UNIVERSITÀ DI PARMA

UNIVERSITÀ DEGLI STUDI DI PARMA

DOTTORATO DI RICERCA IN FISICA

CICLO XXXIV

Muon sites and couplings in magnetic and superconducting materials: towards high-throughput modelling

---

Coordinatore:
Chiar.mo Prof. Stefano
CARRETTA

Tutore:
Chiar.mo Prof. Roberto DE
RENZI

Co-Tutore:
Dott. Ifeanyi John
ONUORAH

Dottarando:
Muhammad Maikudi ISAH

Anni 2019-2022

Muon sites and couplings in magnetic and superconducting materials: towards high-throughput modelling

by

Muhammad Maikudi ISAH

Supervisor: Prof. Roberto DE RENZI

Co-Supervisor: Dr. Ifeanyi John ONUORAH

Department of Mathematical, Physical and Computer Sciences

University of Parma
Parma, PR, Italy

March 2022

Thesis Reviewers:
Prof. Samuele SANNA
Dr. Pietro DELUGAS

Commission of the final examination:

External:
Prof. Juan JIMÉNEZ
Prof. Giacomo PRANDO

Internal:
Prof. Danilo BERSANI

Final examination:
20th May, 2022

Department of Mathematical, Physical and Computer Sciences, University of Parma,
Parma, Italy

Abstract

Muon sites and couplings in magnetic and superconducting materials: towards high-throughput modelling

Muhammad Maikudi ISAH

This thesis consists of the theoretical study of the muon stopping sites and hyperfine interactions in magnetic compounds mostly using density functional theory (DFT) calculations, to aid in the interpretation of muon-spin spectroscopy (μSR) experimental measurements. A new high-throughput (HT) DFT-based calculation approach to automatically manage these calculations is introduced and benchmarked with a large set of magnetic materials already characterized by μSR experiments. It is also demonstrated in this thesis how the results of these calculations are utilized in characterizing material ground state properties.

First, the theoretical quantum mechanical approach for simulating the time dependent muon spin polarization is described together with its implementation in the open-source, UNDI software package. In particular, the computationally fast and efficient method by Celio is described. Also within this approach, the effects of the electric quadrupolar interactions relevant to accurately capture the physical properties for nuclei with large moment are incorporated. The approach is demonstrated for LiF, Cu, MnSi and utilized to study muon sites and magnetic properties in these compounds.

Another, the results of zero field μSR and nuclear magnetic resonance (NMR) measurements for iron-phosphide Fe_2P are presented. This material is the parent compound of a large family of (Fe/Mn), (P/Si/B) alloys displaying first-order magnetic transitions, exploitable for magnetic energy-harvesting applications. Results of DFT calculations provide unique muon-stopping sites, muon hyperfine interactions and hyperfine at the P nuclei that allowed to further characterize and interprete μSR and NMR measurements, providing accurate description of the ferromagnetic ground state properties of Fe_2P.

Next, efforts and approach towards the design and implementation of workflows for high-throughput DFT-based muon calculations are presented. The aim is to introduce a more user friendly calculation approach with less human intervention that

allows to automatically manage, track and store muon calculation results. The workflow is benchmarked over 16 selected magnetic compounds, that allowed to discuss the success and limitations of the approach at its current stage. Benchmark results show that further improvement on the workflow should include; taking into account the muon charge states and proper treatment of electronic correlation effects.

Finally, results of the electronic and magnetic ground state properties together with the muon charge localization in Chromium Chalcogenide Cr_2S_3 are presented. Cr_2S_3 is one of the 16 magnetic compounds selected in the previous chapter for the benchmark of the workflow, where the poor treatment of electronic correlation within the conventional DFT and absence of muon charge state are limitations encountered while benchmarking the workflow. Here, outside the workflow, calculation results show that adequate electronic correlation and muon charge treatment allow to accurately describe the ground state properties and the muon sites Cr_2S_3 in agreement with experiment. The results of the calculation show that the electronic properties are strongly dependent on the magnetic ordering.

Acknowledgements

First, I give thanks and praise to God for His guidance and protection through all my undertakings in these three years journey at the University of Parma.

I would like to express my deep appreciation and gratitude to my supervisor, Professor Roberto De Renzi, who has the poise and the substance of a genius. During the course of my Ph.D., he continually and convincingly inculcated in me the spirit of adventure in research and excitement in studying physics. Without his constant source of inspiration, ideas, and advice, and his incredibly generous with his time, this thesis would not have been possible. Also, I am extremely thankful to him, the Italian Ministry of Education, Universities and Research, and the University of Parma for providing me with a scholarship opportunity, the time necessary to do this thesis, and a wonderful environment to study physics department. It has been an absolute pleasure and I will always cherish that.

I am equally grateful to my parents, siblings, and friends for their love, encouragement, and prayers during the course of my studies.

I would like to thank my two co-supervisors, Dr. Pietro Bonfà and Ifeanyi John Onuorah, without whom this thesis would not be possible. Both have done more for me than can be expressed in this thesis. They are both not only very knowledgeable people, but they were patient with me and extremely understanding. I consider myself very fortunate to have had such good co-supervisors.

To Dr. Pietro Bonfà: thank you for helping me through my Ph.D. journey and having a ready-made project dropped in my lap at the last years.

To Dr. Ifeanyi John Onuorah: who has always provided me with advice and suggestions regarding my work and settling quickly to the first night I arrived in Parma. Thank you.

I would also like to give special thanks to Professor Giuseppe Allodi, who had endless patience, collaboration, and support while teaching me the basics of NMR laboratory practice. Finally, I gratefully acknowledge the support from the Condensed Matter group at the University of Parma.

I am still grateful to Prof. Emine Kucukbenli for supervising my master's thesis and guiding me to apply for a Diploma scholarship in Condensed Matter and Statistical Physics at Abdus Salam International Centre for Theoretical Physics (ICTP). She incessantly inspired and motivated me to further my studies on computational

Condensed Matter Physics. I am also grateful to Prof. Ali Hassanali at ICTP for his guidance and for providing me with valuable insight into the Ph.D. journey.

Finally, my thanks and appreciations also go to my colleague and friends, Luigi Guerrini, Marco Marinucci, Carmine Borelli, Paolo Soresina, and Joshua which we occasionally play my favorite sport in name of Football.

To those I forgot to mention, I owe you all a big thanks.

List of publications

Some of the works published during my Ph.D are also presented in this thesis. Paper 1 and 2 are presented in chapters 5 and 4 respectively. The results and level of participation of other works I was involved in that are not included in this thesis are also highlighted here, in the **comments and participation** section.

1. **Ab *initio* modeling and experimental investigation of Fe_2P by DFT and spin spectroscopies.** Pietro Bonfà, Muhammad Maikudi Isah, Benjamin A. Frandsen, Ethan J. Gibson, Ekkes Brück, Ifeanyi John Onuorah, Roberto De Renzi, and Giuseppe Allodi.

   Submitted to: Physical Review Materials.
   DOI:10.1103/PhysRevMaterials.5.044411

2. **UNDI: An open-source library to simulate muon-nuclear interactions in solids.** Pietro Bonfà, Jonathan Frassineti, Muhammad Maikudi Isah, Ifeanyi John Onuorah, and Samuele Sanna

   Submitted to: Journal of Computer Physics Communications.
   DOI:10.1016/j.cpc.2020.107719

3. **Intrinsic Nature of Spontaneous Magnetic Fields in Superconductors with Time-Reversal Symmetry Breaking.** Benjamin M. Huddart, Ifeanyi J. Onuorah, Muhammad M. Isah, Pietro Bonfà, Stephen J. Blundell, Stewart J. Clark. Roberto De Renzi, and Tom Lancaster.

   Submitted to: Physical Review Letters.
   DOI:10.1103/PhysRevLett.127.237002

   Comments and participation:

   This work was carried out in colloboration with groups at Durham and Oxford, UK. Here, we address the origin of the spontaneous magnetization detected with μ^+SR in superconductors, arising below the superconducting transition that corresponds to a spontaneous time-reversal symmetry breaking (TRSB). This phenomenon, not predicted by simple Bardeen-Cooper-Schrieffer (BCS) models, is still not fully understood. The very tiny TRSB fields are observed in a number of materials, in particular non-centrosymmetric compounds, but

they escape detection by scanning probe methods. In order rule out a muon-induced origin of the TRSB observed with μ^+SR, we determined the muon implantation sites and investigate the effects of implanted muon by evaluating the effects on its electronic structure, spin density, and lattice distortions.

In this paper, I gratefully acknowledge Ifeanyi J. Onuorah by involving me take part in the analysis of muon-stopping sites.

4. **Frustrated network of indirect exchange paths between tetrahedrally coordinated Co in Ba_2CoO_4.** Ifeanyi John Onuorah, Muhammad Maikudi Isah, Roberto De Renzi, and Pietro Bonfà.

   Submitted to: Physical Review Materials.
   DOI:10.1103/PhysRevMaterials.5.124407

   Comments and participation:

   Ba_2CoO_4 consists of non-connected and distorted CoO_4 tetrahedra as opposed to other cobalites with Co and O on octahedral coordinations. We performed detailed first-principle identifying the magnetic ground state and the dominant exchange interactions through a projection on Wannier wavefunctions. The couplings justify the presence of frustration and a Néel temperature lower than the Curie temperature obtained from paramagnetic susceptibility.

   This paper was conceived and planned by Ifeanyi John Onuorah. My early contributions to this paper was initiate to the search of realizations of Ba_2CoO_4 magnetic structure and later involved to the discussions of the results.

5. **Entanglement between muon and $I > \frac{1}{2}$ nuclear spins as a probe of charge environment.** Pietro Bonfà, Jonathan Frassineti, John M. Wilkinson, Giacomo Prando, Muhammad Maikudi. Isah, Chennan Wang, Tiziana Spina, Boby Joseph, Vesna Mitrović, Roberto De Renzi, Stephen J. Blundell, and Samuele Sanna.

   Submitted to: Physical Review Letters.

   Comments and participation:

   In summary, we have presented calculations of quantum coherence between the spins of muons and nuclei. Our results demonstrate that in the coherent quantum regime the positive muons can be used to analyze structural and electronic properties in non magnetic materials hosting quadrupolar nuclei ($I > \frac{1}{2}$) as a quantum sensor tool of local charge-related phenomena. This type of coherence phenomena is clearly seen with $I = \frac{1}{2}$ spin systems (i.e. Fluorides; [J. M. Wilkinson et al., Phys. Rev. Lett. **125**, 087201 (2020)]) where the quadrupolar interaction is not interfering with the quantum entanglement of few nearly isolated spins including the muon. It was not clear until now that an analogous coherence was possible to observe in the presence of quadrupolar interactions. Here we predict and measure the time evolution in A15 type II materials (incidentally, superconductors) that include V_3Si, V_3Sn and Nb_3Sn.

   In this paper, I have carried out some part of the DFT calculation of muon-stopping site(s) in consultations with Pietro Bonfà. The design of the experiments was conceived by Samuele Sanna and the main thrust in the analysis was put forward by Pietro Bonfà.

Contents

List of Figures

List of Tables

List of Symbols

A	ampere
kg	kilogram
s	second
m	metre
ω	angular frequency
μ^+	positive charge muon
μ^-	negative charge muon
Z	atomic number

C	coulomb	1 C	=	$1\,\mathrm{A\,s}$
V	volt	1 V	=	$1\,\mathrm{m^2\,kg\,s^{-3}A^{-1}}$
F	Farad	1 F	=	$1\,\mathrm{C\,V^{-1}}$
e	electronic charge	1 e	=	$1.602\,18 \cdot 10^{-19}\,\mathrm{C}$
Hz	hertz	1 Hz	=	$1\,\mathrm{s^{-1}}$
T	Tesla	1 T	=	$1\,\mathrm{kg\,s^{-2}\,A^{-1}}$
J	Joule	1 J	=	$1\,\mathrm{kg\,m\,s^{-2}}$
eV	electronvolt	1 eV	=	$1.602\,18 \cdot 10^{-19}\,\mathrm{J}$
Ha	Hartree	1 Ha	=	27.2114 eV
Å	ångström	1 Å	=	$10^{-10}\,\mathrm{m}$
m_e	electron mass	m_e	=	$9.109\,38 \cdot 10^{-31}\,\mathrm{kg}$
m_p	proton mass	m_p	=	$1.672\,62 \cdot 10^{-27}\,\mathrm{kg}$
$\hbar$	reduced Planck constant	$\hbar$	=	$1.054\,57 \cdot 10^{-34}\,\mathrm{Js}$
ϵ_0	dielectric permittivity of vacuum	ϵ_0	=	$8.854\,19 \cdot 10^{-12}\,\mathrm{F\,m^{-1}}$
bohr	Bohr radius (a_0)	1 bohr	=	$4\pi\epsilon_0\hbar^2/\mathrm{m_e e^2} = 0.529177$ Å
μ_B	Bohr magneton	μ_B	=	$\mathrm{e}\,\hbar/2\mathrm{m_e} = 5.78838 \cdot\ 10^{-5}\,\mathrm{eV\,T^{-1}}$

List of Abbreviations

μSR	Muon Spin rotation and Relaxation spectroscopy
AE	All Electron
AF/AFM	Antiferromagnet
AiiDA	Automated Interactive Infrastructure and Database for Computational Science
BO	Born-Oppenheimer
DFT	Density Functional Theory
DOS	Density of States
EFG	Electric Field Gradient
FCC	Face Center Cubic
FM	Ferromagnet
FOMT	First Order Magnetic Transition
FiM	Ferrimagnet
GBRV	Garrity Bennett Rabe Vanderbilt
GGA	Generalized Gradient Approximation
HEG	Homogeneous Electron Gas
HK	Hohenberg and Kohn
HPC	High performance computing
HT	High-throughput
KS	Kohn and Sham
KT	Kubo and Toyabe
LCAO	Linear Combination of Atomic Orbitals
LDA	Local Density Approximation
LF	Longitudinal field
LRO	Long Range Magnetic Order
LSDA	Local Spin Density Approximation
MAGNDATA	Magnetic structures database
MAPD	Mean Absolute Percentage Deviation
MCA	Magnetocrystalline Anisotropy
MP	Monkhorst and Pack
MT	Muffin-tin
MUESR	Magnetic Structure and Muon Embedding Site Refinement
Mu	Muonium

NCPP	Norm-Conservation Pseudopotential
NMR	Nuclear Magnetic Resonance
NQM	Nuclear Quadrupole Moment
PAW	Projector Augmented Wave
PBE	Perdew Burke Ernzerhof
PDOS	Partial Density of States
PK	Primary Key
PP	Pseudopotential
QE	Quantum Espresso
RPA	Random Phase Approximations
SCAN	Strongly Constrained and Appropriately Normed
SOC	Spin Orbit Coupling
TF	Thomas-Fermi
UEP	Unperturbed Electrostatic Potential
UNDI	Muon Nuclear Dipolar Interaction
USPP	Ultrasoft Pseudopotential
UUID	Universal Unique Identifier
VCM	Valence Band Maximum
VESTA	Visualisation for Electronic Structural Analysis
XMCD	X-Ray Magnetic Dichroism
ZF	Zero field

CHAPTER 1

Introduction

The main focus of this thesis is to provide improved and more efficient computational procedures to aid the analysis of muon spectroscopy experimental data and facilitate better understanding of the properties of magnetic compounds. I present an approach I developed to automate the various calculation protocols of the muon-stopping sites and their hyperfine interactions with the electronic environment.

Muon spin rotation and relaxation (μSR) spectroscopy has become a widely popular technique for studying microscopic internal magnetic fields in condensed matter systems including magnetic, superconducting [1–4], heavy-fermion and other strongly correlated electron systems [5–7]. A number of magnetic properties have been successfully investigated, which include; magnetic penetration depths [8–12], vortex state [13, 14] in superconductors, muonium states in semiconductors [15–17]. In μSR, spin polarized positive muons are injected into a target sample to serve as a sensitive local probes of magnetism and other physical properties. However, a wholesome interpretation of μSR experimental data and understanding the effects of the implanted muon in the local environment is sometimes crippled by the lack of knowledge of where the muon choose to stop in the sample and the difficulty in quantifying the muon hyperfine interactions within the host. In few cases, it has been possible to determine the muon-stopping site by some specific experimental measurements such as: muon-Knight shift measurements [18, 19], level-crossing resonance spectroscopy [20] and/or analysis of dipolar coupling and muon polarization functions [21, 22].

In the recent years, there have been significant progress with the integration of a more thorough and accurate first principle simulations in μSR data analysis, thanks to the development of algorithms and hardware of high-performance computing (HPC) that provide powerful tools to accelerate usage of these approaches. Particularly, the usage of the well-established density functional theory (DFT) calculations for electronic structure calculations allows to reliably find the muon-stopping sites, analyze the effects of muon implantation in the sample and as well accurately quantify the hyperfine interactions [23–33]. In this thesis, I have further utilized the existing calculation protocols to validate the μSR and NMR experimental results while studying

the magnetic phase transitions and ground state magnetic properties of a number of selected materials.

The recent advent of high throughput computing and the development of dedicated frameworks has opened to the possibility of performing computational material design. I have applied similar procedures to the computational methods already in use for the collection of muon-sample interaction parameters calculation procedure and workflows that allow the automation of the muon calculation protocols. I have also benchmarked and demonstrated the success of the workflow and HT calculations in a number of magnetic materials selected by screening the magnetic structure database.

The next two chapters of this thesis are introductory and provide an overview of the μSR technique and DFT method relevant for this thesis, while subsequent chapters each contain distinct topics on the study of material properties and the progress made in muon-stopping site(s) calculations with DFT.

1.1 Thesis structure

The thesis is structured as follows:

Chapter 2 : Introduction to muon spin spectroscopy : In this chapter, I describe the μSR experimental technique together with relaxation functions for μSR data analysis.

Chapter 3 : Density functional theory : In this chapter, I present the density functional theory (DFT) method and other theoretical considerations utilized for calculations in this thesis.

Chapter 4 : Simulation of muon spin polarization: Case study with Fluorides, Cu and MnSi : Here, I present a quantum mechanical method to study the spin dynamics of a static muon interacting with neighboring nuclear spins.

Chapter 5 : Magnetic ground state of Fe_2P from experimental and ab-initio modelling perspective : Here, I present the μSR and NMR measurements on Fe_2P together with DFT calculations of the muon stopping site, the hyperfine coupling calculations both at the muon and nuclei, that allowed complete characterization of the origin of the signals observed from the two techniques.

Chapter 6 : High-throughput design and implementation for muon-site and hyperfine calculations: In this chapter, I present the high-throughput calculation approach and workflows I have developed to automate muon calculation procedures. I further benchmarked this approach in a number of magnetic materials.

Chapter 7 : Magnetic properties and effects of muon charge localization in Cr_2S_3: In this chapter, I present a refined and more optimized first principles calculations that allow to describe the ground state electronic and magnetic

properties of Cr_2S_3. I also discuss the muon stopping sites, muon charge localization, hyperfine interactions and their implications on the magnetic properties of Cr_2S_3.

Chapter 8 : Summary and Conclusion: The thesis is summarised and I discussed the future outlook and improvements.

CHAPTER 2

Introduction to muon spin spectroscopy

In 1936 marked the discovery of the muon from cosmic radiation studies by Carl D. Anderson and Seth Neddermeyer [34, 35], which was further confirmed with the cloud chamber experiment in the following year [36]. Initially, scientists had not realized the potential application of the muon to study condensed matter systems till Garwin *et al.* [37] provided the evidence of its parity violating property relevant for exploring the magnetic field of a solid when implanted in it. This led to the birth of the usage of muon spin spectroscopy as a technique experiment to study condensed matter systems.

In muon spin spectroscopy, the muon spin acts as a sensitive local probe of magnetism and the essence of the method lies on the collected *asymmetry* distribution of the anisotropic emitted positrons in the muon weak decay process. The experimental technique is usually denoted with the acronym μSR [1–4] analogous to nuclear magnetic resonance (NMR) where "μS" is for *muon-spin*, and "R" for either of *rotation*, *relaxation* or *resonance*[1]. μSR has now become a widely used sensitive probe for magnetism and superconductivity.

Further in this chapter, I shall introduce the muon properties and the principles of the μSR experimental setup together with the review of relevant relaxation and fitting functions for data analysis.

2.1 The properties of the muon

The relevant properties of the muon are listed in Table 2.1 in comparison with those of electrons and protons. The muon's mass is heavier than that of the electron but lighter than that of proton. Importantly for the muon decay process, the muon has a short lifetime of 2.197 μs. It has a large gyromagnetic ratio and magnetic moment

[1] *Rotation* refers to the precession of the muon spin caused by an internal or external magnetic field, *Relaxation* refers to the dephasing of the polarization of the muon ensemble as a function of time due to the variation of field distributions, while *Resonance* refers to the application of radio-frequency (RF) to determine the position and shape of the observed level-crossing resonances.

that is 3.183 times that of proton. For this reason, μSR can therefore detect extremely small internal fields.

Also, the charge of the muon allows to distinguish between the negative (μ^-) and positive muon [anti-muon] (μ^+). The μ^- interacts strongly with the nucleus of the host atom and is readily captured into the $1s$ atomic orbital. Also these interactions of μ^- reduce its lifetime and measured asymmetry compared to μ^+ rendering it less sensitive to the physical properties of our interest (namely magnetism and superconductivity), thus leaving μ^+ as the popular choice for measurements in most materials. All discussions in this thesis will be based on μ^+.

Table 2.1: Properties of the muon (μ) in comparison with those of the electron (e) and proton (p), together with the analogous experimental techniques where they are utilized.

	charge	spin	mass	moment	$\gamma/2\pi$ (MHzT^{-1})	lifetime (μs)	technique
e	$\pm e$	$\frac{1}{2}$	m_e‡	$657 \cdot \mu_p$‡	28000	∞	ESR
μ	$\pm e$	$\frac{1}{2}$	$206.768 \cdot m_e$	$3.183 \cdot \mu_p$	135.538	2.197	μSR
p	$\pm e$	$\frac{1}{2}$	$1836.15 \cdot m_e$	μ_p	42.6	∞	NMR

‡ Obtain from [2], where $\mu_p = 1.5 \cdot 10^{-3}\mu_B$ and $m_e = 9.10938 \cdot 10^{-31}$Kg.

2.2 Muon production and decay

Naturally, muons are produced from the collisions of high energy particles with the gas nuclei in the atmosphere, while in the laboratories they are produced by collisions between high energy protons p (from the particle accelerator) with target protons, which then emit the very unstable pions π. The emitted pions with the desired charge (positive pions) and momentum are selected using the dipole magnet and they further decay with a mean lifetime of 26 ns into the positive muons (μ^+) and a neutrino (ν_μ). These processes can be represented as;

$$p^+ + p^+ \longrightarrow \pi^+ + p^+ + n \tag{2.1}$$

$$\pi^+ \longrightarrow \mu^+ + \nu_\mu \tag{2.2}$$

After a mean lifetime of 2.197 μs, the muon decays into positron (e^+) and two neutrinos (ν_e and $\bar{\nu}_\mu$). This process is written as;

$$\mu^+ \longrightarrow e^+ + \nu_e + \bar{\nu}_\mu \tag{2.3}$$

In Fig. 2.1 the schematic representation of the muon production and decay processes are shown, together with the characteristic spin and momentum directions of the produced particle in each process. Particularly, the pion is a spin-zero particle and the neutrino has spin $\frac{1}{2}$ with negative helicity [38] and considering momentum

conservation the muon must have a spin $\frac{1}{2}$ and a negative helicity. This results in the production of *spin polarized* muons.

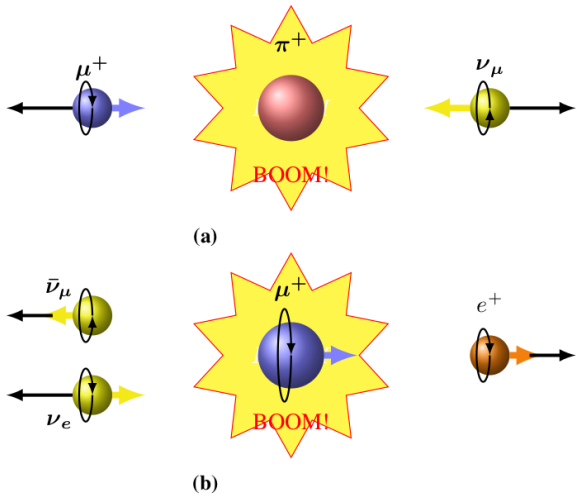

Figure 2.1: A Schematic plot of (a) pion decay, and (b) muon decay. The solid colored and black arrows indicate the spin and momentum direction of each particle respectively. Figure is taken from Ref. [39].

The produced muons kinetic energy are selected. 100% polarized surface muons with kinetic energies of around 4.119 MeV (from pions that decay at the surface of the target) are selected for studying thin samples as they stop within penetration depth of only between 0.1 mm and 1.0 mm. On the other hand, the 'regular' muons with much higher kinetic energy are selected from pions that decay in flight for studies where deeper penetration of the muons are required before they stop in the sample. The selected positive muons are then guided through the beamlines to the sample of interest.

The muon beams used to investigate sample properties can be either continuous or pulsed depending on how they are structured in the facility/laboratory hosting the proton source. The muons as they are directed to the sample, lose their kinetic energy by ionization of atoms and inelastic scattering with electrons in the sample. During this process, the muon might lose or capture an electron temporarily forming a bound state, muonium (Mu $\equiv [\mu^+ e^-]$), which might further dissociate into a bare muon or not. The muon finally arrives and occupy at the implantation site, where they might even form chemical bonds e.g with anions. Importantly, these processes are Coulombic in origin, and occur time scale of nanoseconds, much shorter than the muon's lifetime, thus ensuring that muon spin polarization is preserved during the process.

2.2.1 The muon asymmetry

The muon decay is mediated by the weak force, and violates parity conservation; positron is emitted preferentially along the muon spin direction [37, 38]. This is the key feature that allows μSR to probe materials by exploiting the muon dynamics. As a consequence of the conservation of energy and momentum in this three body decay,

the positron is emitted in a direction with an angle θ to the muon spin direction, with a decay probability plotted in Fig. 2.2b and given by;

$$W(\epsilon,\theta) = \frac{n(\epsilon)}{4\pi}\left(1 + a(\epsilon)\cdot\cos\theta\right) \tag{2.4}$$

where $a(\epsilon)$ is the asymmetry factor that depends on the positron energy $\epsilon = \frac{E}{E_{max}}$ ($E_{max} = 52.85$ MeV) plotted in Fig. 2.2a and given by;

$$a(\epsilon) = \frac{2\epsilon - 1}{3 - 2\epsilon} \tag{2.5}$$

which follows a distribution function plotted in Fig. 2.2a and given by;

$$n(\epsilon) = 2\epsilon^2(3 - 2\epsilon) \tag{2.6}$$

For a fully polarized muon beam in an ideal set-up, the asymmetry factor averages to the value of $\frac{1}{3}$[2]. However, this is not always the case due to limitations from experimental conditions. This value is usually between ~0.2-0.3 [1–3, 40].

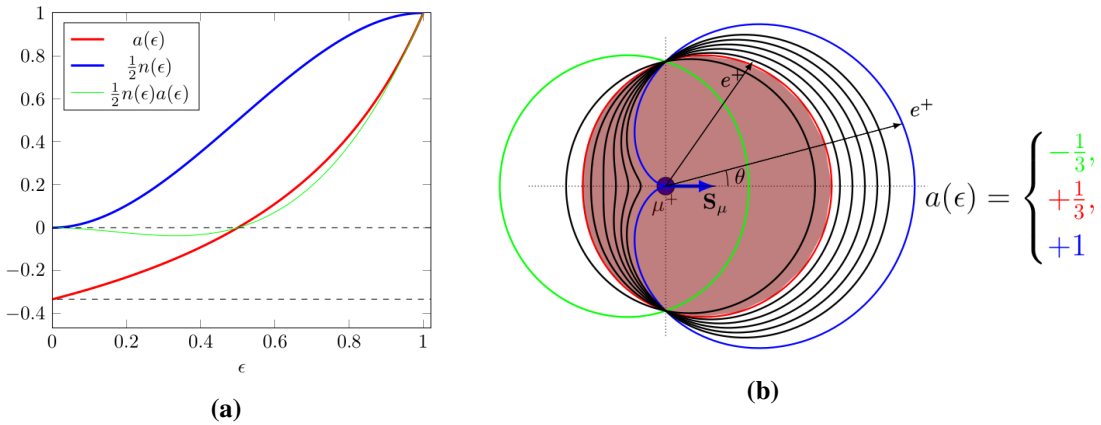

(a) **(b)**

Figure 2.2: (a) The asymmetry parameter $a(\epsilon)$ (red curve), energy distribution $n(\epsilon)$ (blue curve) and weighted asymmetry $n(\epsilon)a(\epsilon)$ (green curve) of positron as a function of normalised kinetic energy ϵ. Negative $a(\epsilon)$ represents lower energy positrons. Figure taken from Ref. [3]. (b) The angular probability distribution $W(\epsilon,\theta)$ [proportional to $\left(1 + a(\epsilon)\cos\theta\right)$] of the positrons for minimum (green curve), maximum (blue curve), and average energy (red curve). The shaded red area corresponds to when all positron energies ϵ are sampled with equal probability, the asymmetry parameter has the value $a = \frac{1}{3}$. Figure taken from Ref. [40].

2.3 Experimental setup and technique

In this section, I briefly introduce the μSR experimental technique and setup (See Ref. [1–4] for details). A schematic representation of a typical μSR setup and positron count is shown in Fig. 2.3.

[2] by simply integrating; $\bar{a}(\epsilon) = \langle a(\epsilon)\rangle = \int_0^1 a(\epsilon)n(\epsilon)d\epsilon = \frac{1}{3}$.

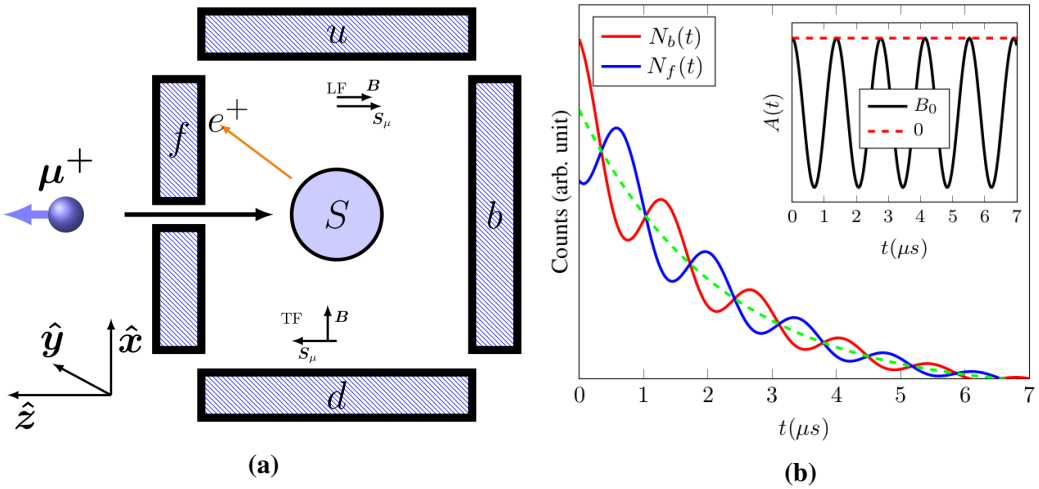

Figure 2.3: (a) A Schematic illustration of μSR experiment with a beam of spin-polarized μ^+ implanted in a sample S. (b) A schematic illustration of the number of positrons detected in the forward (blue curve) and backward (red curve) detectors and the exponential decay of the muons (dotted green curve) for TF geometry. The inset shows an illustration of data collected in form of asymmetry function $A(t)$ (see Eq. (2.8), α = 1.) with a null and homogeneous magnetic field define as B_0. Figure taken from Ref. [2]

In Fig. 2.3a, 100% spin-polarized positive muons (μ^+) beam are directed toward the sample (S), the initial spin polarization is antiparallel to the beam momentum [along $\hat{z}$]. The muon is implanted into the sample (S) and comes to rest at interstitial sites. Assuming the presence of a single local field at all interstitial sites their spin precess around the local magnetic field $\boldsymbol{B}_\mu$ at the stopping site. Each muon decays according to Eq. (2.3), with a lifetime $\tau_\mu \approx 2.197\ \mu s$. The decay positrons e^+ are emitted preferentially in the direction of the μ^+ spin at the time of decay (see Fig. 2.2b), and are detected using an array of detectors surrounding the sample. The detectors are placed around the sample space to track the direction of emitted positrons. There are two possible geometrical configurations for these detectors; longitudinal and transverse, as shown in Fig. 2.3. The former is used for zero-field (ZF) and longitudinal-field (LF) measurements (or ZF/LF-μSR) whilst the latter is used for transverse-field (TF, or TF-μSR). A more detailed discussion of these types of measurements and their applications will be addressed in the following sections. In transverse-field (TF-μSR) or longitudinal-field measurements (LF-μSR) an external field $\boldsymbol{B}$ is applied perpendicular or parallel to the initial muon spin, $\boldsymbol{S}_\mu$ respectively. The detector axis is along $\hat{\boldsymbol{z}}$ for LF configuration, i.e one places detectors; the forward f and backward detector b, and along $\hat{\boldsymbol{x}}$ for TF configuration, i.e one uses the upward u and downward detector d.

For each detector the positron count rate $N(t)$ is given by;

$$N(t) = N^0 e^{-t/\tau_\mu}\left[1 + a_0 P(t)\right] + N_{\text{bg}}, \tag{2.7}$$

where $P(t)$ is the time evolution of the μ^+ ensemble spin polarization component in the direction of the detector ($P(t=0) = 1$ for 100% polarization), N^0 is the initial count rate [and the exponential accounts for the muon decay], a_0 is the count-rate

asymmetry, and $N_{\rm bg}$ is a time-independent background rate. The number of positrons counted in N_f and N_b in the f and b detectors decreases exponentially with time as shown in Fig. 2.3b. For the two f and b detectors (setting $N_f^0 = N_b^0, N_f^{\rm bg} = N_b^{\rm bg}$ in Eq. (2.7)), we can extract the normalized asymmetry spectrum $A(t)$ as;

$$A(t) = \frac{N_b(t) - \alpha N_f(t)}{N_b(t) + \alpha N_f(t)} = a_0 P(t). \tag{2.8}$$

Fig. 2.3b contains the essential information conveyed by muons concerning local static and dynamic magnetic properties of the sample. The constant α is experimentally determined to account for any difference in detector efficiency. Typically in μSR, $N \approx 10^7$ count of events are collected for a single measurement of $A(t)$. It is the asymmetry spectrum $A(t)$ that contains the essential information conveyed by muons on the internal field distribution (both static or dynamic). The asymmetry spectrum oscillates at a frequency directly proportional to the magnitude of the magnetic field B_μ experienced by the muon and any dephasing of oscillation demonstrates the effects of any spatial or time-dependent variations in the local field. In general, the muon spin interacts with its local environment. In the inset of Fig. 2.3b, I show the plot for muons in zero local field, and also for muons in a homogeneous transverse magnetic field B_0. Typically, in a μSR experiment, one interprets the asymmetry data by fitting to a proposed model for the internal field distribution of the sample using a least-squares fitting procedure.

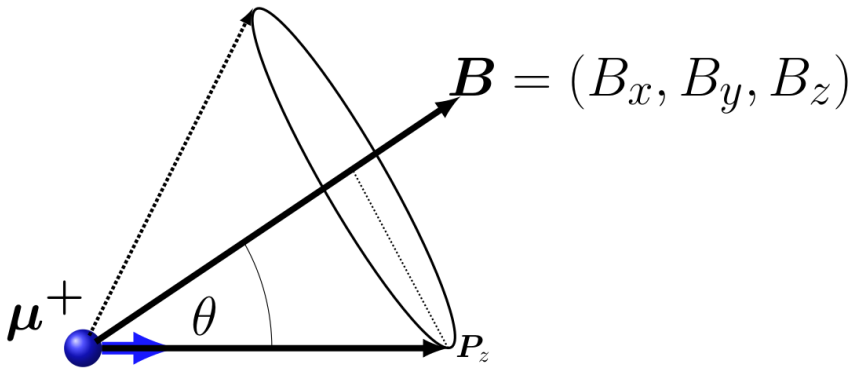

Figure 2.4: A schematic representation of the muon spin precession around a local magnetic field $\boldsymbol{B}$. Figure taken from Ref. [40].

2.4 Muon precession and relaxation

In μSR experiments, if each implanted muon senses the same magnetic field $\boldsymbol{B}_\mu$ oriented at an angle θ with respect to the initial muon polarization along z-axis, its spin will precess around $\boldsymbol{B}_\mu$ with Larmor (angular) frequency (see Fig. 2.4);

$$\omega_\mu = \gamma_\mu |\boldsymbol{B}_\mu| \tag{2.9}$$

where $\gamma_\mu = 2\pi \times 135.5\,\mathrm{MHzT}^{-1}$ is the muon gyromagnetic ratio. The time evolution of the z-component of muon polarization $P_z(t)$ is given by;

$$P_z(\theta, |\boldsymbol{B}_\mu|, t) = \cos^2\theta + \sin^2\theta \cos(\gamma_\mu |\boldsymbol{B}_\mu| t) \tag{2.10}$$

However, if the muon sense varying ranges of magnetic field, the time evolution of the muon spin polarization $S_z(t)$ can be obtained as a statistical average of Eq. (2.10) over a field distribution function $f(\mathbf{B})$ given as;

$$\langle P_z(\theta, |\boldsymbol{B}_\mu|, t)\rangle_{\theta, |\boldsymbol{B}_\mu|} = \int P_z(\theta, |\boldsymbol{B}_\mu|, t) f(\mathbf{B}) d\mathbf{B}. \tag{2.11}$$

whereas taking the powder average over the solid angle for a single value of B_μ of the local field yields;

$$P_z(|\boldsymbol{B}_\mu|, t) = \frac{1}{3} + \frac{2}{3}\cos(\gamma_\mu |\boldsymbol{B}_\mu| t) \tag{2.12}$$

where 1/3 represents the non-processing component of the muon that lie parallel to the field direction, where 2/3 represents the perpendicular component.

Since magnetic materials are central in my thesis in the following section I present different types of applied field geometries [zero-field, longitudinal and transverse field μSR experiments] that are possible within μSR and describe the most significant cases of μSR relaxations that can arise in these different cases. Although the μSR relaxations are not vital for my thesis I can recommend Ref. [3] for more detailed library of μSR relaxations.

2.4.1 Zero-field and longitudinal μSR

In Zero-field (ZF-μSR), samples with spontaneous magnetic properties can be probed without necessarily applying an external magnetic field as the muon feels the internal local magnetic field that result from its spontaneous precession. This feature provides unique information on the magnetic structure and the nature of the internal magnetic field distribution. If long-range magnetic order is present, a significant number of muons will stop in sites of equivalent local magnetic fields $|\boldsymbol{B}_\mu|$ resulting in a coherent muon precession frequency $\nu_\mu = \omega_\mu/2\pi$ that is clearly dictated from cosinusoidal nature of the asymmetry spectrum $A(t)$.

If the local magnetic field has an inhomogeneous distribution the muons oscillate at different frequencies and the muon asymmetry dephases over time. In an ordered sample, it can happen that the muon senses a slight variation of the local magnetic field, this results to weak damped oscillations. If the muon is in a paramagnetic state, its local magnetic fields are well known to arise from surrounding nuclear dipolar moments that result in the formation of static Gaussian field distribution [41, 42] with width $\Delta = \langle (B - \langle B\rangle)^2\rangle^{1/2}$ [40]. γ_μ is the muon gyromagnetic ratio. If the distribution is centred around zero field $\langle B\rangle = 0$, then, the resulting time evolution of the muon spin polarisation is well characterised by the Gaussian Kubo-Toyabe (KT) function [43, 44] written as;

$$P_z^{\mathrm{ZKT}}(\Delta, t) = \frac{1}{3} + \frac{2}{3}\left(1 - \gamma_\mu^2\Delta^2 t^2\right)\exp\left(-\frac{\gamma_\mu^2\Delta^2 t^2}{2}\right) \tag{2.13}$$

The KT function is appropriate for dense moments in the lattice. The schematic representation of the KT function is plotted in Fig. 2.5 (red curve). The plot shows the characteristic 1/3 asymmetry at long time and a Gaussian relaxation function at shorter time due to dephasing of the muons. This function has a minimum at $t_{\min} = \sqrt{(3)}/\gamma_\mu\Delta$ and subsequently increase to an asymptotic asymmetry value. Assuming a simple magnetic dipole interaction between a nuclear spin I and a muon, Δ can be described as [1, 3]:

$$\gamma_\mu^2\Delta^2 = \frac{4}{3}\left(\frac{\mu_0}{4\pi}\right)^2 \sum_i \frac{(\gamma_\mu\gamma_I\hbar)^2}{r_i^6}\frac{I_i(I_i+1)}{3} \tag{2.14}$$

where γ_I is the gyromagnetic ratio of the nuclear I_i and r_i is the distance between the muon and the nearby nuclear I_i.

In *dilute* systems, such as dilute spin-glass [42] it is known that the dipolar fields from the local moments follow a Lorentzian distribution [45]. This distribution follows the so-called KT-Lorentzian relaxation function [42]

$$P_z^{\mathrm{L}}(a,t) = \frac{1}{3} + \frac{2}{3}(1-at)\exp(-at) \tag{2.15}$$

where a/γ_μ is the distribution half-width at maximum [42, 44]. This function decays faster at short time due to the wider range of distribution of $|\mathbf{B}|$ as compared to Gaussian KT function in Eq. (2.13). A comparison of the relaxation functions due to static Gaussian and Lorentzian distribution is plotted in Fig. 2.5.

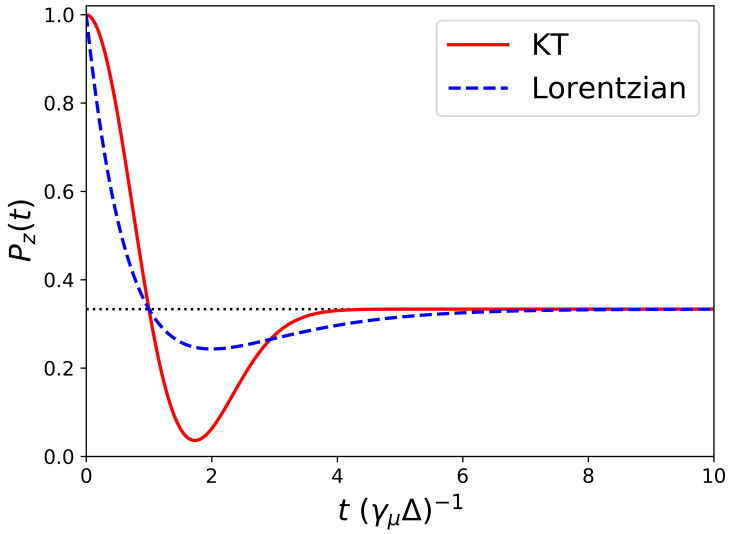

Figure 2.5: The Kubo-Toyabe (solid curve) function (Eq. (2.13)) and the Lorentzian (dashed line) (Eq. 2.15) with width $\gamma_\mu\Delta = a = 0.2$ MHz.

In the longitudinal field μSR (LF-μSR) an external magnetic field $\boldsymbol{B}_{\mathrm{LF}}$ is applied parallel to the initial muon spin polarization which aligns the local magnetic internal field along the direction of the applied field. This setup is also useful for studying the nature of muon depolarization in an inhomogenous internal field, as the muon spin is decoupled from the internal magnetic field with an applied external field stronger

than the internal magnetic field. For LF-μSR, the Gaussian distribution function in an applied field $\boldsymbol{B}_{\mathrm{LF}} = B_{\mathrm{L}}\hat{z}$ has an analytical form given as [41];

$$P_z^{\mathrm{LKT}}(\Delta, \omega_{\mathrm{L}}, t) = 1 - \frac{2(\gamma_\mu \Delta)^2}{\omega_{\mathrm{L}}^2}\left[1 - \cos(\omega_{\mathrm{L}} t)\exp\Big(-\frac{\gamma_\mu^2 \Delta^2 t^2}{2}\Big)\right] + \frac{2(\gamma_\mu \Delta)^4}{\omega_{\mathrm{L}}^3}\int_0^t \sin(\omega_{\mathrm{L}} x)\exp\Big(-\frac{\gamma_\mu^2 \Delta^2 x^2}{2}\Big)dx \quad (2.16)$$

where $\omega_{\mathrm{L}} = \gamma_\mu B_{\mathrm{L}}$ and Δ/γ_μ is the width of Gaussian distribution. This function is plotted in Fig. 2.6 for a range of $\omega_{\mathrm{L}}/\gamma_\mu\Delta$ values. It can be seen that for fields $\omega_{\mathrm{L}} \approx 10\gamma_\mu\Delta$ ($B_{\mathrm{L}} \approx 10\Delta$), the relaxation approaches 1 asymptotically as $\boldsymbol{B}_{\mathrm{LF}} \gg \boldsymbol{B}_\mu$; the muon spins are "decoupled" [41] from their local field. Thus, LF relaxation is useful for probing the dynamics of a system.

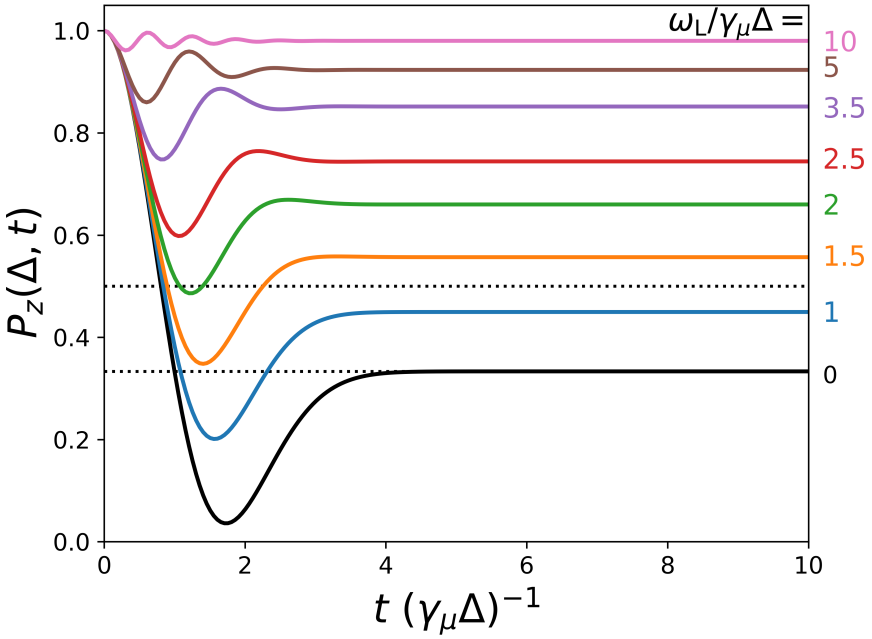

Figure 2.6: The Kubo-Toyabe function for the longitudinal fields B_{L} (Eq. (2.16)) plotted for different B_{L} in the unit of $\omega_{\mathrm{L}}/\gamma_\mu\Delta$, where $\gamma_\mu\Delta$ = 1.0 MHz. At zero field (black line), the plot is the KT function in Eq. (2.13).

2.4.2 Transverse field μSR

In transverse field muon spin rotation (TF-μSR), an external magnetic field $\boldsymbol{B}_{\mathrm{TF}}$ is applied perpendicular to the initial muon spin polarization i.e along x. Hence, the muon spin will precess in the plane perpendicular to the field direction with precession frequency given as $\gamma_\mu|\boldsymbol{B}_{\mathrm{TF}}|$. TF-$\mu$SR experiments are used to measure or study the magnetic field distribution of the vortex lattice in a type-II superconductor [13], the μ^+ Knight shift in metallic systems [18, 19] or dynamical processes like muon

diffusion or spin fluctuations. When an external field $\boldsymbol{B}_{\mathrm{TF}}$ is applied the ensemble muon spin rotates around $\boldsymbol{B}_{\mathrm{TF}}$ and any variation of local magnetic field distribution is observed via;

$$P_x(t) = G_x(t)\cos(\omega_{\mathrm{T}} t + \phi) \tag{2.17}$$

where $\omega_{\mathrm{T}} = \gamma_\mu |\boldsymbol{B}_{\mathrm{TF}}|$ is the angular frequency of the oscillations which is dependent on the local transverse field $\boldsymbol{B}_{\mathrm{TF}}$. ϕ is the phase that depends on the initial angle between the muon spin and the detector. $G_x(t)$ is the transverse function that describe the information about field distribution and dynamical processes.

In the case of purely static field distribution, if the distribution has a Gaussian shape the muon polarization function often takes the form [41];

$$P_x(t) = \exp\Big(-\frac{\gamma_\mu^2 \Delta^2 t^2}{2}\Big)\cos(\omega_{\mathrm{T}} t + \phi) \tag{2.18}$$

where $\omega_{\mathrm{T}} = \gamma_\mu B_{\mathrm{T}} (\boldsymbol{B}_{\mathrm{TF}} = B_{\mathrm{T}}\hat{x})$. For large $\boldsymbol{B}_{\mathrm{TF}}$, the asymmetry spectrum oscillates at a frequency corresponding to the applied field and decays with a Gaussian whose width is related to the distribution of fields at the muon site.

In the case of dynamic fluctuations, where the local fields at the muon site fluctuate or the muon diffuses through the solid, caused for example by magnetic excitations [46–49] or ionic diffusions and muon motion [50–55] etc. For the Gaussian field distribution, the TF relaxation function $P_x(t)$ often takes the following form:

$$\begin{aligned} P_x(\Delta, \nu, \omega_{\mathrm{T}}, t) &= \exp\left(-\frac{\gamma_\mu^2 \Delta^2}{\nu^2}(\nu t - 1 + e^{-\nu t})\right)\cos(\omega_{\mathrm{T}} t) \\ &= G_x^{\mathrm{AA}}(\Delta, \nu, t)\cos(\omega_{\mathrm{T}} t) \end{aligned} \tag{2.19}$$

where ν is the fluctuation (or muon hopping) rate and Δ is the Gaussian width. Equation (2.19) is the Abragam formula [56]. In Fig. 2.7, $G_x^{\mathrm{AA}}(\Delta, \nu, t)$ is plotted for high TF for varying values of the fluctuation rate. For increasing fluctuation rate, one observes the reduction of the depolarization at short times. (See Ref. [41] and [57] for more details.)

For an increasing fluctuation rate, one observes a reducing depolarization at short times. For more see Ref. [41] and numerical calculations [57].

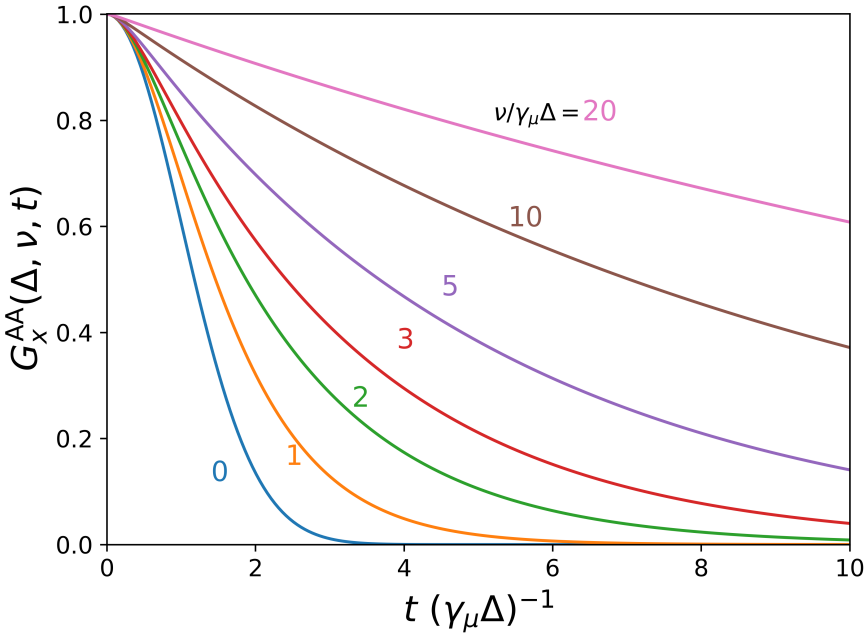

Figure 2.7: The dynamical TF characteristic function (see Eq. (2.19)) for different muon hopping rates ν plotted in the unit of $\nu/\gamma_\mu\Delta$, where $\gamma_\mu\Delta$ = 1.0 MHz.

2.5 Local magnetic field at the muon site

In μSR, the implanted muon possesses a gyromagnetic ratio (γ_μ), which in the presence of magnetic field results in muon spin precession frequency $\nu_\mu = \omega_\mu/2\pi$,

$$\nu_\mu = \frac{\omega_\mu}{2\pi} = \frac{\gamma_\mu}{2\pi}|\boldsymbol{B}_\mu(\boldsymbol{r}_\mu)|, \tag{2.20}$$

where $\boldsymbol{B}_\mu$ is the local magnetic field at the muon site $\boldsymbol{r}_\mu$, with the following components [3];

$$\boldsymbol{B}_\mu(\boldsymbol{r}_\mu) = \boldsymbol{B}_{\text{ext}} + \boldsymbol{B}_{\text{dip}}(\boldsymbol{r}_\mu) + \boldsymbol{B}_{\text{cont}}(\boldsymbol{r}_\mu) \tag{2.21}$$

where

- $\boldsymbol{B}_{\text{ext}}$ is the applied external field already discussed above in Sec. 2.3 and 2.4,
- $\boldsymbol{B}_{\text{dip}}$ is the dipolar coupling interaction that arises between the muon-spin and the lattice of localized electronic or nuclear magnetic moments $\boldsymbol{m}$.
- $\boldsymbol{B}_{\text{cont}}$ is the hyperfine contact field which arises due to short-range interaction between the muon-spin and the local electronic spins at the vicinity of the muon.

The dipolar contribution to the local field at the muon is given by;

$$\boldsymbol{B}_{\text{dip}}(\boldsymbol{r}_\mu) = \frac{\mu_0}{4\pi}\sum_i^N \left[\frac{3\hat{\boldsymbol{r}}_i(\boldsymbol{m}_i \cdot \hat{\boldsymbol{r}}_i) - \boldsymbol{m}_i}{r_i^3}\right], \tag{2.22}$$

where $\boldsymbol{r}_i = \boldsymbol{r}_\mu - \boldsymbol{R}_i$, and $\hat{\boldsymbol{r}}_i = \boldsymbol{r}_i/|\boldsymbol{r}_i|$ is the position of muon relative to magnetic moments $\boldsymbol{m}_i$ and unit vector, respectively, and the sum runs over all the N magnetic moments $\boldsymbol{m}_i$ at site $\boldsymbol{r}_i$. In this thesis, the $\boldsymbol{B}_{\text{dip}}$ at the muon site $\boldsymbol{r}_\mu$ is calculated using the MUESR library which performs the summation using the Lorentz method, where a sphere construction approach is invoked (more details at Ref. [3]), which distinguishes three contributions to the summation:

$$\boldsymbol{B}_{\text{dip}}(\boldsymbol{r}_\mu) = \boldsymbol{B}'_{\text{dip}}(\boldsymbol{r}_\mu) + \boldsymbol{B}_{\text{Lor}} + \boldsymbol{B}_{\text{dem}}. \tag{2.23}$$

$\boldsymbol{B}'_{\text{dip}}(\boldsymbol{r}_\mu)$ has the same form as Eq. (2.22) restricted to the lattice sum of magnetic moments $\boldsymbol{m}_i$ within the Lorentz sphere. The Lorentz field is $\boldsymbol{B}_{\text{Lor}} = \frac{\mu_0}{3}\mathbf{M}_s$, where $\mathbf{M}_s$ is the magnetization of the material and accounts for the dipole field due to magnetic moments outside the sphere. $\boldsymbol{B}_{\text{dem}} = -\mu_0\bar{\mathbf{N}}\cdot\mathbf{M}_b$ is the demagnetization field generated by the free charges at the edges of the sample. $\bar{\mathbf{N}}$ is the demagnetization tensor and $\mathbf{M}_b$ is the bulk magnetization of the whole sample. The demagnetization tensor N depends on the shape of the sample and known for a number of regular shapes (eg. infinite thin film, $N = 0$, sphere, $N = 1/3$, etc). In order to correctly calculate dipolar field at the muon site, accurate magnetic structure and ordering of magnetic moments is required. These are often obtained from magnetic structure characterization experiments (neutron diffraction), single crystal μSR or/and from DFT calculations.

The hyperfine contact field $\boldsymbol{B}_{\text{cont}}$ in Eq. (2.21) is proportional to the local electron spin density at the muon site $\boldsymbol{r}_\mu$ which is induced by the polarisation of the conduction electrons. Thus, $\boldsymbol{B}_{\text{cont}}$ requires the detailed form of the wave function of the electron. It is however common to assume that $\boldsymbol{B}_{\text{cont}}$ is isotropic, i.e. assuming a spherical electron wave functions, which has the form [3, 26]:

$$\boldsymbol{B}_{\text{cont}}(\boldsymbol{r}_\mu) = \frac{2\mu_0\mu_B}{3}\rho_s(\boldsymbol{r}_\mu)\hat{\boldsymbol{d}} \tag{2.24}$$

where $\rho_s(\mathbf{r}_\mu) = \rho_s^{\uparrow} - \rho_s^{\downarrow}$ is the scalar value of local spin density at the muon site, $\rho_s^{\uparrow}$ and $\rho_s^{\downarrow}$ are the spinor components of spin density and $\hat{\boldsymbol{d}}$ is the global spin axis direction defined by the ordered magnetic moments of the host atoms. Thus to properly estimate this quantity a detailed and accurate treatment of electronic properties and wavefunctions are needed. The calculation of the contact hyperfine contribution using DFT calculations is well established [26], this approach was also utilized in this thesis for the calculation of $\mathbf{B}_{\text{cont}}$.

It is worthwhile to point out that the knowledge of the muon implantation site is required to evaluate the contributions to the muon local field, Eq. (2.22) and (2.24). Approaches by DFT calculations to identify muon sites are further discussed in the subsequent chapters of this thesis. I now describe in the next chapter, the DFT method used for calculations in this thesis.

CHAPTER 3

Density functional theory

In this chapter I present the formalism of the density functional theory (DFT) and electronic structure approaches that were utilized for calculations in this thesis.

3.1 Introduction

In quantum mechanics, in order to study and obtain the ground state properties of a many interacting particles system, we have to solve the time-independent Schrödinger equation for the many-electron wavefunction Ψ given by;

$$\mathcal{H}|\Psi\rangle = E|\Psi\rangle \tag{3.1}$$

where $\mathcal{H}$ is the Hamiltonian operator of the system, E is the energy, and $|\Psi\rangle$ the many-particle wavefunction. In the non-relativistic picture, the Hamiltonian of the many-body particle is a strongly coupled system consisting of two species: electrons and nuclei. The Hamiltonian (in SI units) consist of the following terms:

$$\mathcal{H} = -\overbrace{\frac{\hbar^2}{2}\sum_{I}^{N_n}\frac{\nabla_I^2}{M_I}}^{T_\mathrm{n}} + \overbrace{\frac{1}{2}\sum_{I\neq J}^{N_n}\frac{Z_I Z_J e^2}{4\pi\epsilon_0|\boldsymbol{R}_I-\boldsymbol{R}_J|}}^{V_\mathrm{nn}} - \overbrace{\frac{\hbar^2}{2m_e}\sum_{i}^{N_e}\nabla_i^2}^{T_\mathrm{e}} + \underbrace{\frac{1}{2}\sum_{i\neq j}^{N_\mathrm{e}}\frac{e^2}{4\pi\epsilon_0|\boldsymbol{r}_i-\boldsymbol{r}_j|}}_{V_\mathrm{ee}} - \underbrace{\sum_{i,I}^{N_\mathrm{e},N_\mathrm{n}}\frac{Z_I e^2}{4\pi\epsilon_0|\boldsymbol{r}_i-\boldsymbol{R}_I|}}_{V_\mathrm{ne}} \tag{3.2}$$

where the indices i, j represent the electrons and I, J for the atomic nuclei. Z is the atomic number while $\boldsymbol{R}$ and $\boldsymbol{r}$ denote nuclear and electron coordinates respectively, M and m_e are the nuclear and electron mass respectively, while N_n and N_e are the number of nuclei and electrons. e is the electronic charge. The description of the various terms in Eq. (3.2) are; T_n is nuclei kinetic energy, V_nn is the nuclei interaction

potential, T_e is the electronic kinetic energy, V_{ee} is the electron-electron interaction and V_{ne} is the nucleus-electron interaction.

However, since our main interest in this thesis is to study the electronic structure and taking into account that the nuclei are much heavier than the electrons, we invoke the Born-Oppenheimer (BO) approximation [58], where we take the nuclei to remain fixed. Hence from Eq. (3.2) we can separate the electronic and nuclear degrees of freedom, such that the time-independent Schrödinger equation of the interacting electrons with wavefunction Φ is written as;

$$\mathcal{H}_e\Phi = E^e\Phi \tag{3.3}$$

and the electronic Hamiltonian $\mathcal{H}_e$ given as:

$$\mathcal{H}_e = T_e + V_{ee} + V_{ne} \tag{3.4}$$

where in what follows and within the BO approximation, V_{ne} is the external potential encompassing the nuclear attraction energy contribution. The wavefunction Φ is dependent on the positions and spin of each of the N_e electrons in the system and must be antisymmetric with the exchange of two electrons. Φ is written as a;

$$\Phi = \Phi(\boldsymbol{r}_1, \boldsymbol{r}_2, \boldsymbol{r}_3, \ldots, \boldsymbol{r}_{N_e}, \sigma_1, \sigma_2, \sigma_3, \sigma_{N_e}) \tag{3.5}$$

The solution of the time-independent Schrödinger equation is suitably solvable for few simple systems such as He or H_2 [59, 60]. However, for larger systems, the number of atoms increases and there is an exponential growth of the required variational parameters such that the solution of the wavefunction of the system explicitly becomes not easily tractable. A number of many-body theories (e.g the Hartree and Hartree-Fock approaches) exist for providing approximate solutions to the time-independent Schrödinger equation. In these mentioned approaches the many interacting electron wavefunction is written as a product of single particle wavefunction neglecting the electron-electron interaction V_{ee} that doesn't allow the antisymmetrization of the product. This approach is not so realistic in some cases for solving electronic structure problems. However, in this thesis we have utilized the DFT method, shown to be very successful for electronic structure studies with the implementation readily available. The following description in this chapter is devoted to the DFT method.

3.2 Density functional theory

The important concept of DFT is that the charge density $n(\boldsymbol{r})$ is the basic variable instead of the wavefunction of many-interacting electrons for solving the many-electron problem. This is such that the problem of solving for N_e particle wavefunction $\Phi(\{\boldsymbol{r}_i\})$ is reduced by treating the terms in Eq. (3.4) as the functionals of the density $n(\boldsymbol{r})$ in a mean-field manner and the physical quantities are now functionals of this density. Thus, DFT formulates the *total* energy as a *functional* of the density, that is $E = E[n(\boldsymbol{r})]$.

The first early attempt of mapping the wavefunction to the charge density is the Thomas-Fermi (TF) model proposed in 1927 [61]. In this approximation, the kinetic energy T_e is calculated assuming homogeneous electron gas (HEG) while, the electron-electron interaction energy V_{ee} and nuclei-electron interaction energy V_{ne} are treated classically neglecting the electron correlation. However, in atoms and materials, the electron density is far from being homogeneous, and unsurprisingly, the TF model is a rough approximation and inaccurate for solving the many-body problem. Even though it was successful in calculating properties like the total energy of atoms, it turned out to fail in the description of a number of properties especially those relating to the binding of atoms. But then, the idea of using the electron charge density as the basic variable instead of the wavefunction turned out to be one of the fruitful outcome of TF theory as it hinted towards DFT. The problems with the TF model was bypassed and Hohenberg and Kohn [62, 63] showed that it is possible in principle to completely describe the electronic structure in terms of $n(\boldsymbol{r})$. Next we continue with the description of the Hohenberg-Kohn (HK) theorems [62, 63].

3.3 Hohenberg-Kohn theorems

The two theorems of Hohenberg and Kohn [62] that show the justification and possibility to use the the charge density as the central quantity are:

Theorem 1 (the uniqueness theorem): This theorem states that *the ground state density* $n(\boldsymbol{r})$ *uniquely determines the external potential* V_{ne} in which the electrons move. The proof of this theorem is of two folds; first by demonstrating that two external potential V_{ne}^1, V_{ne}^2 differing by more than a constant (i.e $V_{ne}^1 \neq V_{ne}^2 + \alpha$) give rise to distinct ground state wavefunctions Φ_1, Φ_2. The Schrödinger equation of systems defined by distinct external potentials V_{ne}^1, V_{ne}^2 can be written as;

$$(T_e + V_{ee} + V_{ne}^1)\Phi_1 = E_1\Phi_1 \tag{3.6}$$

$$(T_e + V_{ee} + V_{ne}^2)\Phi_2 = E_2\Phi_2 \tag{3.7}$$

Taking Φ_1=Φ_2 and subtracting Eqn (3.7) from Eqn (3.6) gives $V_{ne}^1 - V_{ne}^2 = E_1 - E_2 = \alpha$, where α is a constant. This shows that $V_{ne}^1 = V_{ne}^2 + \alpha$ only when distinct external potential give rise to same ground state wavefunction. Hence, by contradiction this shows that external potential that differ by more than a constant give rise to distinct ground state wavefunctions.

The second approach to prove the theorem is by demonstrating that two different non-degenerate ground state wavefunctions Φ_1, Φ_2 from two different external potential V_{ne}^1, V_{ne}^2 respectively, result in different ground state densities n_1, n_2 respectively. From the variational principle, if we assume a non-degenerate ground state, we know that no other wavefunction can give an energy that is less than that of Φ_1 for the Hamiltonian defined by V_{ne}^1. Using Φ_2 as a trial wavefunction for the same Hamiltonian defined by V_{ne}^1, we can then write;

$$E_1 = \langle\Phi_1|T_e + V_{ee} + V_{ne}^1|\Phi_1\rangle < \langle\Phi_2|T_e + V_{ee} + V_{ne}^1|\Phi_2\rangle \tag{3.8}$$

and using Φ_1 as a trial wavefunction of Hamiltonian defined by V_{ne}^2

$$E_2 = \langle \Phi_2 | T_e + V_{ee} + V_{ne}^2 | \Phi_2 \rangle \leq \langle \Phi_1 | T_e + V_{ee} + V_{ne}^2 | \Phi_1 \rangle \tag{3.9}$$

Adding Eq. (3.8) and (3.9) and collecting like terms, we get

$$\langle \Phi_1 | V_{ne}^1 - V_{ne}^2 | \Phi_1 \rangle < \langle \Phi_2 | V_{ne}^1 - V_{ne}^2 | \Phi_2 \rangle \tag{3.10}$$

rearranging and integrating further gives;

$$\int d\boldsymbol{r} \big(V_{ne}^1(\boldsymbol{r}) - V_{ne}^2(\boldsymbol{r}) \big) \big[n_1(\boldsymbol{r}) - n_2(\boldsymbol{r}) \big] < 0 \tag{3.11}$$

Clearly, from Eq. (3.11), saying that $n_1(\boldsymbol{r}) = n_2(\boldsymbol{r})$ is the same as saying that $0 < 0$ which is a contradiction. This shows that the ground state density $n(\boldsymbol{r})$ for an external potential V_{ne} is unique. Further with this theorem we can then write the properties of the ground state of an interacting many-electron system as a unique functional of the electron density as;

$$\begin{aligned} E[n] &= \overbrace{T_e[n] + E_{ee}[n]}^{\text{Universal functional}} + \overbrace{E_{ne}}^{\text{System dependent}} \\ &= F_{HK}[n] + \int d\boldsymbol{r} n(\boldsymbol{r}) V_{ne}(\boldsymbol{r}) \end{aligned} \tag{3.12}$$

Here I have distinguished the energy expression into the universal functional F_{HK} that doesn't depend on the external potential. If this functional is known the Schrödinger equation would be solved exactly.

Theorem 2 (the variational theorem): *This theorem states that the functional $F_{HK}[n]$ that provides the ground state charge $n(\boldsymbol{r})$, minimizes the total energy functional $E[n]$.* This theorem provides a scheme on how to find the ground state charge density, by trying densities and selecting the one that gives the lowest energy. If $n^*(\boldsymbol{r})$ is a trial ground state charge density, then from variational principle;

$$E_0 \leq E[n^*] = F_{HK}[n^*] + E_{ne}[n^*] \tag{3.13}$$

This shows that for densities n^* that are not the true ground state density, $E[n^*]$ represents an upper bound to the true ground state energy E_0. In summary, HK second theorem tell us that *if the true ground state charge density that minimizes $E[n]$ is known, the variational principle for $E[n]$* is

$$\delta \left\{ E[n] - \lambda \left(\int d\boldsymbol{r} n(\boldsymbol{r}) - N \right) \right\} = 0 \tag{3.14}$$

or

$$\frac{\delta E[n]}{\delta n} = \lambda \tag{3.15}$$

subjected to the condition that the total number of particles $N = \int d\boldsymbol{r} n(\boldsymbol{r})$.

3.4 Kohn-Sham formulation

The theorem and proofs put forward by Hohenberg and Kohn [62] (see Sec. 3.3) neither provide the practical scheme on how to determine the explicit functional form of $F_{\mathrm{HK}}[n]$ or the electron density $n(\mathbf{r})$, hence Kohn and Sham [63] (KS) scheme provided approaches to these issue. They provided set of equations that allow to replace the density functional problem of N interacting particles to those of N non-interacting particles provided that the ground state density $n(\mathbf{r})$ of the system is the same. Thus for the $F_{\mathrm{HK}}[n]$ functional, the kinetic energy functional $T_{\mathrm{e}}[n]$ of interacting particles is approximated with the kinetic energy functional $T_{\mathrm{s}}[n]$ of non-interacting particles. The Hartree, U_{H} contribution is also distinguished from the electron-electron interaction energy E_{ee}.

Thus, the functional $F_{\mathrm{HK}}[n]$ is written as;

$$\begin{aligned} F_{\mathrm{HK}}[n] &= T_{\mathrm{e}}[n] + E_{\mathrm{ee}}[n] \\ &= T_{\mathrm{s}}[n] + \frac{1}{2}\int\int d\boldsymbol{r}d\boldsymbol{r}'\frac{n(\boldsymbol{r})n(\boldsymbol{r}')}{|\boldsymbol{r}-\boldsymbol{r}'|} + E_{\mathrm{xc}} \\ &= T_{\mathrm{s}}[n] + U_{\mathrm{H}}[n] + E_{\mathrm{xc}}[n]. \end{aligned} \tag{3.16}$$

E_{xc}, is the exchange-correlation energy (which contains everything that is unknown in the electron electron interaction) and contains the sum of two contributions the exchange energy (E_x) and the correlation energy (E_c). The kinetic energy functional $T_{\mathrm{s}}[n]$ is obtained by the the sum of kinetic energy of the single-particle wavefunctions of the non-interacting system ϕ_i as;

$$T_{\mathrm{s}}[n] = -\frac{1}{2}\sum_i \int d\boldsymbol{r}\langle\phi_i|\nabla^2|\phi_i\rangle \tag{3.17}$$

and the total energy functional is now of the form;

$$E[n] = T_{\mathrm{s}}[n] + \int d\boldsymbol{r}n(\boldsymbol{r})V_{\mathrm{ne}}(\boldsymbol{r}) + U_{\mathrm{H}}[n] + E_{\mathrm{xc}}[n] \tag{3.18}$$

To obtain the ground state enrgy of the interacting system, $E[n]$ is minimized with respect to the variation in $n(\mathbf{r})$ as;

$$\begin{aligned} 0 = \frac{\delta E[n]}{\delta n(\boldsymbol{r})} &= \frac{\delta T_{\mathrm{s}}[n]}{\delta n(\boldsymbol{r})} + V_{\mathrm{ne}}(\boldsymbol{r}) + \frac{U_{\mathrm{H}}[n]}{\delta n(\boldsymbol{r})} + \frac{E_{\mathrm{xc}}[n]}{\delta n(\boldsymbol{r})} \\ &= \frac{\delta T_{\mathrm{s}}[n]}{\delta n(\boldsymbol{r})} + V_{\mathrm{ne}}(\boldsymbol{r}) + v_{\mathrm{H}}(\boldsymbol{r}) + v_{\mathrm{xc}}(\boldsymbol{r}) \end{aligned} \tag{3.19}$$

where $V_{\mathrm{H}}(\boldsymbol{r})$ and $V_{\mathrm{xc}}(\boldsymbol{r})$ are the Hartree and exchange-correlation potentials, respectively. The minimization in Eq. (3.19) above is equivalent to the minimization of the total energy of non-interacting particle $E_{\mathrm{s}}[n]$;

$$0 = \frac{\delta E_{\mathrm{s}}[n]}{\delta n(\boldsymbol{r})} = \frac{\delta T_{\mathrm{s}}[n]}{\delta n(\boldsymbol{r})} + \frac{\delta V_{\mathrm{s}}[n]}{\delta n(\boldsymbol{r})} = \frac{\delta T_{\mathrm{s}}[n]}{\delta n(\boldsymbol{r})} + v_{\mathrm{s}}(\boldsymbol{r}) \tag{3.20}$$

where

$$v_s(\boldsymbol{r}) = V_{ne}(\boldsymbol{r}) + v_H(\boldsymbol{r}) + v_{xc}(\boldsymbol{r}) \tag{3.21}$$

Eq. (3.20) represents the energy of a non-interacting particle system exposed to an *effective* single-particle potential $v_s(\boldsymbol{r})$. At this point, the many-particle interacting ground state density can now be obtained by solving Kohn-Sham equation (i.e the Schrödinger equation of the non-interacting system). This equation is written as;

$$\left[-\frac{\nabla^2}{2} + v_s(\boldsymbol{r})\right]\phi_i(\boldsymbol{r}) = \epsilon_i\phi_i(\boldsymbol{r}), \quad i = 1, 2, \ldots N. \tag{3.22}$$

The obtained density is;

$$n(\boldsymbol{r}) = \sum_{i=1}^{N} f_i|\phi_i(\boldsymbol{r})|^2 \tag{3.23}$$

where where $\phi_i(\boldsymbol{r})$ is the single-electron wavefunction and f_i represents the occupation of the i^{th} orbital.

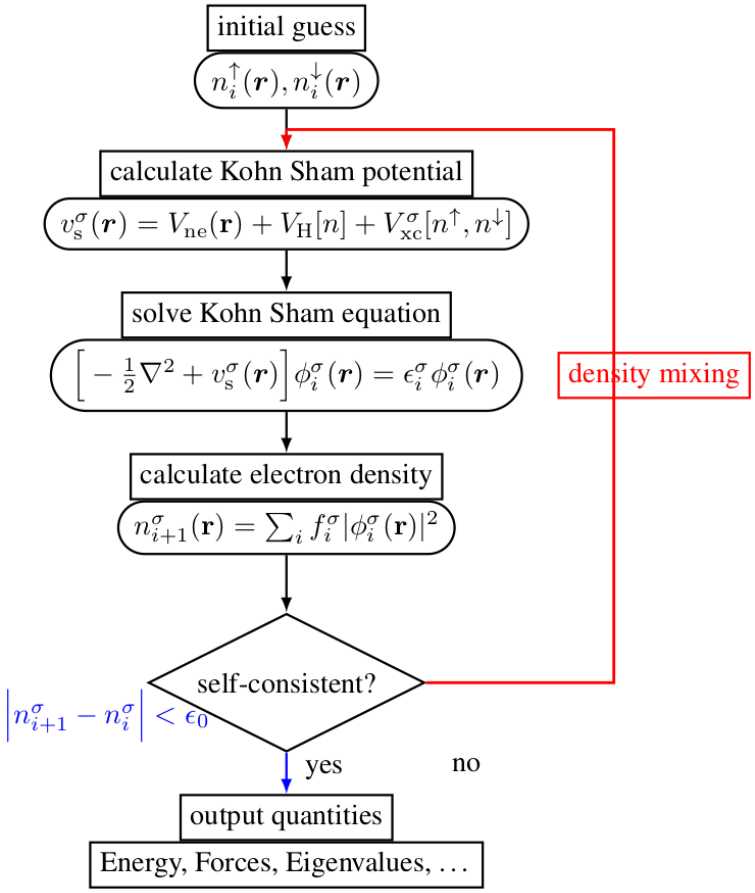

Figure 3.1: Kohn-Sham self-consistency routine.

In practice, the solution of Eq. (3.22) is obtained *self-consistently* considering that the potentials are functionals of $n(\boldsymbol{r})$. The self-consistent iteration begins with an initial guess for $n(\boldsymbol{r})$ and with that the effective potential v_s can be calculated. Eq. (3.22) can now be solved to obtain the single-particle wavefunctions $\phi_i(\boldsymbol{r})$, which is

further used to obtain the density $n(\boldsymbol{r})$ using Eq. (3.23). This process repeats until convergence (of the total energy E, density $n(\boldsymbol{r})$, forces and some other observable) is achieved.

In order to treat magnetism in DFT, spin polarization is considered such that the KS total energy functional $E[n]$ now becomes a functional of the spin up $n^{\uparrow}$ and spin down densities $n^{\downarrow}$ with the new energy functional written as $E[n^{\uparrow}, n^{\downarrow}]$. A schematic representation of the self-consistent iteration process in the spin-polarized formalism is shown in Fig. 3.1.

3.5 Exchange-correlation functional

One of the major difficulty in solving the KS equation (Eq. (3.22)) lies in the treatment of exchange and correlations $V_{\mathrm{xc}}(\boldsymbol{r})$. In principle the KS equation is exact but not in practice since the exact form of $V_{\mathrm{xc}}(\boldsymbol{r})$ is not known, and approximate functionals are instead used. For the purpose of the approaches used in this thesis, I will concentrate on the local density approximation (LDA) and the generalized gradient approximation (GGA).

3.5.1 Local density approximation

Here, the exchange correlation energy contribution is approximated by using the energy from uniform electron gas. Thus the density of the system is treated as homogenous. The form of this functional is;

$$E_{\mathrm{xc}}[n(\boldsymbol{r})] \simeq \int n(\boldsymbol{r})\epsilon_{\mathrm{xc}}[n(\boldsymbol{r})]d\boldsymbol{r} \tag{3.24}$$

where ϵ_{xc} is the exchange and correlation energy per particle of a homogeneous electron gas with density $n(\boldsymbol{r})$. The exchange contribution ϵ_{x} to this energy is that of a homogenous electron gas (HEG) with a known analytical form, while there is no known analytical form for the correlation contribution ϵ_{c} and they are obtained from the parametrization of uniform electron gas calculations by the Monte-Carlo method [64].

Since LDA is derived from the HEG, one expects that it should work well only for systems with slowly varying densities. But then, the applicability of LDA goes way beyond this and has proven to produce good results even for systems regarded as very inhomogeneous. However, one of the drawbacks of this approach is that it is known to overestimate the binding energy and lengths. For spin polarized systems the terminology is normally referred to as Local spin density approximation (LSDA).

3.5.2 Generalized gradient approximation

Another approach to approximate the E_{xc} is to not only consider the dependence on the density $n(\boldsymbol{r})$ and but also its gradient $\boldsymbol{\nabla} n(\boldsymbol{r})$, hence the name generalized gradient approximations (GGA). The form of this function is

$$E_{\mathrm{xc}}[n(\boldsymbol{r}] = \int n(\boldsymbol{r})\epsilon_{\mathrm{xc}}[n(\boldsymbol{r}), \boldsymbol{\nabla}(\boldsymbol{r})]d\boldsymbol{r} \tag{3.25}$$

One particular feature of this approximation is that it improves the binding energy estimation in comparison with the LDA. Functionals using this approximation has been constructed by Perdew and coworkers [65, 66] popularly called the Perdew-Burke-Ernzerhof (PBE) exchange-correlation functional. I have made the most use of this functional in this thesis.

3.6 Plane-wave basis set

In the self-consistent approach, to solve the KS equation in Eq. (3.22) a basis set is required to expand the KS wavefunction and in this section we discuss the basis set used for major calculations in this thesis. For a periodic system, the Bloch theorem allows to expand the single particle KS wavefunction ϕ_i in terms of plane-waves, which take the periodicity of the lattice and written as;

$$\phi_i(\boldsymbol{r},\boldsymbol{k}) = \exp(i\boldsymbol{k}\cdot\boldsymbol{r})u_i(\boldsymbol{r},\boldsymbol{k}) \tag{3.26}$$

where $\boldsymbol{k}$ is the wave vector limited in the first Brillouin Zone (BZ) of the reciprocal lattice $\boldsymbol{G} = m_1\boldsymbol{b}_1 + m_2\boldsymbol{b}_2 + m_3\boldsymbol{b}_3$ ($m_i \in \mathcal{Z}$, and $\boldsymbol{a}_i \cdot \boldsymbol{b}_j = 2\pi\delta_{ij}$) due to the symmetry of the crystal lattice and the index i runs over all states with occupations $f_i(\boldsymbol{k})$. $u_i(\boldsymbol{r},\boldsymbol{k})$ is the periodic function with same periodicity as the lattice, written as;

$$u_i(\boldsymbol{r},\boldsymbol{k}) = u_i(\boldsymbol{R}+\boldsymbol{r},\boldsymbol{k}). \tag{3.27}$$

In the above, $\boldsymbol{R} \equiv n_1\boldsymbol{a}_1 + n_2\boldsymbol{a}_2 + n_3\boldsymbol{a}_3$ ($n_i \in \mathcal{Z}$) is a translation vector of the crystal lattice. The periodic functions $u_i(\boldsymbol{r},\boldsymbol{k})$ have the form

$$u_i(\boldsymbol{r},\boldsymbol{k}) = \frac{1}{\sqrt{\Omega}}\sum_{\boldsymbol{G}} c_i(\boldsymbol{k},\boldsymbol{G})\exp(i\boldsymbol{G}\cdot\boldsymbol{r}) \tag{3.28}$$

where Ω is the volume of unitcell and thus, the Kohn-Sham orbitals are expanded as;

$$\phi_i(\boldsymbol{r},\boldsymbol{k}) = \frac{1}{\sqrt{\Omega}}\sum_{\boldsymbol{G}} c_i(\boldsymbol{k},\mathbf{G})\exp\Big(i(\boldsymbol{k}+\boldsymbol{G})\cdot\boldsymbol{r}\Big) \tag{3.29}$$

where $c_i(\boldsymbol{k},\boldsymbol{G})$ are complex numbers. Thus, the charge density in Eq. (3.23) can also be expanded in terms of the plane-wave basis. For usage and implementation in calculations, the summation of over $\boldsymbol{G}$ is truncated with a cutoff energy;

$$\frac{1}{2}\Big|\boldsymbol{k}+\boldsymbol{G}\Big|^2 \leq E_{\text{cut}} \tag{3.30}$$

In order to calculate quantities in the KS iterative process, the BZ integration was carried out using a finite number of k-points. This summation is written as:

$$\bar{Q}_i = \frac{\Omega}{(2\pi)^2}\int_{\text{BZ}} d\boldsymbol{k} Q_i(\boldsymbol{k}) = \sum_j w_j Q_i(\boldsymbol{k}) \tag{3.31}$$

where w_j are weighting factors. In practice, special k-points schemes can also be used to reduce to the number of points used in the integration. Such schemes include

the Monkhorst-Pack [67] approach were uniform k-point grid are used to sample the reciprocal space. Other such special schemes exists, such as Baldereschi point [68].

Aside from the plane-wave basis set mostly considered in the thesis, other types of basis set exist including linear combination of atomic orbitals (LCAO), Gaussian basis sets and the linearized augmented plane waves.

3.6.1 Pseudopotentials

Here, I discuss the pseudopotential (PP) concept that is always considered with the usage of the plane-waves basis. The expansion of Eq. (3.29) requires large energy cutoffs (a large number of plane waves) for plane waves that oscillate on short length scales. This corresponds to tightly bound core electrons that oscillate faster than the valence electrons. To minimize the number of plane waves N_{PW} for an increasing number of atoms and lattice dimension a PP concept was introduced. The idea of PP was first introduced by C. Herring [69] and later put into practice by J.C. Philips and L. Kleinman [70]. In the PP formalism, the core (c) and valence (v) electrons are distinguished. The core electrons are deeper in energy, mostly occupied, and do not contribute to the chemical properties of a material. Hence, in this formalism the fast oscillating wavefunctions at the core are replaced with smooth PPs, such that above a certain cutoff radius ($r > r_c$), the all-electron (AE) and the pseudo-function coincide. This reduces the number of plane-waves needed for calculations. An illustration of the PP concept is shown in Fig. 3.2.

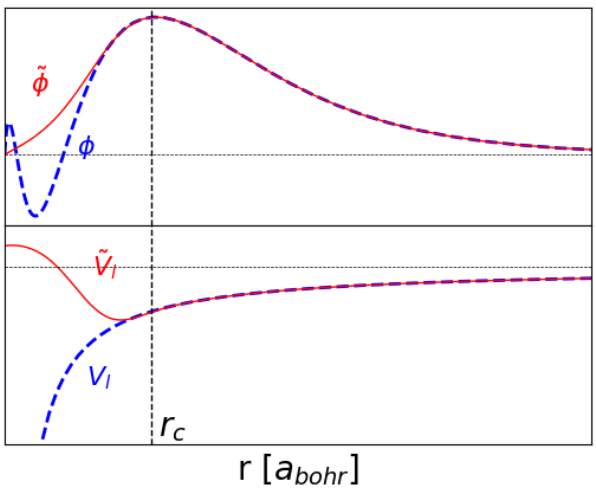

Figure 3.2: A schematic illustration of the pseudopotential formalism. The solid red-line represents the pseudo-wavefunction $\tilde{\phi}$ in the upper panel and pseudo-potential $\tilde{V}_l$ in the lower panel. The dashed blue-line represents the all-electron wavefunction ϕ in the upper panel (shows oscillations at small r) and all-electron potential $V_l \sim \frac{Z}{r}$ in the lower panel. For $r > r_c$ both the all-electron and pseudo functions coincide for each panel.

Types of pseudopotential

There are three commonly used types: norm-conserving [71, 72]; ultrasoft [73, 74]; and projector-augmented waves (PAWs) [75, 76]. When using PPs it is important to consider the *softness/hardness* [77] and its *transferability* [77, 78]. The transferability of PP characterizes how accurate PP mimics the all-electron wavefunction in different chemical environments. For large system size, the computational load increases and sometimes the PP are required to be soft as possible i.e. with small number of plane waves. Unfortunately, transferability and softness are usually challenging requirements especially for first row elements and transition metals and attempts to save computational cost and transferability often lead to harder PP.

- **Norm-Conservation pseudopotential (NCPP):** As the name implies this is the pseudopotential obtained by imposing the constraints [71, 72]

$$|\tilde{\phi}_i^{\mathrm{PP}}|^2 = |\phi_i^{\mathrm{AE}}|^2, \quad r > r_c \tag{3.32}$$

  (*i.e.* the total charge of the pseudo wavefunctions equals that of all-electron wavefunctions) where ϕ_i^{AE} is the all-electron wavefunctions and $\tilde{\phi}_i^{\mathrm{PP}}$ is the pseudo-wavefunctions. This constraints often results in hard pseudopotentials.

- **Ultrasoft pseudopotential (USPP):** Ultrasoft pseudopotentials relax the norm-conserving constraint to reduce the number of plane waves. Hence, the name ultra-soft pseudopotential [73, 74].

- **Projector Augmented-Wave pseudopotential (PAW):** This approach uses pseudopotential transformation operators that keeps the full core effects of all-electron wavefunctions [75, 76] by performing a linear transformation ($\mathcal{T}$) of a true wavefunction $|\phi_i\rangle$ to a pseudo-wavefunction $|\tilde{\phi}_i\rangle$.

$$|\phi_i\rangle \simeq \mathcal{T}|\tilde{\phi}_i\rangle \tag{3.33}$$

3.7 Structural optimization and Forces

Another important aspect in the electronic structure theory for this thesis is the structure optimization and relaxation of the forces acting on the atoms in the lattice. In the structure minimization algorithm and procedure used, calculations of the forces is required. The forces acting on the nuclei can be calculated using the force (Hellman-Feynman) theorem [79] within the BO approximation we have discussed earlier, This theorem states that;

$$\boldsymbol{F}_I = -\frac{\partial E}{\partial \boldsymbol{R}_I} = \langle \Psi_{\boldsymbol{R}} | \frac{\mathcal{H}}{\partial \boldsymbol{R}_I} | \Psi_{\boldsymbol{R}} \rangle \tag{3.34}$$

where $|\Psi_{\boldsymbol{R}}\rangle$ is the ground state wavefunction for the electrons and the nuclei. This theorem allows to compute the forces on the nuclei using the ground state wavefunction in DFT and further allow structural relaxations.

The procedure in practice for the structure optimization include: (i) calculate the Hellman-Feynman forces on each of the nuclei and use it to minimize the ionic

positions by any method such as gradient descent, conjugate gradient or Newton's method [80, 81] (ii) For the new ionic positions, minimize the electronic configuration (iii) compare the total energy and ionic position with the previous calculation and calculate the forces for the new ionic positions and then (iv) If the changes on forces and total energy fall below threshold limits, then the structure is minimized, otherwise continue with the minimization from step (i) above.

3.8 Ab-initio Strategy for muon calculations

Here, I outline the strategy used for the calculation and search of the muon sites in this thesis. For all calculations involving the identification of muon sites and or muon hyperfine fields, I have utilized the plane wave DFT approach as implemented in Quantum ESPRESSO [82–84]. In this thesis I have considered two approaches; the unperturbed minima of the electrostatic potential method and the supercell method.

- **Unperturbed electrostatic potential:** Here, since the muon (μ^+) has a positive charge it can be assumed that it will occupy the minima of the electrostatic potential after thermalization. The approach is to calculate the electrostatic potential of the unit cell without introducing the muon impurity. For example, in Fig. 3.3 the minima of the electrostatic potential is shown for UCoGe, where the muon can be assumed to stop at these sites. This method has been shown to work in systems where the muon charge is partially screened [85–87].

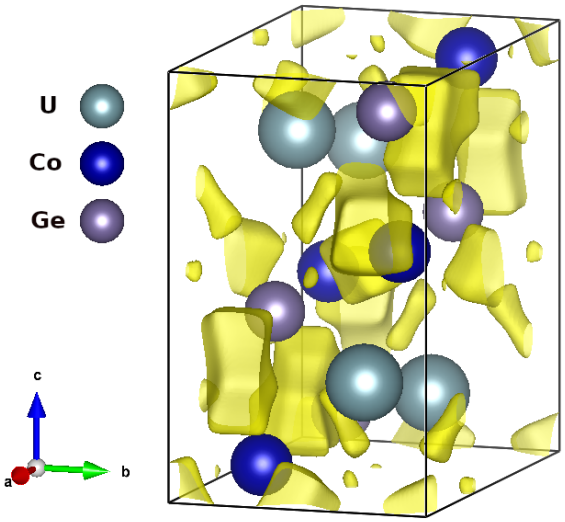

Figure 3.3: Unperturbed electrostatic potential of UCoGe (in yellow), U (cyan), Co (blue) and Ge (purple). The VESTA package [88] was used for this visualization.

However, the approach is found not to be realistic and *crude* in the case where screening of the muon charge strongly bond with electron to form muonium [23, 24]. In general, for the muon site(s) identification a more reliable and detailed approach is usually required, this leads us to the supercell approach.

- **Supercell method:** Here, the muon is treated as an impurity and for this a large cell, i.e supercell is required to avoid the artificial interaction of the muon with its periodic image. Conventionally, convergence of relevant physical quantities is used to determine the choice of the supercell size. For the plane-wave DFT approach used in this thesis, the hydrogen pseudopotenital is used to represent the muon, as this is an electronic problem where the muon is treated as a classical particle and its mass is not taken into account considering the BO approximation. The total positive and neutral charged of the entire supercell is usually used to designate the μ^+ or μ respectively.

  In the supercell method, the approach involves placing the muon at a number of initial guess positions while the forces acting on the muon and host atoms are optimized (i.e relaxed in DFT parlance) with the structure optimization method described above. In this relaxations, since the muon is not expected to alter the cell structure, the lattice parameters are kept fixed, usually at experimentally observed values or at earlier DFT optimized values. At the end of the relaxations the symmetry inequivalent muon relaxed positions corresponds to candidate muon stopping positions. One of the advantages of this approach is that it provides a means to study the effects of the muon in the lattice, which the earlier discussed approach do not avail.

  Further, one of the important concepts in this approach is the choice of the initial guess positions for the muon before relaxation. In this thesis, the initial guess are generated by sampling a uniform grid at the interstitial positions of the cell, such that each position has a distance of at least 1 Å from the host atoms. Then, applying the crystal symmetry, the number of the uniform grid positions is condensed into inequivalent positions, that are then used as the initial guess for the muon site search. An example is shown in Fig. 3.4 for UCoGe were the $4 \times 4 \times 4$ uniform grid positions are reduced to 10 symmetry inequivalent positions with the symmetry of the lattice.

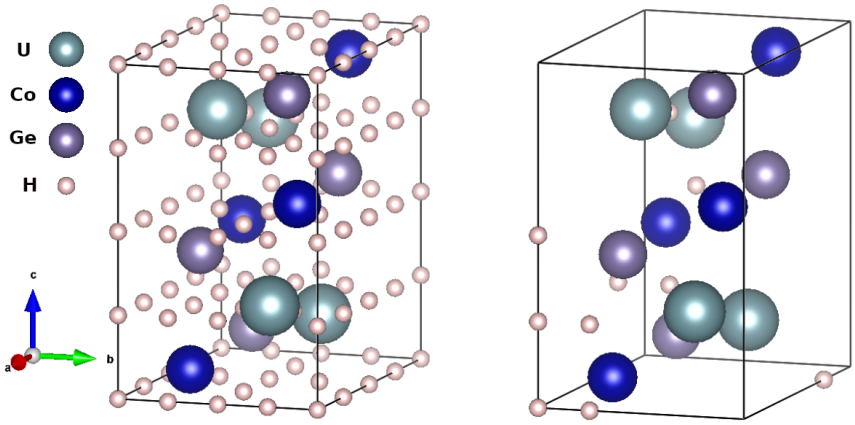

Figure 3.4: Left: Initial muon positions (pink) generated in a $4 \times 4 \times 4$ uniform grid in UCoGe. **Right:** Reduction by the space group [space group P_{nma}, No. 62] symmetry of UCoGe of the uniform grid to 10 symmetry inequivalent positions. U (cyan), Co (blue) and Ge (purple). The Fig. is visualised using VESTA program [88].

For some calculations in this thesis, in order to improve the initial guess positions, I have included the sites of the minima of the electrostatic potential described above in the initial guess positions. In all, this approach is computationally expensive and task demanding as large number of calculations (depending on the number of initial guess positions) and repeated runs are required to achieve convergence. However, one of the topics contained in this thesis is a new high throughput approach aimed at automating and managing these calculations.

CHAPTER 4

Simulation of muon spin polarization: Case study with Fluorides, Copper and MnSi.

In this chapter[1], I describe and summarize the approach introduced by Celio [22] about 30 years ago to study the spin dynamics of a static muon interacting via dipole interaction with surrounding nuclear spins. The aim is towards the numerical calculation and analysis of the time dependent spin polarization function of the muon within μSR. The studies is performed considering non-magnetic phase, in a temperature range where thermally activated muon diffusion does not average the dipolar interaction with nuclear magnetic moments to zero. Luckily, this situation is not so uncommon, since thermally activated muon diffusion is very often observed at temperatures higher than those of interest. The implementation of this approach is already contained in the UNDI (mUon Nuclear Dipolar Interaction) python code [89]. I have used this approach to simulate the muon spin polarization in Flourides, Copper and MnSi.

I continue to describe the interaction between the muon and its host in a sample and further the Celio approach.

4.1 The muon-nuclei Hamiltonian

The Hamiltonian that describes the interaction between the muon spin ($\mathbf{I}_\mu = \frac{1}{2}$) and the N neighboring nuclear spins ($\mathbf{I}_i$) is given by [22]:

$$\mathcal{H} = \mathcal{H}_{Z,\mu} + \sum_{i}^{N} \mathcal{H}_{Z,i} + \mathcal{H}_{\mathrm{Dip},i} + \mathcal{H}_{Q,i} + \sum_{i>j} \mathcal{H}_{\mathrm{Dip},ij} \tag{4.1}$$

where

[1]The contents of this chapter are already published on Journal of Computer Physics Communications: Pietro Bonfà, Jonathan Frassineti, **Muhammad Maikudi Isah**, Ifeanyi John Onuorah, and Samuele Sanna. **UNDI: An open-source library to simulate muon-nuclear interactions in solids.** DOI: 10.1016/j.cpc.2020.107719

$$\mathcal{H}_{Z,\mu} = -\hbar\gamma_\mu \mathbf{I}_\mu \cdot \mathbf{B}_{\text{Ext}} \tag{4.2}$$

$$\mathcal{H}_{Z,i} = -\hbar\gamma_i \mathbf{I}_i \cdot \mathbf{B}_{\text{Ext}} \tag{4.3}$$

$$\mathcal{H}_{\text{Dip,i}} = \frac{\mu_0\hbar^2}{4\pi}\gamma_i\gamma_\mu \left(\frac{\mathbf{I}_i \cdot \mathbf{I}_\mu}{r^3} - \frac{3(\mathbf{I}_i \cdot \mathbf{r})(\mathbf{I}_\mu \cdot \mathbf{r})}{r^5} \right) \tag{4.4}$$

$$\mathcal{H}_{Q,i} = \frac{eQ_i}{6I_i(2I_i-1)} \sum_{\alpha,\beta\in\{x,y,z\}} V_i^{\alpha\beta} \left[\frac{3}{2}\left(I_i^\alpha I_i^\beta + I_i^\beta I_i^\alpha \right) - \delta_{\alpha\beta} I_i^2 \right] \tag{4.5}$$

and

$$\mathcal{H}_{\text{Dip},ij} = \frac{\mu_0\hbar^2}{4\pi}\gamma_i\gamma_j \left(\frac{\mathbf{I}_i \cdot \mathbf{I}_j}{r_{ij}^3} - \frac{3(\mathbf{I}_i \cdot \mathbf{r}_{ij})(\mathbf{I}_j \cdot \mathbf{r}_{ij})}{r_{ij}^5} \right) \tag{4.6}$$

$\mathcal{H}_{Z,j}$ $j \in \{i,\mu\}$ is the Zeeman interaction of the nuclear magnetic moment for each nucleus i and muon μ subject to the external field $\boldsymbol{B}_{\text{Ext}}$. $\mathcal{H}_{\text{Dip},i}$ is the dipolar interaction between the muon and the nuclei. $\mathcal{H}_{\text{Dip},ij}$ is the dipolar interaction between the nuclei i and j. $\mathcal{H}_{Q,i}$ is the quadrupolar interaction with $\boldsymbol{V}_i$ being the electric field gradient (or EFG tensor) at nuclear site i. In Eq. (4.5), $\mathbf{I}_i$ is the spin operator of the nucleus i, characterized by the gyromagnetic ratio γ_i and nuclear quadrupole moment Q_i (NQM). In Eq. (4.2), $\mathbf{I}_\mu$ is the spin operator of the muon, that has gyromagnetic ratio γ_μ, and $\boldsymbol{r}$ is the vector from the muon to the various nuclei while $\boldsymbol{r}_{ij}$ is the distance between nuclei i and j. In general, in light of the r^{-3} decrease in the strength of the dipolar interaction, the sum is limited to a few muon nearest neighbours.

In order to interpret μSR data the theoretical knowledge of the form of the evolution of muon polarization function (denoted as $\boldsymbol{\mathcal{P}}(t)$) is required. Theoretically, an approximate or exact (or analytical) form of the polarization function $\boldsymbol{\mathcal{P}}(t)$ of a static muon interacting with neighbouring nuclear moments can be calculated for cases where the secular approximation for the dipolar interaction provides an approximation to the experimental $\boldsymbol{\mathcal{P}}(t)$. This formulation was first provided by Kubo and Toyabe named Kubo-Toyabe (KT) function (see Chap. 2). The theory of KT gives an approximate method for evaluating the time evolution of a classical spin ensemble, in zero and low longitudinal field where the local fields are assumed to be static and random with a Gaussian distribution.

This simplified model ignores both the crystal structure of the nuclear spins and their true quantum behaviour. Often both these aspects are not prominent and the central limit theorem justifies the agreement of the KT model with the data. This is not the case when nearest neighbor moments dominate the local field at the muon site. Notable cases are provided by Fluorides where two conditions are met: the moun binds to few F atoms, and ^{19}F is a 100% abundant $I = \frac{1}{2}$ nucleus with large gyromagnetic ratio $\gamma_{\text{F}} = 2\pi \times 40.05$ MHzT^{-1}. Another very interesting case is Cu metal, whose $I = \frac{3}{2}$ nuclei produce a dipolar field at the muon site, but interact also with the electric field gradient originated from the positive muon charge. A third interesting case is MnSi, where fine details of the magnetic structure lead to a very

precise muon site identification. It is interesting to compare this site identification with that predicted out of the accurate calculation of the local field from the nuclear spins in the paramagnetic phase where electron moments can be neglected.

In these cases a first order estimate can be produced by a proper quantum treatment of nearest neighbours. However, the inclusion of the quadrupolar effects and of second, third nearest neighbours already increases the spin manifold beyond tractability. Here, an approach pioneered by Moreno Celio [22] comes handy. In the following I described this approach and test it with the program UNDI in the simple cases outlines above. This has been my contribution to the publication [89] where the UNDI code was described. Since the aim is to validate the code the comparison is often not with the experimental data but rather with the nearest neigbour approximation or a known analytical function.

4.2 Celio approximation

Following the Celio approximation [22], we can now write the muon spin polarization $\mathcal{P}_\mu(t)$ as ;

$$\mathcal{P}_\mu(t) = \mathrm{Tr}\left[\rho e^{(i\mathcal{H}t/\hbar)}\sigma_\mu e^{(-i\mathcal{H}t/\hbar)}\right] \tag{4.7}$$

where $\sigma_\mu = 2\mathbf{I}_\mu$ are the Pauli operators and ρ is the density matrix.

For a system with N randomly oriented distinct nuclear spins (unpolarized), the initial density matrix is given as

$$\rho = \frac{1}{2\prod_{i=1}^{N}(2I_i+1)}\left[\mathcal{I} + \mathcal{P}_\mu(0)\sigma_\mu\right] \quad ;\mathcal{P}_\mu(0) = 1 \tag{4.8}$$

where $\mathcal{I}$ is an identity operator, I is a nuclei spin. The general orientation of initial muon spin polarization with respect to crystallographic axis is $\sigma_\mu = \sin\theta\cos\beta\sigma^x + \sin\theta\cos\beta\sigma^y + \cos\theta\sigma^z$ [90]. From the definition of the Hamiltonian $\mathcal{H}$ in Eq. (4.1) $\mathcal{H}_{\mathrm{Dip},i}$ does not commute and an analytical solution of $\mathcal{P}_\mu(t)$ is not possible for a large Hilbert space dimension $d = \prod_{i=1}^{N} 2(2I_i+1)$. However, we can resort to Celio approximations [22] based on Suzuki-Trotter expansion [91] and random phase approximations (RPA).

Trotter expansion: The trotter expansion is based on product of formulas. Suppose $\mathcal{H} = \sum_{i=1}^{N}\mathcal{H}_i$ be a Hamiltonian on which each $\mathcal{H}_i$ does not commute with one another. Assuming $\mathcal{H}$ is time independent , the evolution of $\mathcal{H}$ for time t is define by the unitary operator $e^{-i\mathcal{H}t/\hbar}$. When t is small, the Trotter expansion is $e^{-i\mathcal{H}_1 t/\hbar}\cdots e^{-i\mathcal{H}_N t/\hbar}$, and for a long time t, we may divide the evolution of $\mathcal{H}$ into k Trotter steps and simulate each stem with an error ζ/k. The Trotter expansion number k is chosen to be sufficiently large so that the error vanishes to a first order. This can be expressed as;

$$e^{-i\mathcal{H}t/\hbar} = e^{-i\sum_{i=1}^{N}\mathcal{H}_i t/\hbar} \simeq \lim_{k\to\infty}\left(e^{-i\mathcal{H}_1 t/k\hbar}\cdots e^{-i\mathcal{H}_N t/k\hbar}\right)^k \tag{4.9}$$

Now we can recast Eq. (4.7) as

$$\boldsymbol{\mathcal{P}}_{\mu}(t) = \mathrm{Tr}\left[\rho\sigma_{\mu}(t)\right] \tag{4.10}$$

where

$$\sigma_{\mu}(t) = e^{(i\mathcal{H}t/\hbar)}\sigma_{\mu}e^{(-i\mathcal{H}t/\hbar)} \tag{4.11}$$

Choosing a representation where $\sigma_{\mu} = \sigma_{\mu}^{z}$ is diagonal, any complete sets of $\{|\psi\rangle\}$ can be used to calculate Eq. (4.10). As already proven, the trace of a matrix is independent of the basis chosen. In Schrödinger picture Eq. (4.10) reads as:

$$\boldsymbol{\mathcal{P}}(t) = \sum_{n=1}^{d} w_n \left\langle \psi_n(t)|\sigma_{\mu}^{z}|\psi_n(t)\right\rangle \tag{4.12}$$

where

$$|\psi_n(t)\rangle = e^{-i\mathcal{H}t/\hbar}|\psi_n(0)\rangle \tag{4.13}$$

The coefficient w_n can be described as the probability of finding the spin system, in the pure state $|\psi_n(0)\rangle$ at time $t = 0$ and can be determined from density matrix ρ in Eq. (4.8)

$$w_n = \begin{cases} \frac{2}{d}, & \text{if} \quad \sigma_{\mu}^{z}|\psi_n(0)\rangle = +|\psi_n(0)\rangle, \\ 0, & \text{if} \quad \sigma_{\mu}^{z}|\psi_n(0)\rangle = -|\psi_n(0)\rangle. \end{cases} \tag{4.14}$$

Considering that we can neglect the dipolar nuclei-nuclei interaction $\mathcal{H}_{\mathrm{Dip},ij}$ as they have negligible effects in the μSR time scale, we can re-write Eq. (4.1) as $\mathcal{H} = \sum_{i}^{N}\mathcal{H}_i$. This is such that each $\mathcal{H}_i$ acts in a small subspace of dimension $2(2I+1)$. Thus, the problem of diagonalizing a huge $d \times d$ matrix is replace by diagonalizing a single N matrix $\mathcal{H}_i$ according to the Suzuki-Trotter expansion given as;

$$e^{-i\mathcal{H}t/\hbar} = \lim_{k\to\infty}\left[\prod_{i=1}^{N} e^{\left(-i\frac{\mathcal{H}_i}{k}\frac{t}{\hbar}\right)}\right]^{k} \tag{4.15}$$

Thus, Eq. (4.13) becomes

$$|\psi_n(t)\rangle = e^{-i\mathcal{H}t/\hbar}|\psi_n(0)\rangle \tag{4.16}$$

$$= \lim_{k\to\infty}\left[\prod_{i=1}^{N} e^{\left(-i\frac{\mathcal{H}_i}{k}\frac{t}{\hbar}\right)}\right]^{k}|\psi_n(0)\rangle \tag{4.17}$$

where the largest value of k is chosen to make sure that an error in the depolarization signal is negligible within a μSR time window. For all $d/2$ possible initial states computing Eq. (4.10) becomes computationally expensive for increasing d. This issue can be resolved by invoking the random phase approximation (RPA) method. In this case, the idea of RPA is that for each possible initial states $|\psi_l(0)\rangle$ one chooses a random phase of λ_l's, chosen from a uniform distribution in the interval $(0, 2\pi)$ subjected to a normalization condition of a_l so that

$$|\phi(0)\rangle = \sum_{i=l}^{d_{\mathcal{H}}/2} a_l e^{i\lambda_l} |\psi_l(0)\rangle \tag{4.18}$$

and

$$\sum_{i=l}^{d_{\mathcal{H}}/2} |a_l|^2 = d_{\mathcal{H}}/2 \cdot |a_l|^2 = 1 \tag{4.19}$$

where $a_l = \sqrt{\frac{2}{d_{\mathcal{H}}}}$.
Then, at a later time t , $|\phi(t)\rangle$ is:

$$|\phi(t)\rangle = \sum_{l=1}^{d_{\mathcal{H}}/2} \sqrt{\frac{2}{d_{\mathcal{H}}}} e^{i\lambda_l} |\psi_l(t)\rangle \tag{4.20}$$

and the matrix element in Eq. (4.12) then becomes:

$$\langle\phi(t)|\sigma_\mu|\phi(t)\rangle = \sum_{l=1}^{d_{\mathcal{H}}/2} \left(\frac{2}{d_{\mathcal{H}}}\right) \langle\psi_l(t)|\sigma_\mu|\psi_l(t)\rangle + \sum_{l,n=1,l\neq n}^{d_{\mathcal{H}}/2} \left(\frac{2}{d_{\mathcal{H}}}\right) e^{i(\lambda_l-\lambda_n)} \langle\psi_l(t)|\sigma_\mu|\psi_n(t)\rangle \tag{4.21}$$

The first term on the R.H.S of Eq. (4.21) is the exact solution of Eq. (4.12) with $w_n = 2/d_{\mathcal{H}}$, and second term tends to zero and in a limit of large $d_{\mathcal{H}}$ can be considered as a small correction. In order to obtain an exact signal $\mathcal{P}(t)$, one has to calculate the matrix element over various random initials states and average over all signal.

4.3 UNDI code

The implementation of the Celio approximation to compute the muon spin polarization is contained in a python package **UNDI**, published to assist in analyzing μSR data. The acronym **UNDI** stands for m**U**on **N**uclear **D**ipolar **I**nteraction. The code can be used to compute both LF (or ZF) and TF-μSR polarization signals as a function of time. The code also has a feature to align initial muon polarization to a given direction, as well as performing the rotation of various quantities like EFG tensors, the atomic and muon positions.

4.3.1 Input parameters

The current version of UNDI accepts the following inputs defined by a list of dictionaries. The details for the muon and the nuclei can be set with the following keys:

- **`Position`** : 3D vector, the position of the nucleus or the muon in Cartesian coordinates.

- **`Label`** : string, this can be either '**`mu`**', a chemical symbol or the isotope name, for example Al or 63Cu.
- **`Spin`** : real, the spin of the nucleus or of the muon (optional, the mendelev package is used to obtain the spin value using the information in **`Label`**).
- **`Gamma`** : real, the gyromagnetic ratio of the muon/nucleus (optional).
- **`ElectricQuadrupoleMoment`** : real, the nuclear quadrupole moment (optional).
- **`EFGTensor`** : 3D matrix, the EFG tensor in Cartesian coordinates (optional, default zero).
- **`OmegaQmu`** : real, the quadrupole coupling frequency of the nuclear spin due to the EFG generated by the muon, (optional, default zero)

All details are optional except for the **`Label`** and the **`Position`**. Missing information are taken from the Mendeleev package and the most abundant isotope is selected by default. A message warns the user when multiple isotopes should be considered or when the potentially interacting nuclei are only a fraction of the natural occurring isotopes (in both cases the threshold is set to 99% relative abundance). All quantities should be provided and are returned by the code in SI units. A self-explanatory image-shot of the input python script is shown in Fig. 4.1 for Copper, that I discuss in the next section.

In UNDI, if quadrupolar contributions are present, they are of two parts: the 3D **`EFGTensor`** ($I > 1/2$) of the nuclear spin due to the crystal EFG and **`OmegaQmu`** quadrupole coupling constant of the nuclear spin due to the EFG generated by the muon. These quantities must be provided by the user and often estimated from first principle calculation otherwise it is assumed to be zero.

Also, there is a possibility to rotate the direction of the external field.For more on unit conventions on UNDI, installation, and dependencies look at the official github page and published article [89].

```
import numpy as np
import matplotlib.pyplot as plt
from undi import MuonNuclearInteraction

# The Tetrahedral (T) muon site in Cu
# and it is nearest neighbors.

angtom=1.0e-10 # m
a=3.6212625504 # Cu lattice constant,
# in Angstrom

# Electric Quadrupole Moment of
# Copper
Cu_Q_moment = -0.211e-28 # m^2
OmegaQmu =  3.2e6 # s^-1

atoms = [
                {'Position': np.array([0.25,0.25,0.25])*a*angtom,
                'Label': 'mu'},
                {'Position': np.array([0.5,0.5,0.0])*angtom*a,
                'Label': '63Cu',
                'ElectricQuadrupoleMoment': Cu_Q_moment,
                },
                {'Position': np.array([0.0,0.5,0.5])*angtom*a,
                'Label': '63Cu',
                'ElectricQuadrupoleMoment': Cu_Q_moment,
                },
                {'Position': np.array([0.5,0.0,0.5])*angtom*a,
                'Label': '63Cu',
                'ElectricQuadrupoleMoment': Cu_Q_moment,
                },
                {'Position': np.array([0.0,0.0,0.0])*angtom*a,
                'Label': '63Cu',
                'ElectricQuadrupoleMoment': Cu_Q_moment,
                }
                ]
```

Figure 4.1: (a) A sample python script for UNDI input initialization. Here, this is for the tetrahedral muon site in FCC Copper discussed in the next section.

4.3.2 Setting the UNDI environment

The muon depolarization signal can be computed exactly or using the Celio approximation. For the former, the setting is initialized in UNDI with the `MuonNuclearInteraction` class, called in the script as;

```
NS=MuonNuclearInteraction(atoms,external_field=[0.,0.,0.001])
```

where `atoms` contains the list of dictionary as define in Fig. 4.1 and `external_field` is in this case, 1 mT applied along z. Then the approximated signal by Celio approach is called as:;

```
celio_signal=NS.celio(tlist,k=2)
```

where k is the Suzuki-Trotter expansion number and `tlist` is a 1D NumPy array containing the 'time' list to be used for the computation of the muon polarization. The sample can be rotated such that the muon spin is aligned to a specific direction say $\langle 100 \rangle$ or $\langle 111 \rangle$, e.t.c., this can be done by;

```
NS.translate_rotate_sample_vec(np.array([1.,1.,1.]))
```

4.4 Muon polarization signal in selected materials

In this section I discuss the muon polarization signal in Flourides, Cu and MnSi. Also, I further show how this approach with UNDI can be used along with other theoretical or *ab-initio* methods to predict or identify muon stopping sites or to predict μSR experimental features.

4.4.1 Fluorides

In this example, I compute the muon polarization function determined by the interaction between a spin-polarized muon and the neighbouring nuclei in a fluoride compound. In flourides, the muon is preferentially drawn towards highly electronegative fluorine atoms where the muon spin may dipole couple strongly with a small number of fluorine nuclei spins via the Hamiltonian term in Eq. (4.4). In the case of insulating alkali metal fluorides [92], for example, the muon and two fluorine form a strong linear "hydrogen bond" with the nominal fluorine-fluorine (F-F) bond distance of 2.30 Å [92] (approximately twice the fluorine ionic radius) [the so-called F-μ-F state]. In some compound such as the molecular material polymer, other F-μ-F complexes may be formed, including interaction of muon with a single F, and more complicated arrangements [23, 24, 93]. In each of these cases, the muon spin becomes entangled with the spins on nearest neighbors (nn) fluorine nuclei (correlated with its environment), and the muon's polarization gives rise to an oscillatory time-dependence of the muon polarization, $\boldsymbol{\mathcal{P}}(t)$. These oscillations can be interpreted as a *coherent* exchange of spin polarization between the initial spin-polarized muon and unpolarized fluorine nuclei. The muon-spin polarization also *decoheres* into the environment, and hence causes a relaxation of the oscillatory signal. Recently, it was shown that the the decoherence nature of the F-μ-F state by including a more distant next nearest neighbors (nnn) flourine nuclei from the muon in the simple cubic fluorides of CaF_2 and NaF [94].

Here, I apply the procedure used for CaF_2 and NaF [94] on LiF to further demonstrate that DFT calculations can be used to determine muon-stopping sites and gain more insight on the muon's perturbation of its local surrounding environment. I consider three cases: (i) the μ-F state, (ii) the F-μ-F state, and (iii) the F-μ-F state with nnn fluorine nuclei found in LiF lattice.

For linear μ-F, the Hamiltonian in Eq. (4.1) in zero applied magnetic field can be diagonalised analytically [93], inserting the eigenvalues and eigenstates into Eq. (4.7) yields [2] the muon spin polarization $\mathcal{P}_z^{\mu\text{-F}}(t)$ along z as;

$$\mathcal{P}_z^{\mu\text{-F}}(t) = \frac{1}{6}\left[1 + \cos\left(\omega_D t\right) + 2\cos\left(\frac{1}{2}\omega_D t\right) + 2\cos\left(\frac{3}{2}\omega_D t\right)\right] \tag{4.22}$$

For an axially symmetric F-μ-F complex, at first approximation [i.e. neglecting coupling between the F-F nuclear], the analytical entangled muon-spin polarization function is given as;

[2] Performed by using an appropriately weighted powder average over all directions.

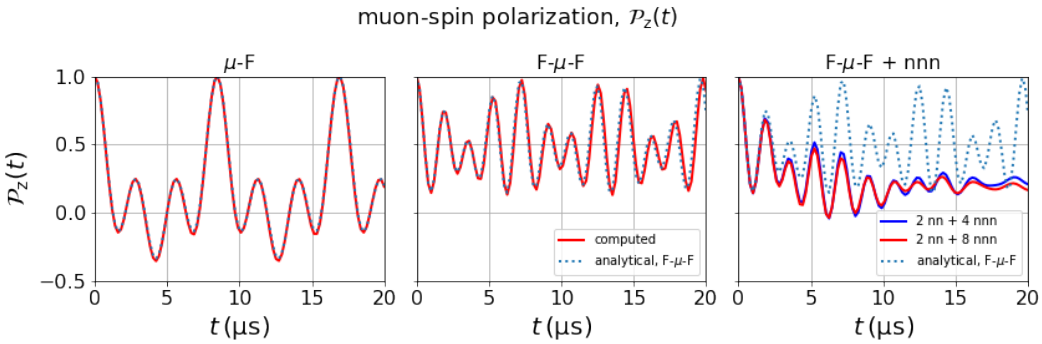

Figure 4.2: A Comparison of $\mathcal{P}_z(t)$ for μ-F, F-μ-F (with 2 nn F nuclei) and F-μ-F + nnn (with 2 nn and 4-8 nnn nuclei). The 4 and 8 nnn nuclei are at a distance of 2.47 Å and 3.23 Å respectively. The solid line is the computed approximate signal, dotted line (blue line) is the analytical function of the corresponding μ-F and F-μ-F shown in Eq. (4.22) and (4.23) calculated at $r = 1.15$ Å.

$$\mathcal{P}_z^{\text{F-}\mu\text{-F}}(t) = \frac{1}{6}\left[3 + \cos\left(\sqrt{3}\omega_D t\right) + \left(1 - \frac{1}{\sqrt{3}}\right)\cos\left(\frac{3-\sqrt{3}}{2}\omega_D t\right) + \left(1 + \frac{1}{\sqrt{3}}\right)\cos\left(\frac{3+\sqrt{3}}{2}\omega_D t\right)\right] \tag{4.23}$$

$$\omega_D = \frac{\mu_0}{4\pi}\frac{\gamma_\mu \gamma_F \hbar}{r^3} \tag{4.24}$$

where r is the μ-F distance, $\gamma_F = 2\pi \times 40.061$ MHzT^{-1} and γ_μ is ^{19}F and muon gyromagnetic ratio respectively. Clearly, the analytical form of μ-F and F-μ-F neglects F-F interactions [which provides a small correction to the relaxation] and the nnn μ-F interaction.

In order to analyze the interaction of the muon and the neighboring F ions, I computed the muon spin polarization considering appropriate powder averaging with the Celio approximation described above. The information of muon-stopping site and its perturbation of the neighbor nuclei in LiF have been taken from the earlier DFT calculation [23, 24]. The distance between the muon and its neighboring F nuclei is 1.15 Å, in excellent agreement with the experiment [92]. In the simulation of the muon spin polarisation, I have restricted the Hilbert space to include only nearest-neighbour and few next nearest neighbour (nnn) F nuceli. F has nuclear spin $I = \frac{1}{2}$, hence no quadrupolar interactions are considered.

The simulation results of the muon-spin polarization in zero applied external field for the for μ-F, F-μ-F and F-μ-F + nnn are plotted in Fig. 4.2. The F-F coupling contribution are not considered in this results as, they have negligible effects on $\mathcal{P}_z(t)$ [22] over the μSR time range. Also in the plot the simulated muon-spin polarization with the Celio's approach are compared to the analytical functions in Eq. (4.22) and (4.23), of which they are both in agreement for μ-F and F-μ-F. It can be seen that $\mathcal{P}_z(t)$ consists of three oscillations frequencies [excluding the zeroth frequency]

corresponding to three distinct transition energy levels, which would not have been observed using the Kubo-Toyabe relaxation function (see Chap. 2). But then nnn F nuclei are introduced, the calculated muon polarization deviates from the analytical one for F-μ-F. This is the quantum decoherence of the F-μ-F complex with nnn Ref. [94].

These results therefore demonstrate that the details of the oscillatory signal are able to distinguish the nature of the quantum entangled state of the muon and neighboring nuclei. Also, from the definition of ω_D in Eq. (4.24), one can evaluate the μ-F distance r and thus the muon-stopping site including the perturbation induced by the muon to the neighboring nuclei are determined, which are all in agreement and validate the DFT approach.

.

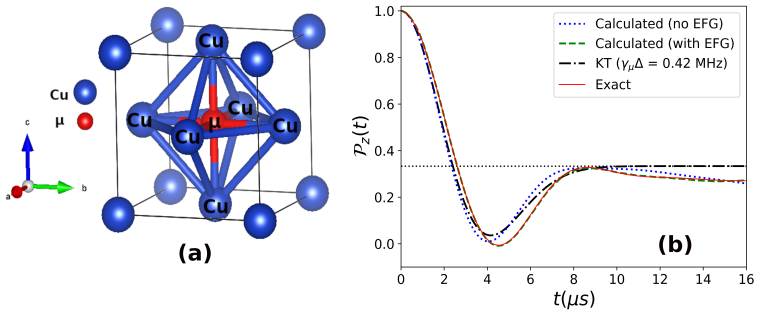

Figure 4.3: (a) The unit cell of face-centred-cubic Copper (Cu, blue sphere) lattice with octahedral (O, red sphere) muon site at (0.5, 0.5, 0.5). 6 Cu nucleus included in the calculation of $\mathcal{P}_z(t)$ for this muon site. (b) Comparison of the zero field KT function (dash-dotted line) with the calculated muon polarisation obtained from the Celio approximation described above of a muon at the octahedral site interacting with Cu on the first nearest neighbours in the absence (presence) of the EFG induced by the muon. The solid line is the exact calculation [90]. The Z-axis of muon spin polarisation is taken parallel to the $\langle 111 \rangle$ direction.

4.4.2 Copper

In a more rigorous example, here, I discuss the muon polarization function of the nuclear-spin in Cu interacting with the muon in zero or longitudinal external field. The calculation of muon spin polarization $\mathcal{P}_z(t)$ using Celio approximation is performed in a face-center-cubic (FCC) geometry. The purpose of this calculation is to show the effects of the applied field and influence of quadrupolar interactions when analyzing experimental data with simulations.

In Cu FCC two candidates muon-stopping sites were identified with DFT calculations, the octahedral (O) and tetrahedral (T) site. The diffusion of muon in Cu was studied experimentally by μSR in various temperature ranges [55, 95–97], where it has been shown that the muons occupied octahedral site at low temperatures. In Fig. 4.3, pristine Cu FCC unitcell is plotted together with the muon at the octahedral position (red sphere). The distance between the muon and the nearest

Cu nuclei $d_{\mu-\mathrm{Cu}}$ is 1.81 Å. In this calculation, we have considered the most naturally abundant (69.1%) Cu isotope, ^{63}Cu with $I = \frac{3}{2}$, gyromagnetic ratio $\gamma_{\mathrm{Cu}} = 7.1088 \cdot 10^{7}\mathrm{rad(Ts)}^{-1}$ and nuclear quadrupole moments of $Q_{\mathrm{Cu}} = -2.2 \cdot 10^{-29}\mathrm{m}^2$ [98].

The muon polarization function is then calculated for a muon interacting with $N_{\mathrm{Cu}} = 6$ nuclei [neglecting Cu-Cu interactions]nin a octahedral (O) arrangement, respectively. The dimensionality of the Hamiltonian matrix grows as $d_{\mathcal{H}} = 2 \times 4^{N_{\mathrm{Cu}}}$ and with $N_{\mathrm{Cu}} = 6$ and $d = 8192$, and the simulation within the Celio approximation shows good agreement with the exact calculations [90]. The calculated muon polarization $\mathcal{P}_z(t)$ for zero field along the $\langle 111 \rangle$ direction of initial muon spin polarization with and without the effect of EFG are shown in Fig. 4.3. The dash-dotted line represents the KT function of the zero field relaxation function given at $\gamma_\mu \Delta = 0.42$ MHz (see Eq. (2.14) in Chap. 2). At long times, the calculated $\mathcal{P}_z(t)$ deviates from the KT function as there is no recovery of asymptotic $\frac{1}{3}$.

We now investigate the influence of including the muon induced EFG on $\mathcal{P}_z(t)$. The muon induced EFG is introduced in the code using the input parameter **`OmegaQmu`**. The EFG arises from the fact that the muon destroys the cubic symmetry of its neighbouring Cu nuclei and exerts an electric field on them. It is assumed in Eq. (4.5) that the electric field gradient on each Cu nucleus is axially symmetric and is the only field gradient present. The value used for quadrupolar coupling constant [**`OmegaQmu`** = 3.2 MHz] of the Cu nuclear spin due to the EFG generated by the muon (at the O site) is taken from Ref. [96]. In figure 4.3, a comparison of the calculated signal with the exact calculations in zero applied field shows that the EFG is required to recover the experiment and also confirms that the octahedral site is where the muon sits.

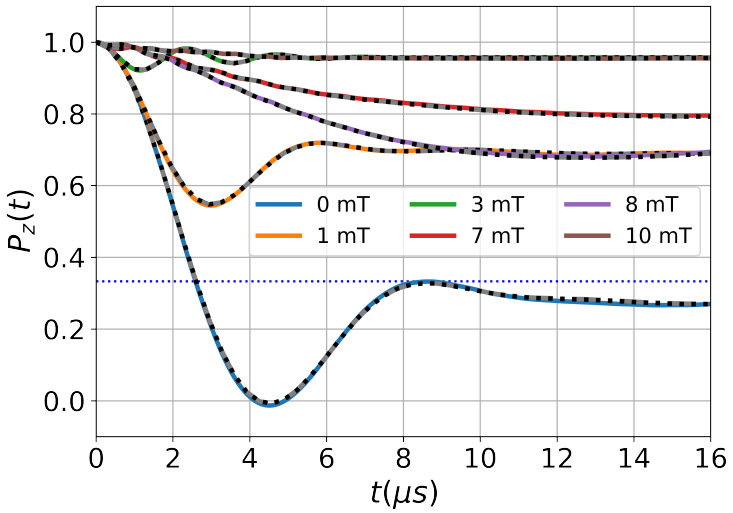

Figure 4.4: Muon spin polarization along the $\langle 111 \rangle$ direction as a function of time for various applied longitudinal fields. The exact result (dotted line) is compared with the approximated one (solid continuous lines). Four repetitions of Celio approximation were used in this case (The signal is orientation dependent except at ZF).

To investigate the influence of the Zeeman interaction in Eq. (4.1) for muon at the O site with the effect of muon induced EFG, the muon spin polarization is

calculated along $\langle 111 \rangle$ direction for arbitrary longitudinal field ranging from 0 to 10 mT. Figure 4.4 shows the calculated muon polarization functions and this agrees with the earlier published results by Celio [22]. The exact (dashed-dotted lines) and Celio approximated (solid continuous lines) methods are compared. One interesting feature of Fig. 4.4 occurs around the field $\approx$ 8 mT, the level-crossing resonance (LCR). This level-crossing resonance occurs approximately when the muon Zeeman energy splitting is approximately equal to the Cu quadrupolar splitting which resulted due to the electric field gradient produced by the muon. The LCR provides an extremely sensitive probe of the muon site. If the muon were to occupy a different site, with a different muon-copper separation or different number of nuclei involved the form of the muon spin depolarization function will change.

4.4.3 MnSi

Here MnSi is considered. For this sample the magnetic order and the muon site are well described and already published [41, 99, 100]. A recent publication has also clarified the uncertainty related to the presence of two interstitial muon sites [99]. Multiple experimental and computational evidences have confirmed that only a single muon site is occupied in the sample, differently from previous indications [101].

Here, we give yet another confirmation of the position of the muon site based on the dipolar interaction between the muon and Mn atoms in the sample. In order to do so the EFG of $V_{zz} = 3.1 \cdot 10^{20}\ \mathrm{V}/m^2$, (calculated from DFT) at Mn sites was used [89].

Figure 4.5 compares the predicted polarization function of the muon using the known muon site [102–104] and the bulk EFG, with the experimental data taken at 150 K published in Ref. [99]. While the curve obtained without taking into account the quadrupolar interaction drastically overestimates the depolarization, a better agreement is found when adding the bulk EFG. Still a small but noticeable deviation exists. This could be partially due to the difference between the ab initio estimate end the experimental value of the EFG and to the neglected contribution originating from the muon, which however is shown to be a small perturbation by comparison of the μSR data with the NMR data [99]. We mention that a perfect agreement is recovered by shifting the muon position slightly closer to the nearest neighbouring Mn atoms, thus proving an estimate of the accuracy based only on the data from the unperturbed crystal. Interestingly, the zero field polarization function can also be used to identify the possible muon sites. This has been previously attempted with the approach proposed here in $La_{2-x}Sr_xCuO_4$ [105], but starting from the previous knowledge of a handful of possible muon sites

Here we compute instead the expected signal for a grid of $10 \times 10 \times 10$ positions in the unit cell. While faster options are available[3], this example shows that arbitrarily accurate quantum simulations as implemented in UNDI can already be used to this aim. Indeed the whole simulation, that also requires powder averages, takes a few hours on a single core of a consumer level laptop.

[3]For example, it has been shown that for sufficiently large spins a classical approach is accurate enough and very efficient. Alternatively, the secular approximation can be used to estimate the second moment of the field distribution causing the depolarization.

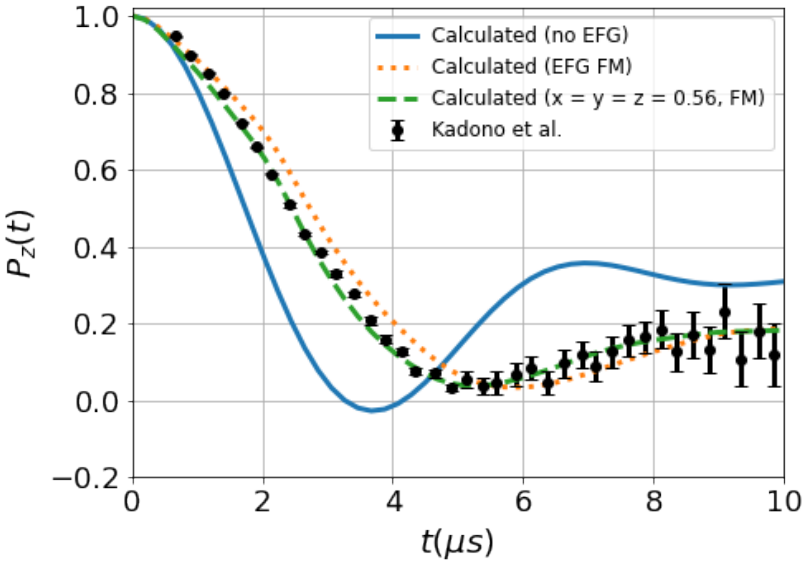

Figure 4.5: Expected muon polarization in the presence (absence) of the EFG on Mn atoms in MnSi, with Mn in (0.138,0.138,0.138) and the known muon site having fractional coordinates (0.532, 0.532, 0.532). When considering only the bulk EFG as estimated from DFT, the best agreement with the experiment is obtained with a muon position slightly closer to the three nearest neighbouring Mn nuclei, namely (0.56, 0.56, 0.56).

In order to find the candidate sites we calculate the sum of the squared deviations between the experimental points of Fig. 4.5 and the calculated signal for each position of the grid in the time window between 0 and 5 μs. Each simulation is performed by searching for the nearest neighboring Mn nuclei up to 1.6 times the shortest bond length (roughly corresponding to a 1/4 ratio between the strength of the dipolar interaction for the nearest and the farthest Mn nucleus) or up to 5 nearest neighbours. The convergence of the Celio method is checked at runtime for each point and the powder average is performed with the method of Ref. [106]. Interstitial positions closer than 1 Å to Mn or Si atoms are rejected.

The set of points that best reproduce the experimental signal are shown in Fig. 4.6 where we only add the points that have up to twice the best sum of square deviations from the experimental points. The muon position is also visible as a green sphere. Two interstitial positions are found to be compatible with the zero field μSR observations: the best match is found with interstitial points shown in yellow, very close to the known muon site, while a second set of points (orange) lie just slightly more than 1 Å far from Si atoms. This second best match is unlikely to be present given the short muon to Si distance. A third set of points (red) is again located close to the known muon site.

Incidentally, similar results and conclusions were obtained in Ref. [101], which however required a single crystal sample and a number of transverse field measurements.

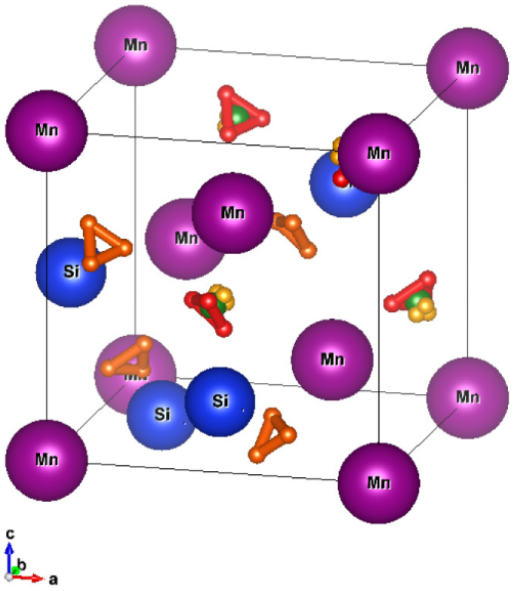

Figure 4.6: Set of points providing the best agreement with the experimentally measured zero field μSR data. The color code from yellow to red reflects best to worse match.

4.5 Conclusion and further outlook

In conclusion, I have summarized the Celio approach for simulating the muon spin polarization and have demonstrated this approach by computing the time evolution of muon-spin polarization function in fluorides, Copper and MnSi. These cases also provide a means to identify muon-stopping sites where dipole interactions provide a quantum mechanical fingerprint that may be used to identify the muon state. With the cases considered, one can immediately see the potentialities of an accurate analysis of muon nuclear interactions for the determination of the physical properties of the sample, such as the disentanglement of magnetic interactions of electronic and nuclear origin or the accurate estimation of the influence of charge ordered states on μSR signals.

CHAPTER 5

Magnetic ground state of Fe_2P from experimental and ab-initio modelling perspective.

In this chapter[1], I present an accurate description of the magnetic transition and the ground state order of Fe_2P with two local probes: μSR and NMR. Also, I further demonstrate by *ab initio* methods that characterizing the hyperfine coupling parameters of ^{31}P nuclei and of the muon in its stable interstitial site allow to predict the experimental features of NMR and μSR spectra of Fe_2P.

5.1 Introduction

Fe_2P based alloys have attracted much interest in the field of magnetocaloric refrigeration applications due to their first-order magnetic transitions (FOMT) coupled to a magnetoelastic transition, which gives rise to a giant magnetocaloric effect in the vicinity of their Curie temperature [107]. This transition has been shown to be tunable across room temperature by suitable (Fe, Mn) and (P,Si)/(P,B) substitution [108, 109]. Interestingly, it has also been proposed for energy harvesting applications [110, 111] and real-case magnetocaloric refrigerators, that provide increased energy efficiency and substantial environmental benefits compared to gas compression thermodynamic cycles [112–115]. Also, the parent compound Fe_2P [116] exhibits this FOMT with a much larger magnetocrystalline anisotropy (MCA) than FeMnPsi compounds [117], making it rather a candidate material for permanent magnets. Indeed, its Curie temperature ($T_C \approx 220$ K) is too low for most applications. However, T_C can be raised well above room temperature by suitable Si, Ni, or Co alloying while preserving a MCA nearly as large as in the parent compound [118]. It is therefore apparent that pure Fe_2P, though not directly applicable in magnetic or magnetocaloric

[1] The contents of this chapter are already published on Physical Review Materials: Pietro Bonfà, **Muhammad Maikudi Isah**, Benjamin A. Frandsen, Ethan J. Gibson, Ekkes Brück, Ifeanyi John Onuorah, Roberto De Renzi, and Giuseppe Allodi. **Ab initio modeling and experimental investigation of Fe_2P by DFT and spin spectroscopies.** DOI: 10.1103/PhysRevMaterials.5.044411

technology, shares most of its physics with the derived alloys, while it is possibly a simpler system to model theoretically.

Fe_2P has a complex hexagonal C_{22} structure with a space group $P\bar{6}2m$ (no: 189). The primitive unit cell consists of nine atoms, three Fe1 iron atoms in $3f$ sites, three Fe2 atoms in the $3g$ sites, two P1 potassium atoms in the $2c$ sites and one P2 in the $1b$ site [119, 120]. Below $T_C \sim 220$ K, Fe_2P orders ferromagnetically (FM) with magnetic moments directed along the c-axis. This magnetic structure has been widely investigated and an inconsistency on the size of the magnetic moment of Fe1 characterized the first reports [116, 120–125].

All reports qualitatively agreed on a larger Fe2 moment with a localized character, and a reduced Fe1 moment typical of itinerant magnetism (a feature shared by FeMnPSi alloys [126]). However, poor quantitative agreement on the size of the Fe1 magnetic moment characterized early literature and, in addition, the presence of helical states below T_C was discussed [124]. A recent elastic neutron scattering experiment[118] seem to finally settle the value of the two magnetic moments of Fe1 and Fe2 to be 0.8 μ_B and 2.11 μ_B respectively while also showing the presence of sizeable local moments on Fe up to 30 K above the FM transition temperature.

Herein, the motivation of this work is threefold. First, the inconsistencies that can be found in the sparse and often very old literature on Fe_2P, as pointed out above, demand clarification by newer experiments. Second, this study will guide the interpretation of NMR and μSR experiments on Fe_2P-based alloys of interest for applications. Third, our results benchmark and validate *ab initio* investigations of hyperfine couplings that are shown to be extremely useful for experimental data analysis.

5.2 NMR

NMR experiments[2] were carried out with finely powdered Fe_2P samples, in order to maximize the penetration of the radio frequency (rf) magnetic field. Spontaneous and intense ^{31}P signals were recorded in ZF measurements up to $T \sim 150$ K. The ZF spin echo amplitudes at 5 K and 77.3 K, are plotted vs. frequency ν in Fig. 5.1. The double peaked structure observed at low temperature, shown in the inset of Fig. 5.1, was initially attributed to the couple of magnetically inequivalent P sites of this system [129]. This structured peak should instead be associated with the signal arising from two distinct contributions: the one from magnetic domains and the one originating from domain walls (Bloch walls). This is indeed confirmed by the application of a small external field which makes the structured peak evolve into a single broad resonance.

The main panel of Fig. 5.1 shows 4 resonances in total with a single peak in the range 70-75 MHz, and three peaks below 25 MHz. The mean frequencies obtained from a multi-Gaussian phenomenological fit shown in the same figure are 14.8 MHz,

[2]NMR measurements were carried out in the university of Parma's NMR EXA lab by colleagues with a home-built phase-coherent spectrometer [127]. The NMR spectra were recorded by means of a standard $P - \tau - P$ spin echoes pulse sequence, with equal rf pulses P of intensity and duration optimized for maximum signal, and delay τ limited by the dead time of the apparatus. [128].

18.2 MHz, 23.6 MHz and 72.7 MHz. Based on Mössbauer spectroscopy measurements,[116, 130] ^{55}Fe resonances are expected at 16 and 24 MHz. [3] The latter is clearly visible while the former falls under ^{31}P resonance and partially contributes to the double-peaked structure observed experimentally. Based on this interpretation, which is corroborated by first principles estimations discussed below, the hyperfine field at P1 and P2 sites can be estimated in 4.5 T and 0.8 T respectively. From the inset of Fig. 5.1 it is also evident that the hyperfine field at P1 sites has positive sign.

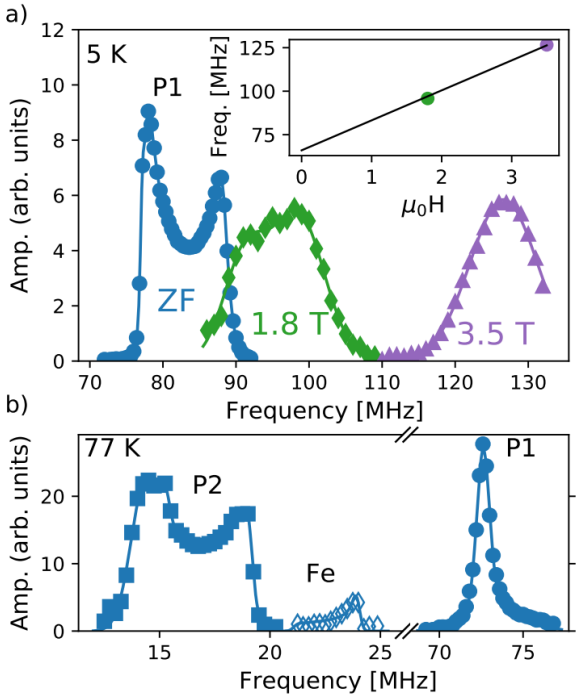

Figure 5.1: a) ^{31}P1 NMR spectra at T = 5 K in ZF (domain wall signal) and in applied fields approaching saturation of the magnetization (domain signal). The inset shows the resonant frequency vs applied field, the black line is a fit described in main text. b) ZF NMR spectrum at T = 77:3 K: ^{31}P2 (left panel, filled squares), ^{57}Fe2 (left panel, empty diamonds) resonance lines and ^{31}P1 resonance (right panel, filled circles). In both panels the lines are a multigaussian phenomenological fit. Portions of the spectra containing just noise are omitted for clarity.

5.3 μSR

The observed zero-field (ZF) μSR measurements[4] are shown in Fig. 5.2. At low temperature, the μSR signal exhibits oscillations characteristic of quasi-static long range magnetic order (LRO) at the muon stopping site. These oscillations comprise a single frequency, which suggests a single magnetically distinct muon stopping site

[3] The estimate is done by extrapolating the results shown in the supplemental materials of Ref. [130] to T=77 K.

[4] μSR measurements were carried out by colleagues at PSI and TRIUMF on a powdered samples of Fe_2P pressed into small pellets that covered the whole muon beam.

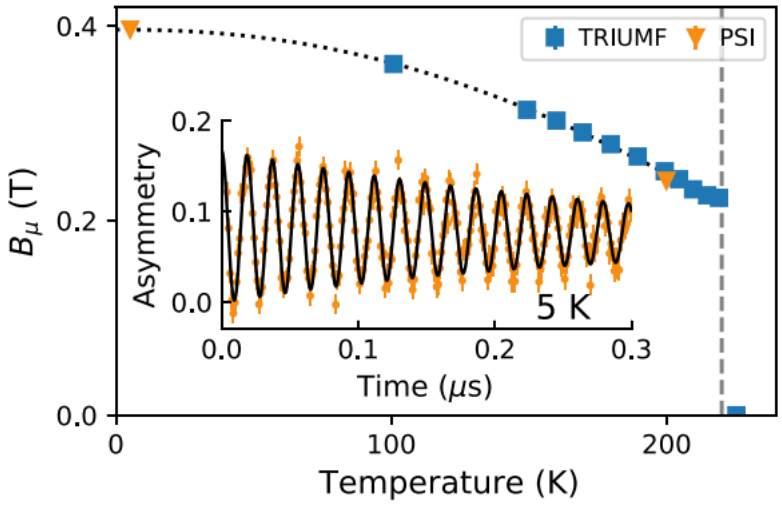

Figure 5.2: The local field at the muon site as a function of temperature extracted from fits to ZF-μSR data collected at TRIUMF (blue squares) and PSI (orange triangles). The vertical dashed line is the Curie temperature (∼220 K) and the dotted line is a guide to the eye. Inset: ZF-μSR data at T = 5 K. Orange dots and the solid black curve represent the experimental data and best fit, respectively. The coherent oscillations indicate the presence of a well-defined, static magnetic field at the muon site due to the long-range FM order.

in the material or, more likely for this system, a single crystallographically distinct site experiencing a range of fields centred on the field corresponding to muon precession frequency. The temperature dependence of muon precession frequency (or local magnetic field, B_μ) confirms a FOMT in the system. Upon heating, the oscillating frequency progressively reduces and is eventually lost at $T_C \sim 220$ K owing to the first order magnetic transition. Still a fast depolarization due to Fe-spin correlations survives up to 50 K above the transition, in agreement with the observation of magnetic moments on Fe atoms above the critical temperature.[130]. To parametrize the oscillations, the first 0.3 μs of the spectra were fitted to a function

$$A_{\mathrm{ZF}}(t) = a_{\mathrm{FM}} \cos(2\pi\nu t + \phi)\mathrm{e}^{-\lambda_{\mathrm{FM}}t} + a_{\mathrm{B}}\mathrm{e}^{-\lambda_{\mathrm{B}}t} \tag{5.1}$$

where A_{ZF} is the muon spin polarization function under ZF. a_{FM}, ν, ϕ and λ_{FM} are the asymmetry, frequency, initial phase, and relaxation rate, respectively, arising from internal field components that are perpendicular to the initial muon spin polarization. a_{B} and λ_{B} are the asymmetry and the relaxation rate arising from the internal field contributions that are parallel to the initial muon spin polarization.

At 5 K, the best-fit frequency is ν = 53.72(1) MHz, corresponding to a magnetic field magnitude of $B_\mu = \nu/\gamma_\mu = 0.3963(1)$ T, where $\gamma_\mu = 135.5$ MHzT^{-1} is the gyromagnetic ratio of the muon.

5.4 Muon-stopping sites and hyperfine couplings at the muon.

In order to characterize the origin of the contributions to the μSR signal, I performed plane wave spin-polarized DFT calculations (implemented in Quantum ESPRESSO package [131–133]) to locate the most probable muon-stopping site and assess the degree of perturbation the muon-probe causes in the system.

I have utilized the generalized gradient approximation (GGA) proposed by Perdew Burke and Ernzerhof (PBE)[134] and Projector Augmented Wave (PAW) [75] pseudopotentials, required to reconstruct the core electrons polarization. The plane-wave cutoff is 80 Ry while that for the charge density is 800 Ry. A $6 \times 6 \times 8$ uniform Monkhorst-pack (MP) [67] was used for the Brillouin zone sampling in the unit cell while for muon interstitial sites calculation I have used a $2a \times 2b \times 3c$ supercell. To describe the magnetism, I have used a Marzari-Vanderbilt [135] smearing of 5 mRy while I chosen a Gaussian smearing of 20 mRy for a supercell calculations.

For all the calculations presented in this chapter, the experimental lattice parameters $a = b = 5.877$ and $c = 3.437$Å [119, 120, 136], have been adopted even though the structure optimisation show very little displacement smaller than $5 \cdot 10^{-2}$ Å. The above computational configuration successfully reproduced the ferromagnetic magnetic (FM) ground state of Fe_2P with the energy difference 1.1 eV per unit cell between the FM and the non-magnetic configuration. The calculated magnetic moment on the Fe1 and Fe2 atoms are 0.84 μ_B and 2.22 μ_B respectively in good agreement with experiment [122, 123, 137, 138].

For muon-stopping site calculations, the set of initial muon locations and the Fe_2P atomic positions were fully relaxed in a $2a \times 2b \times 3c$ supercell until forces and energy difference between optimization steps were smaller than 10^{-3} Ry/a.u and 10^{-4} Ry. A $4 \times 4 \times 4$ Monkhorst-pack mesh grid was used for the supercell and muon contact hyperfine field calculations. The initial guess for the muon calculations are 8 positions from symmetry reduced $4 \times 4 \times 4$ uniform grid sampling and additional 3 positions from the disconnected minima of the bulk electrostatic potential. The full list of initial positions used to perform the calculation and their final relaxed counterparts are presented in Table 5.1.

From Table 5.1 above, ignoring symmetry equivalent relaxed positions, there are five inequivalent candidate muon sites, labeled with letters from A to E in order of increasing total energy, are reported in Table 5.2. The label A* indicates a slightly displaced analogous of site A, with the distance d_{A-A^*} being 0.2 Å. The energy difference between the two is within numerical accuracy, but their distance testifies a rather flat potential energy surface that implies some degree of delocalization of the muon wave function. This has been shown to have limited effects on the local field at the muon site provided that the muon is not diffusing [139].

Table 5.1: Summary of candidate muon stopping sites. The first 8 sites are from $4 \times 4 \times 4$ uniform grid and the last 3 from the bulk electrostatic potential.

	wyckoff[a]	(x,y,z)[b]	(x,y,z)[c]
1	$1a$	0.00 0.00 0.00	0.0000 0.0001 0.0001
2	$3g$	0.00 0.25 0.50	0.0024 0.3274 0.5000
3	$3f$	0.00 0.50 0.00	0.0000 0.5473 0.0074
4	$6i$	0.00 0.50 0.25	0.0002 0.5314 0.1038
5	$3f$	0.00 0.75 0.00	0.0000 0.7068 0.0003
6	$6i$	0.00 0.75 0.25	0.0000 0.7054 0.0160
7	$12l$	0.25 0.50 0.25	0.0578 0.3595 0.4997
8	$6k$	0.25 0.50 0.50	0.0486 0.3535 0.5000
9	$6k$	0.10 0.35 0.50	0.0554 0.3572 0.4999
10	$3f$	0.35 0.35 0.00	0.2959 0.2959 0.0038
11	$2d$	0.33 0.66 0.50	0.3320 0.6654 0.5001

[a] wyckoff number
[b] starting position
[c] final relaxed position

Table 5.2: *Ab initio* muon sites and contact hyperfine fields. The columns are: site label $\alpha = A - E$; fractional coordinates in the conventional unit cell [Fe1 at (0.0,0.257,0.0), $3f$ and Fe2 at (0.0, 0.591, 0.5), $3g$]; total energy difference $\Delta E = E_\alpha - E_A$; contact hyperfine field in Tesla.

Label	Wyckoff	(x,y,z)	$\Delta E(meV)$	B_C (T)
A	$3g$	(0.000, 0.328, 0.500)	0	-0.4274
A*	$6k$	(0.052, 0.358, 0.500)	0	-0.5022
B	$3f$	(0.296, 0.296, 0.000)	280	-0.4573
C	$2d$	(0.333, 0.666, 0.500)	690	-1.7049
D	$3f$	(0.000, 0.545, 0.009)	760	-
E	$1a$	(0.000, 0.000, 0.000)	1120	-

This difference originates from the convergence criteria used for structural relaxation that stop after reaching a flat region of the potential energy surface and leave the muon in a lower symmetry site with $6k$ wyckoff position that is however only ~ 0.2Å away from the $3g$ site. In conclusion, our results indicate that the muon is likely to be trapped in a $3g$ site.

Notably, the positions A and B are just 0.5 Å and 0.3 Å away from the absolute minimum and the second lowest minimum of the electrostatic potential, while site C corresponds exactly to the position of the third relative minimum of the electrostatic potential (see inset in Fig. 5.3). A similar behavior was found in muon site calculations performed on FeCrAs that shares the same space group as Fe_2P[29]. Finally, the largest displacement induced by the muon on the neighboring magnetic atoms is smaller than 0.5 Å.

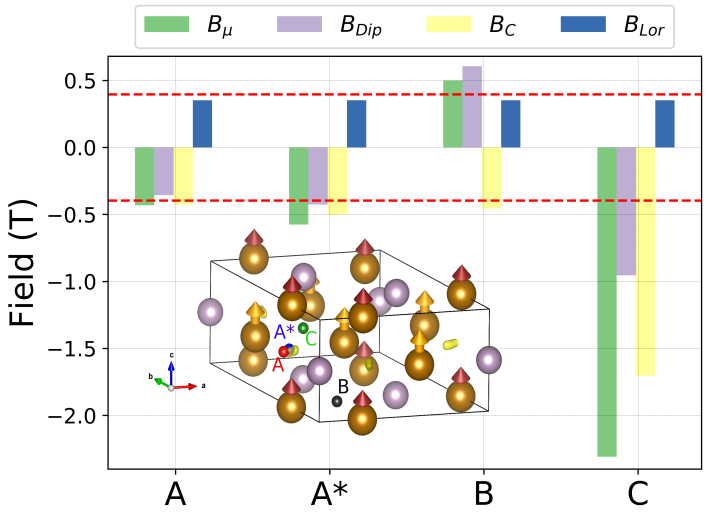

Figure 5.3: Bar plot of the contributions to the local field B_μ (green) at four muon sites (A-C), compared with the experimental value (red dashed lines, sign unknown): dipolar (gray), Lorentz (blue), and contact (yellow). Inset: the Fe_2P unit cell with Fe1, Fe2 magnetic moments as orange and red arrows, respectively. Brown and mauve spheres are Fe, P atoms and the muon sites are labeled A-C. The minima of the unperturbed electrostatic potential, U_{min}, are shown by the yellow isosurfaces at U_{min} + 0.2 eV.

Further, using Eq. (2.24) in Chap. 2, I have calculated the muon contact hyperfine field at the stopping sites, the values of which are reported in Table 5.2 (fourth column). The local fields at the muon sites, shown in Fig. 5.3, are instead in much better quantitative agreement with the experiment. From a quick inspection of the various contributions it is immediately recognized that the long range dipolar contributions (sum of B_{Dip} and B_{Lor}) is almost zero for site A and B, and the local field at the muon sites mainly originates from the Fermi contact term. The comparison with the experimentally measured local field is equally good for both site A and B, with the former showing slightly better agreement. Admittedly, while the highly symmetric site A reproduces the experimental results with better than 10% accuracy, a small displacement bringing the muon to site A* results in a misprediction of the order of 30%. An improved estimate of $\mathbf{B}_{\text{C}}$ could be obtained by taking into account the muon wavefunction delocalization, [139] but this is beyond the scope of the present investigation and probably of limited interest. It is however certain that position A represents an occupied muon site in the sample. A partial occupation of site B be cannot be ruled out and should be considered in future analysis of μSR data of alloys since it is compatible with experimental observations and muon sites branching ratios are not directly proportional to the embedding energy differences.

5.5 Hyperfine couplings at the P nuclei

To further, characterize the NMR signals in the low temperature magnetic phase, a full electron calculation were performed to calculate the hyperfine parameters for P

nuclei. The Wien2k [140] and Elk package [141] package were used for this purpose.

For Elk, in order to achieve convergence of hyperfine fields estimates, a dense k-point grid of $10 \times 10 \times 12$ MP is used while atomic positions were kept fixed in the experimentally reported values. A plane-wave cutoff of $|G+K|_{\max} = 9/R_{\min}^{MT}$ ($R_{\min}^{MT}$ is the average of the muffin-tin radii in the unit cell) was used for the expansion of the wavefunction in the interstitial region. The muffin-tin radius for Fe and P are 1.98 and 2.17 a.u. and respectively. The number of empty states was increased until it reached 40% of valence states and spin-orbit coupling was considered. For Fe, we moved semi-core *s* states to the core and treated them with the full Dirac equation including core polarization. In the Wien2k code, the Dirac equation is solved with the collinear spin formalism and the magnetization is assumed to be directed as the valence magnetization. An equally valid assumption is to consider it to be in the opposite direction. In this case, $12 \times 12 \times 8$ MP was used and muffin-tin radii were 2.35 and 1.83 a.u. for Fe and P respectively.

The approach for the calculation of the hyperfine field for the muon described in Chap. 2 is similar to that for the nuclei both for the long-range dipolar contribution (treated as classical magnetic dipoles) and the short-range Fermi contact contribution except that that for the contact term, the spin density at the P nuclei is actually averaged over the Thompson radius in order to account for relativistic effects [142]. Contrary to hyperfine fields in $3d$ transition metals, where core *s* orbitals give rise to the dominant contributions, the contact field at the P sites dramatically depends on valence electrons' spin polarization and an accurate description of the latter is mandatory. Finally, the short-range dipolar contribution due to *p* orbitals on P atoms is non negligible and contact, short range and long range dipolar terms all appreciably contribute to the final estimate. The results for both Wien2k and Elk calculations are reported in the Table 5.3 below.

Table 5.3: Hyperfine field at the P nuclei in the low temperature ferromagnetic phase obtained with Elk and Wien2K with magnetic moments parallel to the ***c*** lattice vector. All values are in Tesla and are obtained from simulations including spin orbit interaction. The numbers appearing in the brackets are the standard deviation of the two estimates of the contact part obtained with the two different methods implemented in Elk. A positive sign indicates that the spin polarization of a given contribution is the same as that of Fe-*d* orbitals, therefore producing a positive coupling in ferromagnetic Fe_2P, a negative sign means opposite.

Code	Nuc.	B_C	$B_{\text{DipSR}}^{\text{anis}}$	$B_{\text{Dip}}^{\text{anis}}$	$B_{\text{exp}}^{\text{iso}}$	$\sqrt{5/2}B_{\text{exp}}^{\text{anis}}$
Wien2k	P1	3.8	-1.0	+0.11	3.83(4)[a]	0.73(2)[a]
	P2	0.3	0.20	+0.19	0.94(4)[b]	0.28(2)[b]
Elk	P1	4.0/3.2	-0.8	+0.11	3.83(4)[a]	0.73(2)[a]
	P2	0.2/0.7	0.1	-0.19	0.94(4)[b]	0.28(2)[b]

[a] Data from applied field NMR.
[b] Data from ZF NMR

The calculated hyperfine field at P1 and P2 sites shown in Table 5.3 provides

the attribution of the NMR peaks. The contact term accurately reproduces the experimental bulk $B_{hf}^{(iso)}$ for P1 while the comparison for P2 is seemingly less accurate. The field shift of a signal originating from domain wall, like our zero field signal for P2, is of the order of the long range dipolar contribution. In view of the unknown domain wall structure this provides a systematic error in our zero field data analysis, that can also be approximately quantified by comparing the local field obtained from bulk and wall signals for P2, which is 0.9 T. This systematic error has the same magnitude of the uncertainty of the computational estimate, as it is evident from the comparison of the values referring to equivalent quantities appearing in Table 5.3, so that the present analysis of the experimental data is still perfectly adequate for our comparison purpose. In light of this, the small deviation between the predicted and experimental isotropic contribution at P2 is not surprising.

The analysis of the anisotropic part requires more care. In Table 5.3 the experimental $B_{\text{exp}}^{\text{anis}}$, that represents the average of the anisotropic broadening over all directions, is multiplied by $\sqrt{5/2}$ in order to compare it with the anisotropic contributions generated by the short range and long range dipolar interactions described *ab inito*. The experimental values reported for P2 are small and the systematic error due to the lack of domain wall description makes it difficult to draw meaningful comparisons. On the other hand, in applied field, at saturation, B_{Lor} and B_{Demag} cancel out and, as a consequence, for Fe_2P, only B_{DipSR} and B_{Dip} contribute to the anisotropic part. A good quantitative agreement is obtained in this case for P1.

5.6 Conclusions

In summary, I have presented an investigation of the in-field and zero-field magnetic order of Fe_2P using ^{31}P NMR and μSR. A detailed characterization of the microscopic coupling between electrons and P nuclei or the muon in Fe_2P allowed to identify the microscopic origin NMR and μSR resonances in the ferromagnetic phase of this compound.

I have also shown that, DFT based simulations can accurately describe the ground state of Fe_2P with simple GGA functionals and also the microscopic contributions to hyperfine coupling parameters could therefore be obtained straightforwardly for both P nuclei and the muon. In addition, the computational prediction allowed to identify a previously mis-attributed signal from ^{31}P nuclei that can be associate with the $1b$ site, an information to be used in future experiments. This work completely characterizes the signal of two technique of election for the characterization of magnetic properties, thus providing an important base for further analysis of different alloy compositions. Finally, I show that by evaluating the local fields at the muon sites for a candidate magnetic structure, the field experienced by the muon at this site can be compared with the corresponding observed muon precession frequency.

CHAPTER 6

High-throughput design and implementation for muon-site and hyperfine calculations

In this chapter, I describe the high-throughput approach I have developed to automate the calculation protocols and steps of finding the muon-stopping sites and estimating their hyperfine interactions. The HT approach is benchmarked in 16 magnetic compounds, while the limitations and setbacks are also pointed out and discussed.

6.1 Introduction

The protocols for the determination of the muon sites and estimating the hyperfine field from first principle with DFT calculations are well established and have been utilized to successfully investigate the properties of compounds including those of superconducting, magnetic and semiconducting compounds [25, 143]. The comprehensive knowledge of the implantation site and local interactions of the positive spin-polarized muons in the samples are necessary to aid in a wholesome analysis of the experimental μSR spectral data. For example, in the previous chapter (Chap. 5) they allowed to characterize the magnetic ground state of Fe_2P [144]. The calculation protocols utilized for site identification and hyperfine calculations include the following steps; initializing the trial initial guesses of the muon sites, generating the supercell structure, atomic position relaxation of each of these initial guesses in the supercell with DFT, ensuring convergence of the optimization iterations, collecting, analyzing the optimized results and further self-consistent DFT and post processing calculations for hyperfine interaction analysis. But then, carrying out the calculations following these protocols are both resource and task intensive, performed sequentially step after step with a lot of human intervention required to track and coordinate the calculations. Another, the process of tracking the calculation history and the changes within these steps are performed manually. Hence, to use these calculation protocols expertise in the method is required as they are not user friendly for a regular user.

However, with the advent and success of the DFT-based *high-throughput* (HT) approach together with available databases for the storage of electronic structure properties [145–154], the way in which large calculations and "human" DFT calculation are performed is fast changing. The automated frameworks and database in the HT approach have opened the possibility to *automatically* run, manage and analyze large number of calculations over long periods of time. For DFT based HT approaches, there already exist a number of automation and management integrated platforms such as AiiDA (Automated Interactive Infrastructure and Database for Computational Science) [155, 156] and also electronic structure databases such as the Bilbao crystallographic server [157–160] and Materials Project [161].

The intent of this chapter is to present the developed automated workflow for muon calculation protocols to aid in μSR data analysis. This HT approach is then demonstrated and applied to search and identify the muon implantation sites and calculate hyperfine interactions in a set of 16 magnetic compounds[1]. The workflow is embedded on the existing integrated AiiDA platform to produce calculations based on DFT while making using of the Bilbao database to access the input structures. The HT approach and automation is of particular importance and interest for muon calculations to ameliorate the tedious manual tasks in running, managing and storing calculation data and also encouraging the reproducibility of calculation results. HT approaches are proven to be very successful for a wide range of purposes in material design and discovery [162], but the still face important challenges in the case of magnetic materials [163, 164] which are of particular interest in this work. These challenges constitute part of the final discussion.

The main aim in the development of the workflow is not exclusively that of improving accuracy, but rather to find the compromise that ensures automation and timely computations while producing sufficiently reliable results. We have omitted modelling the muon charge states, as this will double the computational effort required and also only sparsely sampled initial muon positions have been considered. The results of the workflow benchmark however, indicate that these factors not considered are relevant to achieve reliable results. These then constitute further improvements to be implemented in the later versions of the workflow, as limitations due time and computational resources hinder their implementation and benchmark at this time.

The chapter is organized as follows; first I discuss the database and selection criteria for the compounds invesitgated in this study, followed by the methodology which contains description of the AiiDA platform and the developed workflow. Then, I proceed to show the application and benchmark of the workflow in the selected magnetic compounds. The results allow us to identify and discuss the success as well as the limitations of the HT workflow (at its current stage), while providing insights for further work, particularly that of extending the workflow to accommodate the approaches of improving the treatment of magnetism within DFT.

[1] The reported workflow at its current state was developed, tested and improved in a step after step process, hence some of the reported benchmark results on the 16 magnetic compounds are not all entirely reproduced with the latest reported version of the workflow.

6.2 Material overview: Database and selection criteria

Here, I discuss the range of materials applicable for HT calculations in this work considering that the aim is to search and identify stopping positions for muon treated as a hydrogen impurity together with their hyperfine interactions towards aiding the μSR experimental analysis. DFT calculations have been used to study the muon in a wide range of materials, including in superconducting and magnetic compounds [23, 26–33]. But then, for this work we consider only magnetic systems where the muon hyperfine interactions (often calculated by DFT) play important roles.

At this point, I discuss the database where the input structures needed to initialize the calculations within the workflow are taken from and the selection criteria for the materials considered in this study.

6.2.1 Database: Crystal and magnetic structures

The input crystal structures and magnetic order are accessed from the `MAGNDATA` [159, 160] database of the Bilbao crystallographic server [157, 158]. Each of these crystal and magnetic structures are stored in the magnetic crystallographic information file (`magCIF` or `mcif`) where crystal space groups, magnetic symmetry and magnetic space groups are used to describe the atomic positions and magnetic order. This database is open access and reported to contain thousands of experimentally known magnetic structures. However, for the purpose of this work, I restrict the search and selection of magnetic structures from this database considering the following criteria;

- Only magnetic structures where experimental μSR results are available are considered. This is necessary to provide a means to benchmark the workflow results. We expect to lift this criteria once the workflows are successful benchmarked and certified to produce desired results.
- Only collinear commensurate or incommensurate magnetic structures (limited to single wavevector structures) are considered, to avoid complex magnetic orderings which often result to magnetic frustrations, or huge exchange interactions eg. disordered systems, spin glasses, etc. This is because it is well-known that most of these compounds with 'complex' magnetism are problematic for the conventional DFT [62, 63] and are also one of the major challenges faced in DFT-based HT computations [163–166]. Even though, this problem has been widely tackled with beyond DFT approaches but their implementation in HT automation is quite far from trivial as they are mostly parameter dependent on a case by case basis. Only simple magnetic orders are considered.
- Only the ground state (low-energy) magnetic structures at T=0 K are considered since, DFT is a ground state theory.
- Structures with partial occupation of the atoms were also not considered.

- Structures where Lanthanides and Actinides are the magnetic specie were avoided, as the treatment of strongly localized f-electrons pose problems for conventional DFT and in most case the inclusion of spin-orbit coupling (SOC) is necessary which is not considered at the current stage of this workflow.

The crystal and magnetic structure of the 16 selected magnetic structures that satisfy the above criteria are listed and plotted in Fig. 6.1.

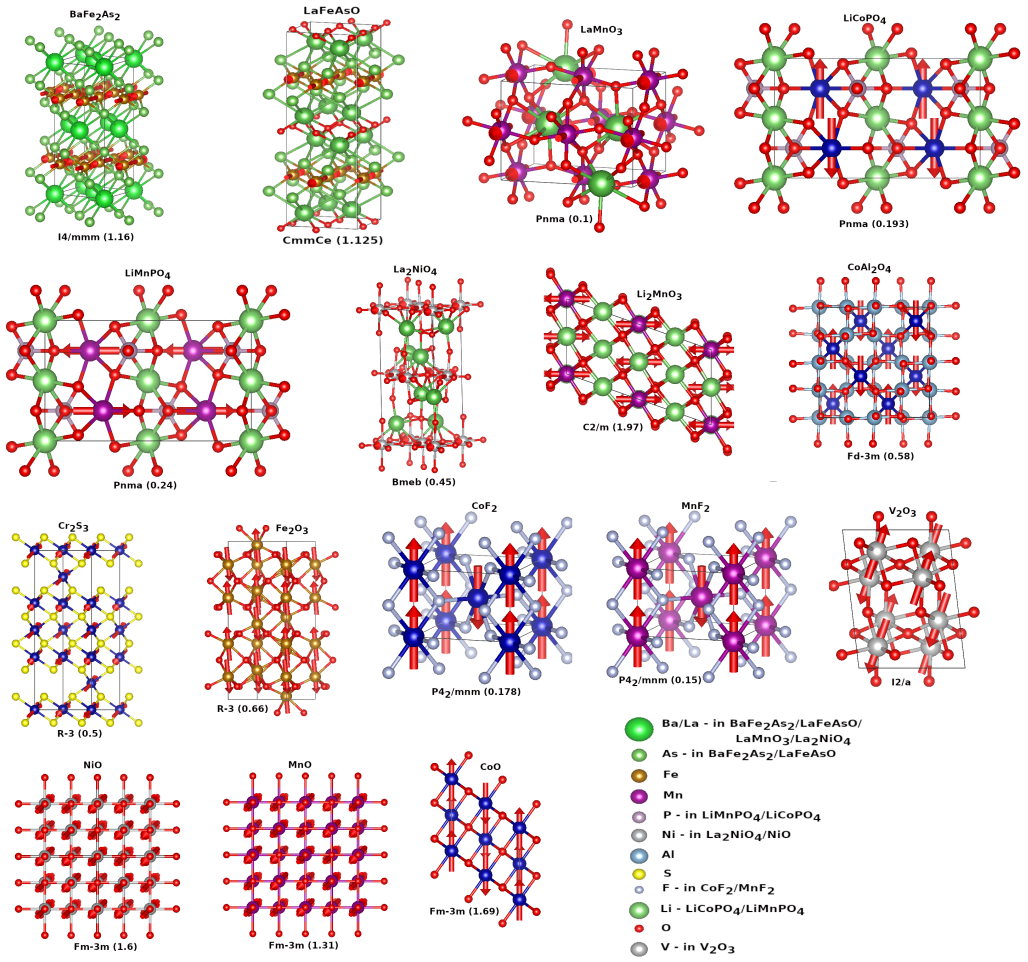

Figure 6.1: Magnetic structures and its representative spacegroup and index from MAGNDATA database.

6.3 Methodology

In this section I describe the details of the DFT calculations and as well describe the workflow based on DFT for the identification of muon sites and hyperfine parameters calculation.

6.3.1 DFT Computational Parameters

The workflow described later in this section is fully based on DFT. For all calculations, spin-polarized plane-wave DFT as implemented in Quantum ESPRESSO [131–

133] restricted only to the collinear formalism was used. I have used the Perdew-Burke-Ernzerhof GGA [65] for the exchange correlation functional and the GBRV high-throughput ultrasoft pseudopotential library [167]. For all structural optimization a plane-wave and charge density cutoffs of 60 Ry and 600 Ry were used respectively. These values were increased by a factor of 1.1 for a single self-consistent run for the muon hyperfine interaction calculations. The Gaussian smearing [168] with width of 0.05 Ry was used for all calculations. A $n_a \times n_b \times n_c$ Monkhost-Pack grid [169] was used for the Brioullion zone sampling, such that the number of grid points along each direction n_i is dependent on the respective crystal coordinate. For this, a minimum grid spacing of $\rho_k = 0.2$ Å^{-1} was used with $n_i = \lceil |\mathbf{b}_i|/\rho_k \rceil$[2],where $\mathbf{b}_i$ represents the crystal coordinates in the reciprocal axes. The magnitude of the starting magnetization (to break the magnetic symmetry) was chosen by scaling the magnitude of the magnetic moment by a factor of 1/3 if the magnetic specie is from the p block and factor of 1/5 if from the d block.

To search and identify the muon stopping sites we use the supercell method already described in Sec. 3.8 of Chap. 3, thus the workflow is based on this approach. This approach requires the generation of the initial positions for the muon using uniform grid positions that are further reduced considering the crystal symmetry. For the muon search calculations, the initial muon position was generated using a $4 \times 4 \times 4$ grid where the grid dimension is increased by 1 if the generated symmetry reduced position is less than 4. For the treatment of the muon, we have considered only the charge neutral impurity case. Another, is the choice of the supercell size to treat the muon *impurity*. Here, the supercell is created starting from the magnetic unitcell and the size is chosen such that nearly cubic supercell structures are achieved with a further limitation on the minimum and maximum number of atoms allowed (set to 60 and 200 respectively)[3]. Typical sizes of the supercell used are $2 \times 2 \times 2$, $2 \times 2 \times 1$ or $2 \times 2 \times 3$ of the magnetic unitcell size. For geometry optimization and relaxations to find the minimum energy positions, total forces and energies were optimized till a threshold of 10^{-3} a.u and 10^{-4} Ry respectively.

6.3.2 Workflows and automation strategy within AiiDA

Here, I describe the workflow for the muon calculations. The workflow is written in python, designed and implemented to function under the AiiDA integrated platform. AiiDA is a python infrastructure designed to enable automation, manage and track calculation data, and supports the usage of external DFT codes via plugins [155, 156]. In addition, it allows one to create and implement workflows including those linked to multiple computers. Other advantages with Aiida is that it is open source, has a number of inbuilt standard workflows and functions that facilitate the implementation of the algorithm for muon calculations. In all, it is python based allowing us to make use of python libraries like `pymatgen`, `ASE`, `spglib` and `MUESR` etc. in the workflow. For tracking and managing calculations, the `PostgreSQL` database backend supported in AiiDA was used. It is important to note that special care has

[2]Where the notation $\lceil |\mathbf{b}_i|/\rho_k \rceil$ is define as the mathematical ceiling function of $|\mathbf{b}_i|/\rho_k$

[3]Exception; This condition was not adopted for the supercell size used in calculations for MnO, NiO and $CoAl_2O_4$ because the calculations were already carried out prior to introducing this condition in the workflow.

been taken to design the workflow in a modular way with functional building blocks, which allows to re-use some existing standard AiiDA workflows for other purposes e.g. querying calculations. The workflow python scripts are available on github website and the calculation data are stored in nodes at local drive hosted on the UNIPR HPC cluster [4].

I now describe the workflow for the HT muon calculations. The graphical representation of the workflow is presented in Fig.6.2. The workflow is initialized by extracting both the crystal and magnetic order symmetry from a magnetic *cif* file (`.mcif`) accessed from the `MAGNDATA` database. The obtained crystal structure is then used to identify the atomic species and further select the pseudopotential files. The crystal symmetry is used to generate the initial guess positions for the muon search. Also, using the crystal symmetry, the supercell size for the calculation is determined and the supercell structure is then generated.

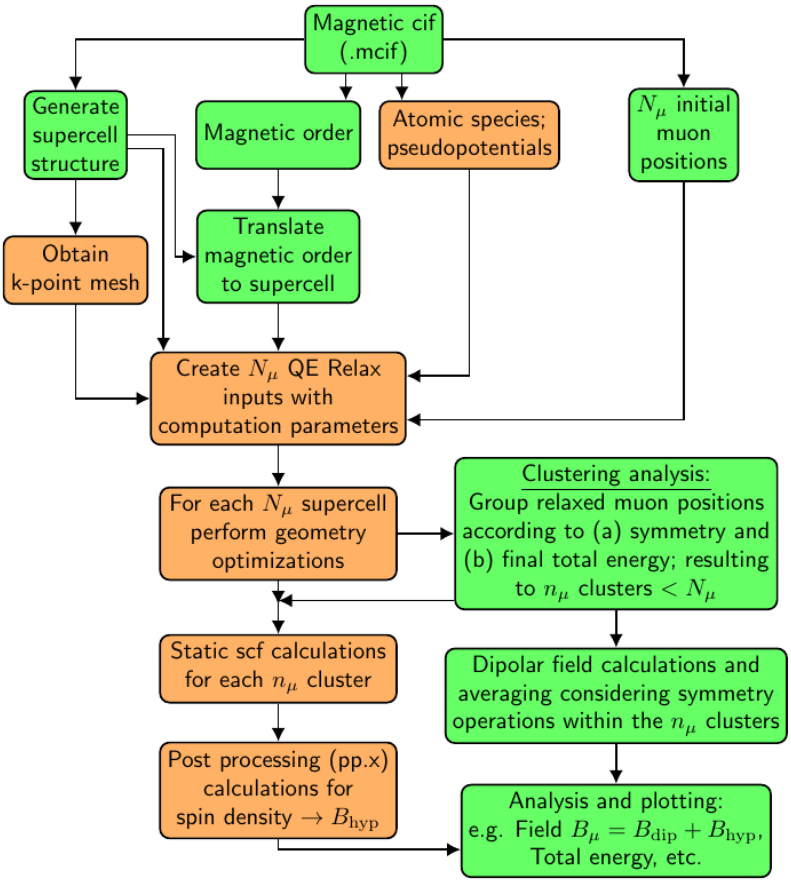

Figure 6.2: Graphical representation of the muon calculation protocol workflow implemented in AiiDA. The boxes in orange color represent calculations where the results are stored as nodes in the database and can be always queried, the boxes in green are of those not stored.

Next, the magnetic order is translated with the new atomic positions in the supercell. After which, the DFT relaxation input files are generated for each of the N_μ initial guess muon positions (details of the other input parameters are described

[4] The data is available on request.

above in Sec. 6.3.1). The next step is to proceed with the DFT geometry optimization or relaxation. These calculations are run in parallel and managed with the AiiDA `JobCalculation` function and `scheduler` classes. With the data provenance that is provided by AiiDA and the implementation in the workflow, calculations were tracked for crashes and restarted for jobs that are not converged.

At the end of the relaxation, to analyze the possible candidate implantation site(s), the N_μ relaxed muon positions are clustered considering symmetry equivalence of these sites and same relaxed total DFT energies. In the *clustering* algorithm, relaxed sites that are equivalent within a symmetry tolerance of 0.05 Å, distance tolerance of 0.01 Å and same total DFT energies within 0.05 eV are considered similar site(s) and subsequently grouped within one cluster. At this juncture, it is important to point out that sites within same cluster though are of same crystal symmetry, might have different magnetic environment which influences the spin density at the muon and in turn the muon hyperfine field. After clustering there are n_μ clusters of candidate sites where $n_\mu < N_\mu$. The total DFT energy differences within each cluster is an important quantity for the identification of the muon implantation site(s), clusters with relative energy difference above 0.6 eV (typical muon zero point vibration energy [139]) are usually not considered probable sites for the muon.

The next step in the workflow is to compute the contact hyperfine interaction for candidate representative site(s) of each cluster. Within each cluster, representative site(s) for further calculation is chosen such that site(s) with distinct magnetic environment (magnetic symmetry) has a candidate representative. Thus, if each cluster has one representative site, it entails that all the site(s) within the cluster have same magnetic environment. Further, a one-shot self-consistent DFT calculation and post-processing (to obtain the spin density at the muon) are performed for each representative muon site in the cluster, with the atomic positions shifted such that the muon position is at the origin. The shift is necessary to accommodate accurate estimation of the spin density at the muon (muon hyperfine quantity see Sec. 2.5) considering the possibility that none of the FFT grids might be centered at the muon position [26].

The dipolar contribution is then computed using the `MUESR` python library and adopting the *experimental* magnetic moment instead of the one from DFT calculations. In order, to compute the total muon local field, an average of the summation of the contact and dipolar field for the sites of same magnetic environment within the cluster is performed. Then, the results are printed and plotted for each magnetic sample, as shown and used for discussions in the next section.

At this point, it is important to point out that the data contained in the AiiDA provenance and subsequently stored in the database are only inputs and outputs of DFT calculations, these steps are also represented in the workflow diagram in Fig. 6.2 with orange colored boxes. But then with the querying tool and the assignment of PK (primary key) and UUID (universally unique identifier) to data in AiiDA, these analysis can always be recovered with the classes and functions implemented in the workflow.

6.4 Application and case studies

In this section, I present the results obtained from using the muon calculation workflow for the 16 magnetic samples considered in a case by case study. For each of the

magnetic samples used for the benchmark of our workflow, their properties including space group, magnetic order, experimental (μ_{exp}) and calculated magnetic moments (μ_{DFT}) are summarized in Table 6.1. The query tool available in AiiDA was used to obtain both the input magnetic moment from the magnetic cif file and calculated magnetic moment from DFT calculations. Also in Table 6.1 the μSR experimental observed muon local fields B_μ is shown, if only one field is reported, it implies that only one distinct muon site is revealed by experiment, hence two and three fields mean that there are two and three distinct sites respectively. These observed local fields at the muon constitute experimental information that we will use to benchmark our workflow. Thus, with the workflow we intend to find the muon sites and hyperfine field that characterize the experimental results.

Table 6.1: Summary of the relevant properties of the considered magnetic compounds

Stoichiometry	Magnetic species	Space group	Magnetic ordering	μ_{EXP} (μ_B)	μ_{DFT} (μ_B)	$B^i_\mu = \frac{2\pi\nu^i_\mu}{\gamma_\mu}$ (T = 0K) (Tesla)
$LaFeAsO$	Fe	$CmmCe$	AFM	0.63 [170]	2.13	$B^1_\mu = 0.0221$, $B^2_\mu = 0.2066$ [171]
$BaFe_2As_2$	Fe	$I4/mmm$	AFM	0.87 [172–176]	2.10	$B^1_\mu = 0.0516$, $B^2_\mu = 0.2095$ [177–179]
La_2NiO_4	Ni	$Bmeb$	AFM	1.6 [180]	1.24	$B^1_\mu = 0.0148$, $B^2_\mu = 0.2656$ [181, 182]
$LiMnPO_4$	Mn	$Pnma$	AFM	3.9 [183, 184]	4.13	$B^1_\mu = 0.5165$, $B^2_\mu = 0.5902$ [185, 186]
$LiCoPO_4$	Co	$Pnma$	AFM	1.0 [183]	2.47	$B^1_\mu = 0.3040$, $B^2_\mu = 0.3541$ [185, 186]
$LaMnO_3$	Mn	$Pnma$	AFM	3.87 [187]	3.10	$B^1_\mu = 0.6264$, $B^2_\mu = 0.9503$ [188, 189]
Li_2MnO_3	Mn	$C2/m$	AFM	2.35 [190]	2.39	$B^1_\mu = 0.1756$, $B^2_\mu = 0.3232$ [191]
CoF_2	Co	$P4_2/mnm$	AFM	2.60 [192]	2.51	$B^1_\mu = 0.2287$ [193, 194]
MnF_2	Mn	$P4_2/mnm$	AFM	4.60 [195]	4.15	$B^1_\mu = 1.1200$, $B^2_\mu = 9.4973$ [196]
$CoAl_2O_4$	Co	$Fd\bar{3}m$	AFM	1.9 [197]	2.34	$B^1_\mu = 0.1070$ [198]
MnO	Mn	$Fm\bar{3}m$	AFM	5.66 [199]	4.07	$B^1_\mu = 1.1436$ [200, 201]
NiO	Ni	$Fm\bar{3}m$	AFM	2.45 [202]	1.33	$B^1_\mu = 0.4523$ [203]
CoO	Co	$Fm\bar{3}m$	AFM	3.98 [204]	2.38	$B^1_\mu = 0.3977$, $B^2_\mu = 0.5784$, $B^3_\mu = 1.1067$ [203]
V_2O_3	V	$I2/a$	AFM	1.15 [205]	1.21	$B^1_\mu = 0.1107$ [200]
Fe_2O_3	Fe	$R\bar{3}$	AFM	4.22 [206]	3.39	$B^1_\mu = 1.5420$, $B^2_\mu = 1.6379$, $B^3_\mu = 1.6600$ [207–209]
Cr_2S_3	Cr	$R\bar{3}$	AFM	1.199 [210, 211]	2.50	$B^1_\mu = 0.2376$, $B^2_\mu = 0.2877$ [212]

For each of the magnetic samples, the plot printed at the end of the workflow is shown. To read them consider the common legend contained in Table 6.2. For example in Fig. 6.3, the results for LaFeAsO is shown. For each of these plots, the horizontal axis represents the muon cluster $n_{\mu ij}$, where i is the cluster index and j to distinguish different magnetic environment within each cluster. On the vertical axis to the left is the muon local field in Tesla (for the bar plots) and to the right is energy in eV (for the *red* dots). The dashed horizontal line(s) running through the

plots indicates the experimental muon local field (in Tesla) to the left vertical axis. To analyze these plots one has to consider that candidate sites (clusters) with relative total energy above 0.6 eV are not probable sites for the implantation of the muon considering that the zero point vibration of the muon of this order, hence only *low* energy sites are considered possible implantation sites.

Table 6.2: Explanation of the symbols and axes in the workflow result (Figs. 6.3-6.14)

x-axis	Muon site clusters, the first number identifies crystallographically equivalent sites, i.e. the cluster, the letter identifies magnetically inequivalent sites in the same cluster.
y-axis (left)	Calculated local magnetic field (height of the bar graph).
y-axis (right)	Calculated total energy difference to the lowest one (cluster 1, by definition).
Horizontal lines	Experimental local fields: when more than one, color lines are used to different fields in order of black, yellow, cyan etc. to distinguish fields in order of decreasing asymmetry

6.4.1 LaFeAsO

LaFeAsO crystallizes in the Cmme (no. 67) parent space group and has an antiferromagnetic order where Fe is the magnetic specie [170]. The μSR measurement reports two local field (see Table 6.1) for the muon at zero pressure [86]. In benchmarking the results of our workflow, we aim to determine the muon sites that characterize these local fields. Within the workflow, calculations were performed for a $2 \times 2 \times 1$ supercell. The workflow result is plotted in Fig.6.3 and shows that three distinct sites (cluster) were found. For cluster site 3, there are two distinct magnetic environment, even though the two sites are symmetrically equivalent and have same energy. However, the these sites (3a and 3b) are ruled out as not probable for the muon to stop as they have energy above 0.6 eV. The probable sites are site 1 and site 2. The local fields at these sites account for the low and high experimentally determined field (dashed horizontal lines) respectively. In this compound, our workflow predicts the muon sites and assigns the local field at the muon site within the calculation accuracy.

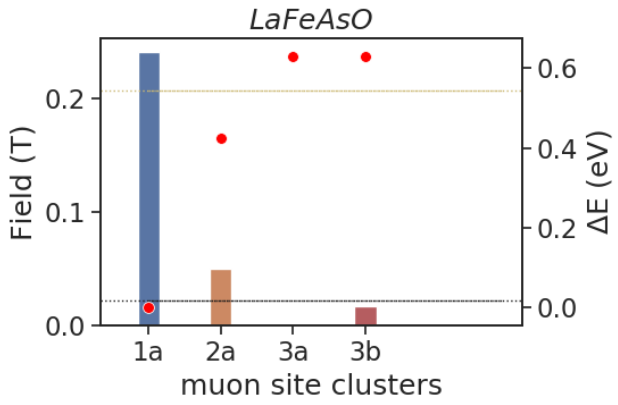

Figure 6.3: Workflow results for LaFeAsO, see Table 6.2 for details of symbol description.

6.4.2 $BaFe_2As_2$

$BaFe_2As_2$ is of the parent space group I4/mmm (no. 139) and has AFM order where Fe is the magnetic specie [172]. Two muon precession frequncies were observed at 0 K [177–179, 213]. A $1 \times 2 \times 2$ supercell was utilized for calculations within the workflow. The workflow results are plotted in Fig.6.4. Site 3 is not considered as it is a high energy site above 0.6 eV. However, site 1 and site 2 are the candidate sites and they both account for the experimental high and low fields respectively at the muon. Also, in this compound the workflow provides excellent prediction of the muon sites and fields.

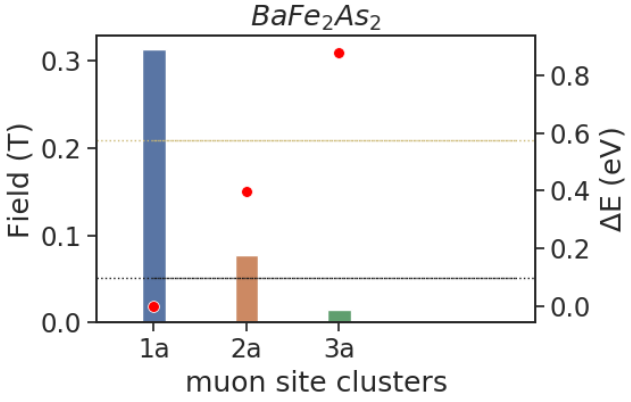

Figure 6.4: Workflow results for $BaFe_2As_2$, see Table 6.2 for details of symbol description.

6.4.3 La_2NiO_4

La_2NiO_4 crystallizes in the Bmeb (no. 64) space group and is an antiferromagnet where Ni is the magnetic specie. [180]. A $2 \times 2 \times 1$ supercell was used for calculations within the workflow and the results are plotted in Fig. 6.5. Here the workflow

results in two sites (clusters) below 0.6 eV, whose local field account for the experimental observed field [10, 181]. In this compound our workflow is successful and provides clear explanation of experimental results.

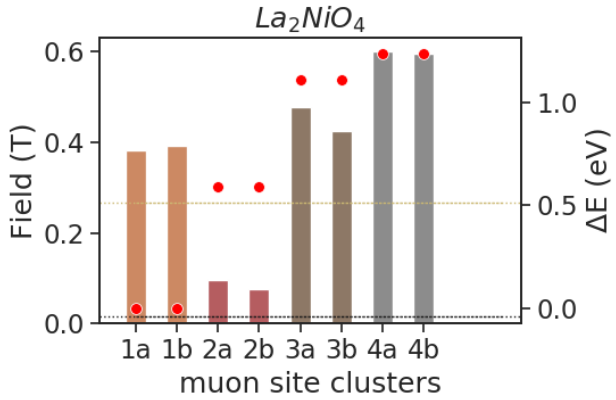

Figure 6.5: Workflow results for La_2NiO_4, see Table 6.2 for details of symbol description.

6.4.4 Li*M*PO_4, (*M* = Co^{2+}, Mn^{2+})

$LiCoPO_4$ and $LiMnPO_4$ crystallize in the orthorhombic crystal structure with the *Pnma* (no. 62) space group. They are AFM insulators [183, 214] and exhibit large magnetocaloric effects [215, 216]. Workflow calculations were performed for a $1 \times 2 \times 2$ supercell in both compounds.

For $LiMnPO_4$, the results are plotted in Fig. 6.6a. Experiment indicates that there are two distinct sites with two local field [185, 186] (see Table 6.1). In this case, even though our workflow results give three distinct sites (clusters) with energies less than 0.6 eV, the calculated muon local field at these muon site(s) are clearly and largely over-estimated in comparison with experiment. This is a case, where the workflow predicts correctly the muon site(s) but fails badly to account for the local field at the muon.

For $LiCoPO_4$, the results are plotted in Fig. 6.6b. Here also, experiment reveals that there are two distinct sites [185, 186]. Our workflow provides four candidate cluster sites, where within each cluster, two distinct magnetic environment exist. The calculated local field of the two lowest energy sites are in agreement with experiment. In this case, the workflow is fairy successful for the muon site calculation.

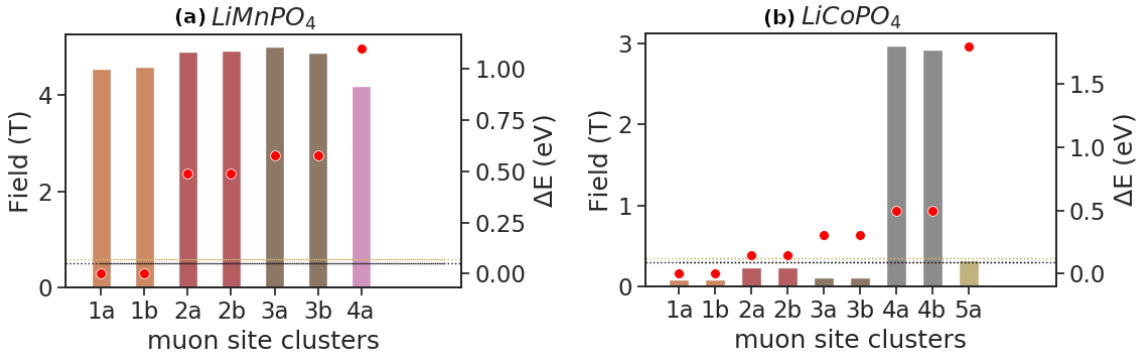

Figure 6.6: Workflow results for (a) $LiMnPO_4$ and (b) $LiCoPO_4$, see Table 6.2 for details of symbol description.

6.4.5 $LaMnO_3$

$LaMnO_3$ crystallizes in Pnma (no. 62) space group. It is an antiferromagnet where Mn is the magnetic specie. [187]. A $2 \times 2 \times 2$ supercell was used for calculations in workflow. The results are plotted in Fig. 6.7. Here experiment [189, 217] reveals two distinct sites. The results of our workflow also predicts two distinct cluster sites with energy less than 0.6 eV. However, the calculated field at both sites are clearly underestimated in comparison with experiment. This is another case like $LiMnPO_4$, where the workflow predicts correctly the muon localization sites but fail to reproduce the local fields.

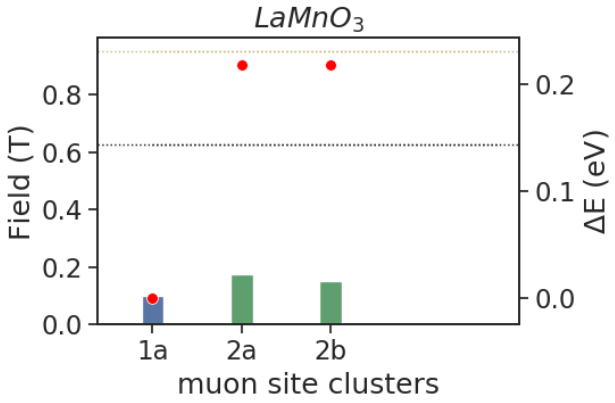

Figure 6.7: Workflow results for $LaMnO_3$, see Table 6.2 for details of symbol description.

6.4.6 Li_2MnO_3

Li_2MnO_3 crystallizes in the monoclinic crystal structure of the C2/m (no. 12) space group. It is an antiferromagnetic insulator [190]. A $2 \times 2 \times 1$ supercell was used for calculations within the workflow and the results are plotted in Fig. 6.8. Here,

experiment reveals two distinct sites with local field 0.3232 T and 0.1756 T at T=0 K [191]. The results of our workflow provide three low energy sites with a slight overestimation of the calculated local field.

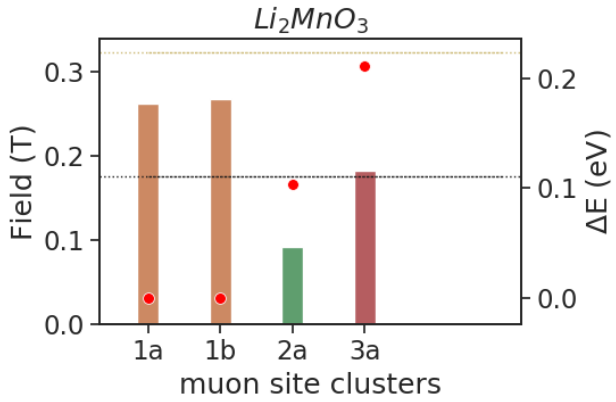

Figure 6.8: Workflow results for Li_2MnO_3, see Table 6.2 for details of symbol description.

6.4.7 MF_2 (M=Co, Mn)

Both CoF_2 and MnF_2 crystallize in the P42/mnm (no. 136) space group and are antiferomagnets [192, 218] where Co and Mn are the magnetic specie respectively. For both structures, a $2 \times 2 \times 3$ supercell was used for the muon site calculations. The candidate sites and their respective total field from the workflow are plotted in Fig. 6.9a and Fig. 6.9b.

For CoF_2, experiment reveals only one distinct site with muon local field of 0.2288 T [193]. The result of our workflow predicts two candidate muon sites whose calculated local field are in agreement with experiment. The workflow provides a decent description of the muon sites and field in this sample.

For MnF_2, experiment reveals two distinct muon sites with low and high local field at 1.12 T and 9.50 T [196], but then with the workflow, three low energy sites were found, and only the low energy local field was reproduced with the workflow. None of the local field at predicted sites accounts for the high field found from experiment.

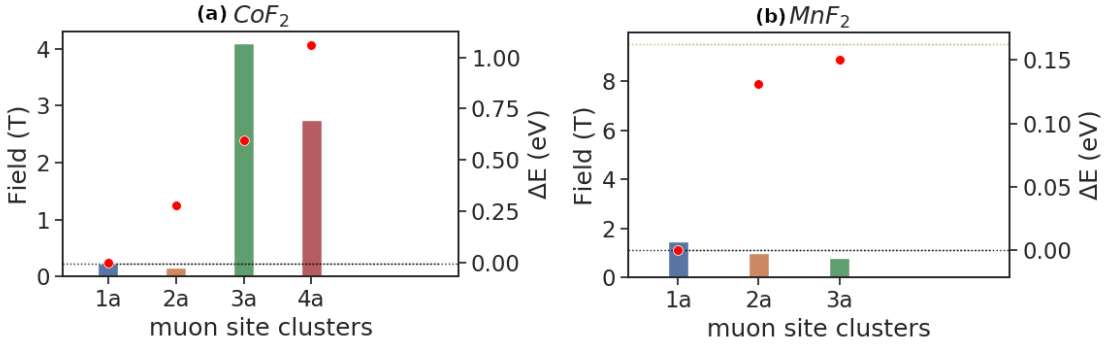

Figure 6.9: Workflow results for (a) CoF_2 and (b) MnF_2, see Table 6.2 for details of symbol description.

6.4.8 $CoAl_2O_4$

$CoAl_2O_4$ crystallizes in the Fd-3m (no. 227) space group. It is antiferromagnetic where Co is the magnetic specie [197]. Structural relaxations were carried out in a $2 \times 1 \times 1$ supercell. The workflow results are plotted in Fig. 6.10. The μSR experiment indicates that there is only one site with local field of 0.1070 T [198]. However our workflow predicts two (cluster) sites. The calculated local field at the lowest energy site is in fair agreement with experiment.

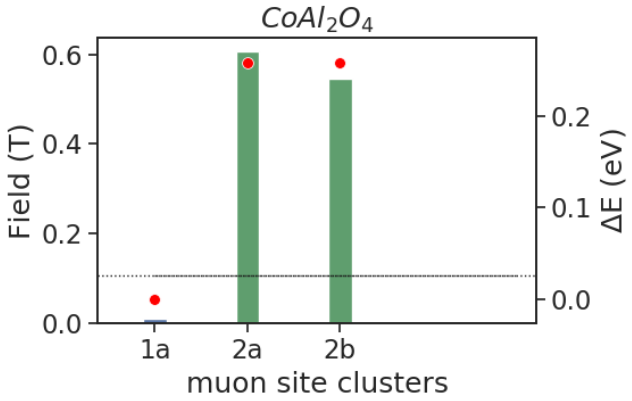

Figure 6.10: Workflow results for $CoAl_2O_4$, see Table 6.2 for details of symbol description.

6.4.9 *M*O (*M*=Mn,Ni,Co)

MnO, NiO and CoO have the rock-salt structure and crystallize in the Fm-3m (no. 225) space group. They are antiferromagnets (type-II) characterized by the propagation vector $\mathbf{k} = \left[\frac{1}{2}, \frac{1}{2}, \frac{1}{2}\right]$ [199, 202, 204]. The magnetic structure consists of (111) sheets of magnetic atoms in which the spins are parallel, but the spin direction alternate in the adjacent sheet. For both MnO and NiO a $2 \times 1 \times 1$ supercell was used for

structural relaxations within the workflow, as the magnetic unitcells are large enough and contain 64 atoms. The workflow results are plotted in Fig. 6.11a and Fig. 6.11b.

For MnO, μSR experiment reveals only one muon site with local field of 1.1436 T [200, 201]. The workflow results predicts four distinct symmetry inequivalent muon sites with nearly degenerate energy. Also the local field at these sites are not in agreement with that from experiment. This is an example where the workflow fails in assigning both the muon sites and the local field.

For NiO, even though the workflow provides a single muon site in agreement with experiment but then the muon local field is highly underestimated.

For CoO, structural relaxations were performed for a $2 \times 3 \times 2$ supercell (of a 8-atom 'primitive' magnetic unitcell). The workflow results are plotted in (Fig. 6.11c). μSR experiment reveals three distinct muon sites [203] and also the workflow results predict three low energy candidate sites. The calculated hyperfine fields at these predicted candidate sites are in decent agreement with experiment.

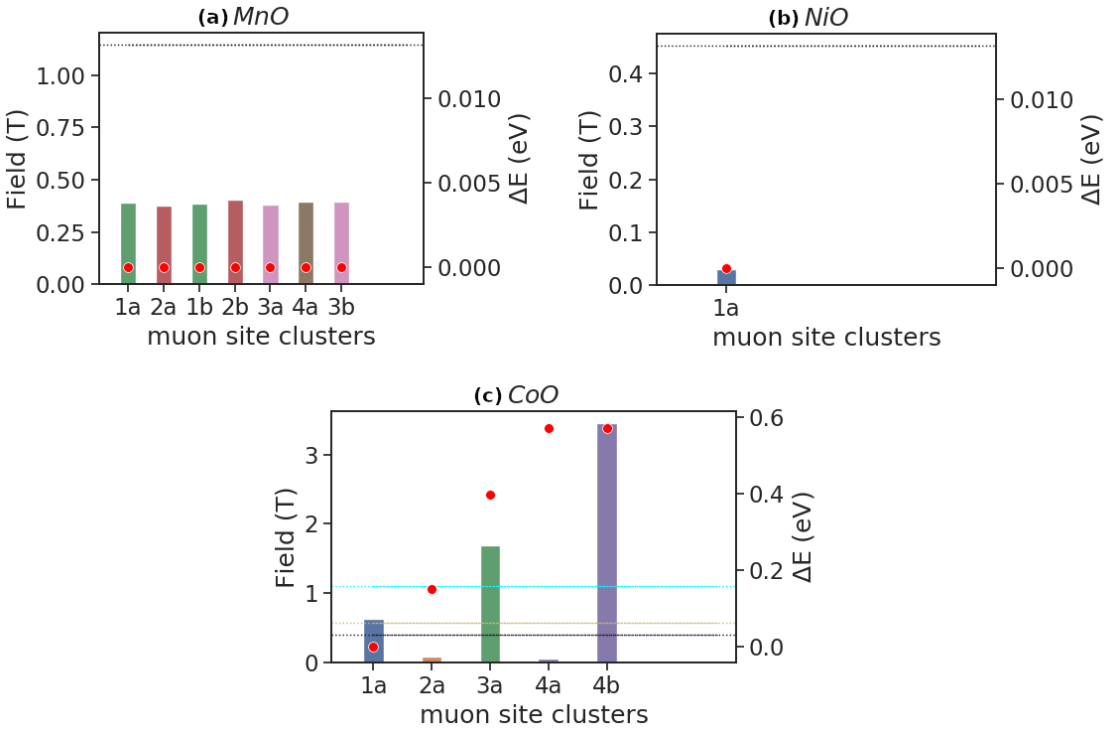

Figure 6.11: Workflow results for (a) MnO, (b) NiO and (c) CoO, see Table 6.2 for details of symbol description.

6.4.10 V_2O_3

V_2O_3 crystallizes in the I2/a (no. 15) space group and orders antiferromagnetically and the magnetic specie is Vanadium [205]. Structural relaxations were performed with the $2 \times 2 \times 2$ supercell and the results of the workflow are plotted in Fig. 6.12. Only one distinct site with 0.1107 T is revealed from μSR experiment [200, 217] but

our workflow provides two low energy sites of which the local field on both sites are in agreement with experiment.

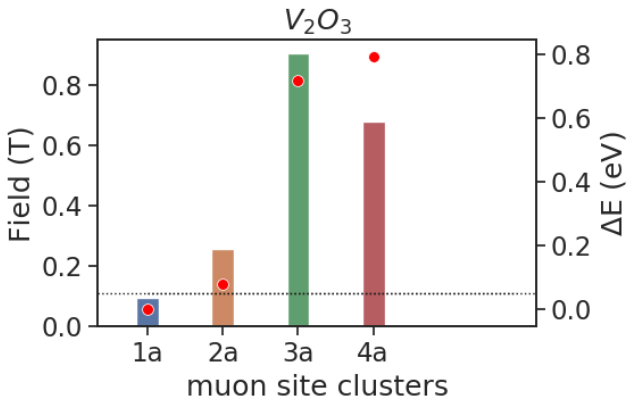

Figure 6.12: Workflow results for V_2O_3, see Table 6.2 for details of symbol description.

6.4.11 Fe_2O_3

Hematite (α-Fe_2O_3) is a semiconductor and crystallizes in the R-3c (no. 167) space group. It orders antiferromagnetically below the Morin temperature with spins aligning along the [111] ([003] in the hexagonal cell) direction (with a tilt of 5-15° [206, 219–221]). Structural relaxations within the workflow were performed with a $2 \times 2 \times 1$ supercell and the workflow results are plotted in Fig. 6.13. μSR experiment reveals three local fields [207–209] but then our workflow reveals only two candidate sites and only one of the experimental local fields is accounted for from the calculations.

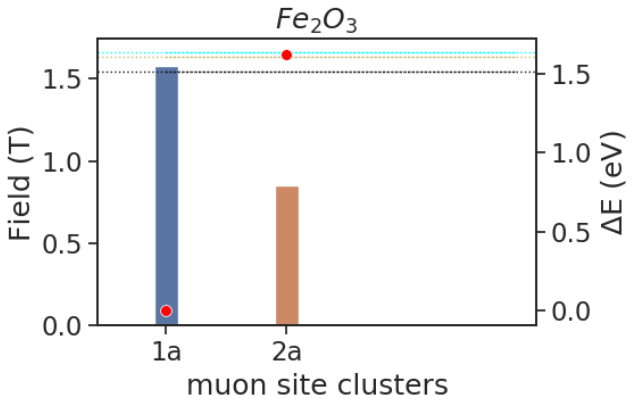

Figure 6.13: Workflow results for Fe_2O_3, see Table 6.2 for details of symbol description.

6.4.12 Cr_2S_3

Chromium Chalcogenide, Cr_2S_3 crystallizes in the R-3 (no. 148) space group with AFM order [222]. Structural relaxations were carried out with a $2 \times 2 \times 1$ supercell and workflow results are plotted in Fig. 6.14. Here, the workflow provides four low energy candidate muon sites in comparison with two distinct sites revealed from experiment [212]. The calculated local fields of the two lowest energy site(s) are in fair agreement with that from experiment but then there is no clear understanding of the site assignment with the workflow results.

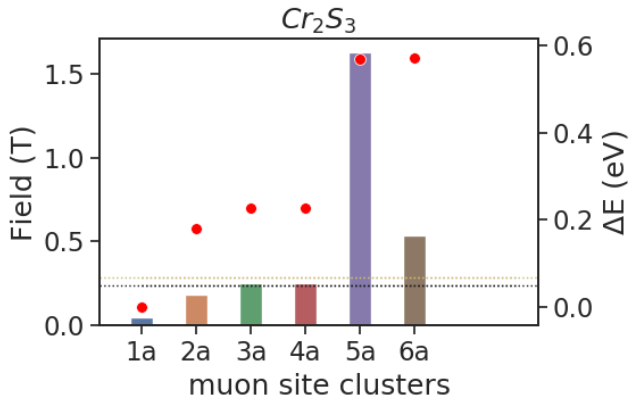

Figure 6.14: Workflow results for Cr_2S_3, see Table 6.2 for details of symbol description.

6.5 Discussions

From the case studies described above, we can discuss the capabilities of the workflow for the purpose of identifying the muon implantation site(s) and calculating the muon hyperfine interaction in magnetic compounds. The benchmark with the selected magnetic compounds indicate that generally the workflow is more reliable in identifying the muon stopping sites than in estimating the hyperfine field at the muon site. One of the reasons why the workflow is less successful for the local field calculation is because the accuracy in calculating the contact contribution (to the local field) is strongly dependent on the optimum level of the input computational parameters used and the accuracy in the description of the electronic and magnetic properties [26]. Another reason is that the effects of the muon vibrations have not been considered in calculating the contact contribution [5]. To analyze in particular, the results of the workflow in calculating the local field, we plot in Fig. 6.16 the deviation between calculated and experimental local field. Also in Fig. 6.15, we plot the percentage deviation of the calculated muon local field from experiment for each of the magnetic compounds. From Fig. 6.15, one notable failure of the workflow is on $LiMnPO_4$, where the deviation of the calculated value from experiment is above 500%. The problem with this compound is that the contact hyperfine contribution to the local field on this compound is expected to be vanishing [223], but then our workflow

[5] There is 1 to 18% correction to the contact hyperfine field due to this effect [139]

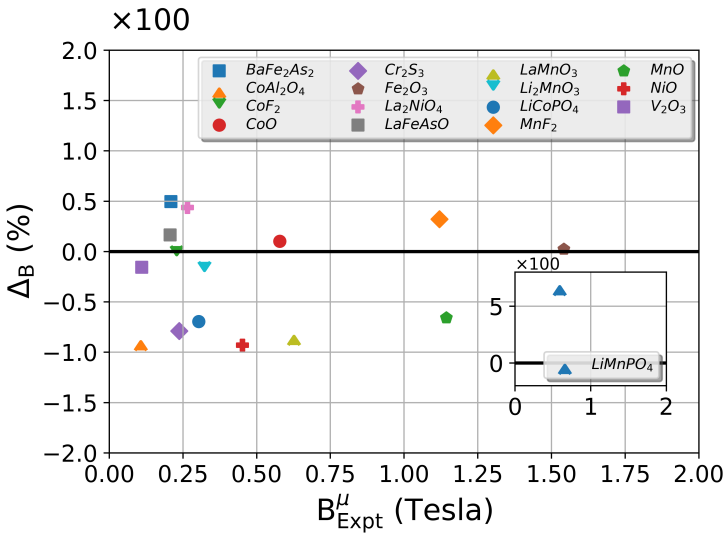

Figure 6.15: Plot of the calculated local field deviation ($\Delta_B = (B^{\mu}_{Calc} - B^{\mu}_{Expt})/B^{\mu}_{Expt}$ in percentage) as a function of experimental local field B^{μ}_{Expt} in Tesla of only the lowest energy muon-stopping site for each compound, where B^{μ}_{Calc} is the local field in Tesla calculated with the workflow.

results predict a large contact contribution. For all the magnetic compounds considered, the mean absolute percentage deviation (MAPD) is 84% but then if we exclude the $LiMnPO_4$ results, MAPD becomes 45%. This shows that generally our workflow is above 50% accurate in calculating the local field at the muon site.

In general, the workflow produces reliable results (for both the stopping sites and local field) in agreement with experiment in three of the compounds considered; LaFeAsO, $BaFe_2As_2$ and La_2NiO_4. However, for a number of other compounds, the workflow results do not provide enough useful details for understanding the experimental data. By studying the trend of the results, three major setbacks why the workflow fails have been identified, they include; (i) insufficient initial muon trial positions, (ii) the muon charge states were not considered and (iii) poor treatment of the electronic correlation. In the workflow, only the neutral supercells where used for calculations, however most of the magnetic compounds considered are antiferromagnetic insulators, and it has been shown [23, 25] that the muon charge is important for insulators unlike for metals where they are effectively screened. Thus, improvements in the subsequent version of the workflow include considering the muon charge in the use of a charged supercell.

Another particular feature of some of these magnetic compounds is that they are well known to be 'problematic' for conventional DFT [224–226]. For example, MnO is a prototype for the implementation of advanced theories in DFT to account for electron correlations, since the conventional DFT predicts it to be a metal where it is actually a Hubbard insulator [226]. Also, another challenge with the conventional DFT, is the accurate estimation of the magnetic moment as this is required for accurate quantitative estimation of the contact contribution to the hyperfine, this very relevant for systems where this contribution is dominant. Approaches to account for

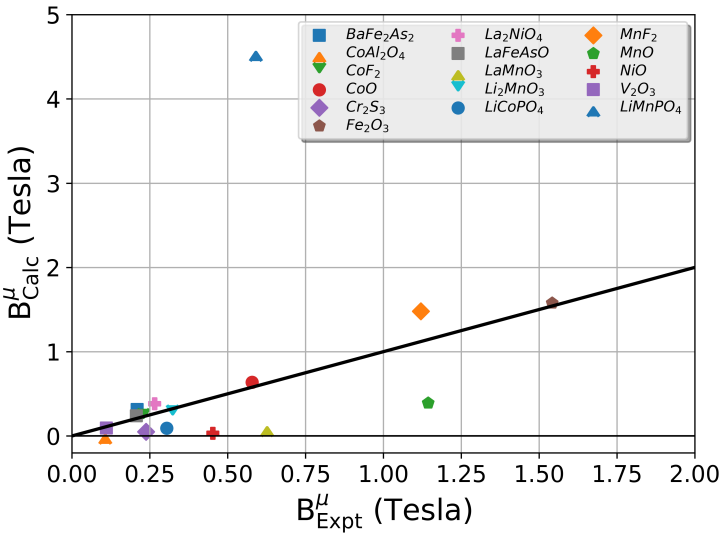

Figure 6.16: Plot of the calculated local field B^{μ}_{Calc} against the experimental local field B^{μ}_{Expt} in Tesla of only the lowest energy muon-stopping site for each compound. The solid black linear line (y=x with slope of 1) provides a guide to the deviation of B^{μ}_{Calc} from B^{μ}_{Expt}.

the electronic correlations with the conventional DFT are widely well developed but their application to proper calculations are either parameter dependent, not general for all compounds and have to be carefully applied on a case by case basis. These are challenges to be tackled in the HT approach for muon calculations. Also, it is well known that HT computations based on DFT pose a series of challenges in dealing with magnetic materials due to these limitations [163, 164]. Addressing these challenges consist of the future work and improvements to be implemented in the workflow.

6.6 Conclusion and Future work

In conclusion, in this chapter, I have described and provided a HT approach to automate the different levels of calculations for finding the muon site and estimating the hyperfine interactions. The workflow created for this purpose is implemented on the AiiDA integrated platform with calculations to be carried by standard DFT imported via the AiiDA plugins. The workflow has been benchmarked on 16 magnetic compounds and they have allowed to understand the workflow capabilities, its limitations and the likely implementations to consider to further improve the workflow in order to provide reliable results.

To improve the workflow for muon calculations and solve the challenges encountered, future work include; considering the effects of the muon charge states, fine sampling of the muon initial guess positions and implementing the approaches to treat electronic correlations such as the DFT+U, where fixed U values are to be used for each atomic specie. Even though it is well known that U values have to be considered for each compound but then this is expected to improve a lot the description of the electronic correlations and at least allow to reproduce the qualitative behaviour of

the bands in the vicinity of the Fermi level, which will in turn improve the workflow results. Another approach might be to instead adopt the strongly constrained and appropriately normed semilocal DFT (DFT+SCAN) which is not parameter dependent but then there are bottlenecks with calculation convergence for this approach.

CHAPTER 7

Magnetic properties and effects of muon charge localization in Cr_2S_3

In this chapter, I present the study of the electronic and magnetic properties of Cr_2S_3 as well as the study of the muon site(s) and its charge localization in this compound by *first-principle* calculations. Before continuing, it is worthwhile to point out that one of the motivation for this study is related to the previous chapter, where I have shown that conventional DFT implemented in the muon HT workflow failed to provide the description of the muon localization in Cr_2S_3 probably because of poor treatment of the electron correlation. Hence, here I implore the use of more optimized approaches, beyond the standard DFT to understand the electron correlation effects on the properties of Cr_2S_3 and the localization of the muon in this compound.

7.1 Introduction

Chromium Chalcogenide, Cr_2S_3 is of interest because of the colossal magnetoresistance property it exhibits that is promising for applications in spintronics and electronic devices [227, 228]. The magnetic, electric and transport properties have been studied. Earlier magnetization measurement [229] has shown that Cr_2S_3 has very weak spontaneous magnetization and is a ferrimagnet (FiM) with Curie temperature of 120 K. Neutron diffraction measurement [222] has shown that the magnetic structure is collinear, has three distinct magnetic sublatices which are ordered antiferromagnetically, where the FiM is suggested to arise from spin canting of the magnetic moment. However, another study [211] reports that FiM arises due to the existence of differences in the three distinct crystallographic Cr sites. Studies using X-Ray Magnetic Dichroism (XMCD) suggest an itinerant nature of d-electrons of Chromium [230]. Also, μSR [212] has been employed to study the magnetic properties of Cr_2S_3 where two distinct muon precession frequency $\nu_1(0) = 39$ MHz (0.2878 T) and $\nu_2(0) = 32.2$ MHz (0.2376 T) were observed at low temperature and sulphur deficiency was shown to drastically alter the magnetic properties.

Despite the broad interest on Cr_2S_3, only but few theoretical investigations [231–233] are found on the electronic and magnetic properties of Cr_2S_3. They only reported results do not properly consider the effects of electronic correlations and the magnetic order. Thus, in order to understand how these quantities affect the electronic and magnetic properties of Cr_2S_3, I have carried out collinear DFT, DFT+U and DFT+SCAN (Strongly Constrained and Appropriately Normed) calculations in the unitcell. The effects of the magnetic order on the electronic properties of the system are discussed. Further, with the more accurate treatment of the electron correlation effects, I now proceed to recalculate the muon stopping sites and hyperfine interactions while also discussing the localization of the muon charge.

7.2 Computational details

Spin-polarized plane-wave DFT calculations were performed using the Quantum Espresso code [82, 83]. The generalized gradient approximation (GGA) parametrized by Perdew-Burke-Ernzerhof (PBE) [134] was used for the exchange correlation potential. We have also considered the role of electron-electron interaction on Cr-d orbitals by using the Hubbard U method [234] implemented to describe the exchange correlation function. The value of $U_{eff} = U - J$ = 4.08 eV was used in this work determined by the linear response method [224, 235]. Also, I have treated the electronic correlations with the DFT+SCAN (meta-GGA) approach. DFT+SCAN has been shown to predict the band gaps correctly [236] and is also able to take into account the electronic correlation effects without the use of free parameters. For DFT and DFT+U calculations, the projected-augmented wave (PAW) [75] was used for the pseudopotentials while for the DFT+SCAN, I have used the norm-conserving pseudopotential of the Troullier-Martins type [237]. The plane wave cutoff of 100 Ry was used while for the charge density thi cutoff was increased by a factor of 10 for DFT and DFT+U calculations, and by a factor of 4 for DFT+SCAN. The Brillouin zone was sampled using a $9 \times 9 \times 8$ Monkhorst-Pack [67] grid. The Marzari-Vanderbilt [135] smearing function with width of 0.005 Ry was used.

In order to estimate muon-stopping-sites and spin densities at the muon sites, I have performed DFT+U calculations (with same U value as above) with a $2a \times 2b \times 1c$ supercell of Cr_2S_3 where the muon is treated as an impurity. Each of the supercells contain 120 Cr and S atoms and 1 muon. Here both the positively and neutral charged supercells were used to model μ^+ and μ respectively. For relaxations with the supercells, a $2 \times 2 \times 2$ Monkhorst-Pack grid of k-point was used while a denser $4 \times 4 \times 4$ grid was used for the estimation of the spin density in a single scf run. The initial guess positions for the muon consists of points from the symmetry reduced $5 \times 5 \times 5$ uniform grid. Structural relaxations where performed to total energy and total force thresholds of $1 \cdot 10^{-4}$ Ry and $1 \cdot 10^{-3}$ a.u respectively.

7.3 Results and Discussion

DFT structural relaxations of the Cr_2S_3 unit cell are in good agreement with experiment. Cr_2S_3 crystallizes in the R-3 (no. 148) space group [238] with lattice parameters $a = b = 5.94$, $c = 16.7$ Å where the three distinct Cr atoms occupy

the $3a$, $3b$ and $6c$ positions with the coordination (0, 0, 0), (0, 0, 0.5) and $\pm$(0, 0, z) respectively, and the S atom occupies the $18f$ positions with $\pm$(x,y,z) coordinates. The unit cell is shown in Fig. 7.1, each of the distinct Cr atom is octahedrally coordinated by six S atoms. The structure is characterized by face sharing (between Cr1 and Cr3 along the c axis) and edge sharing (between Cr2 and Cr3, also between Cr3a and Cr3b along the $a-b$ axis) between neighbor polyhedral complexes. Also, in the unit cell layers of Cr2 and Cr3 atoms are separated by a Cr1 layer along the c axis.

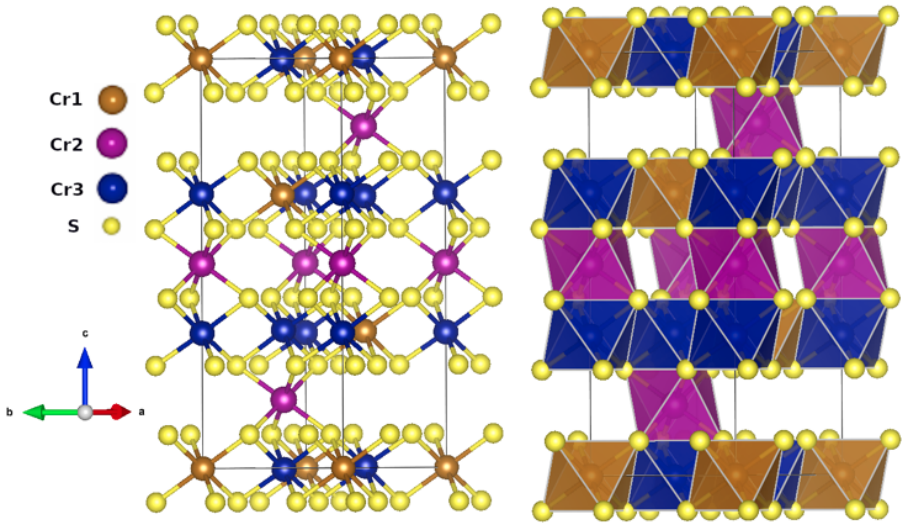

Figure 7.1: The unit cell of Cr_2S_3 with the polyhedra showing the octahedral coordination.

7.3.1 Magnetic order and electronic properties

In order to understand the effects of the magnetic order on the electronic properties, I have considered three different spin alignment on the Cr atoms, hence distinguishing three orders labelled AF1, AF2 and FM. The summary of the magnetic orders and calculations are presented in Table 7.1 for relaxations with DFT, DFT+U and DFT+SCAN calculations. From Table 7.1, one can observe that DFT calculations predict AF1 as the lowest energy magnetic order while the FM order is the lowest energy for both DFT+U and DFT+SCAN calculations, where electron correlation effects were taken into account. But then, observing the magnetic moment on both the Cr and S shows interesting behaviour relevant for the description of the electronic structure for each magnetic ordering. Of interest is the significant induced moment ($\approx$ 8% of those on Cr) on S atoms with opposite polarization to the moment on Cr for the FM order for both DFT+U and DFT+SCAN calculation. This together with the slightly different moment value on each Cr specie, results in an absolute total magnetization ($\sum|m|$) that is not equal to zero for AFM labelled orders and also not equal to the total magnetization ($\sum m$) of the cell for the FM labelled orders.

Table 7.1: The magnetic order and total energy differences ΔE in eV with respect to AF1 for DFT, DFT+U and DFT+SCAN are reported. The moments m in μ_B on Cr and S are presented.

	Order †	Label	ΔE(eV)	m(Cr1)	m(Cr2)	m(Cr3a)	m(Cr3b)	m(S)
DFT	↑↑↓↓	AF1	0.0	2.483	2.425	-2.414	-2.414	-0.002
	↑↓↑↓	AF2	0.1125	2.453	-2.430	2.423	-2.461	0.005 ‡
	↑↑↑↑	FM	0.3595	2.613	2.686	2.638	2.638	-0.044
DFT+U	↑↑↓↓	AF1	0.0	2.925	2.915	-2.913	-2.913	0.002
	↑↓↑↓	AF2	0.0408	2.908	-2.940	2.916	-2.925	0.003 ‡
	↑↑↑↑	FM	-0.1241	2.944	3.039	3.007	3.007	-0.232
SCAN	↑↑↓↓	AF1	0.0	3.012	3.014	-3.050	-3.050	0.016
	↑↓↑↓	AF2	0.0236	3.023	-3.034	3.045	-3.039	0.015 ‡
	↑↑↑↑	FM	-0.1469	3.035	3.095	3.120	3.120	-0.251

† The order of the spin arrangement is for Cr atoms with the sequence (Cr1, Cr2, Cr3(a), Cr3(b)) where 3a and 3b distinguishes the equivalent Cr3 atoms in the 6c position.

‡ In this magnetic order, the moment S, takes two values, the one in the table and -0.001, 0.021 and -0.001μ_B for DFT, DFT+U and SCAN respectively.

The calculated moment on each Cr for all cases are overestimated in comparison with those of experiments (2.05μ_B [239], 2.07μ_B [229] and 1.2μ_B [240]). The large value of the magnetic moment on Cr is an indicator of the itinerant nature of the d-electrons already pointed out in Ref. [230]. Also, the fact that the behaviour of the magnetic moments are significantly different with each magnetic ordering suggest that the electronic properties of Cr_2S_3 is indeed magnetic order dependent.

I now discuss the density of states (DOS) of the AF1 and FM labelled structures. The DOS and projected density of states (PDOS) are shown in Fig. 7.2. The plot shows very small band gap approximately 0.45 eV for DFT, 0.35 eV for DFT+U and 1.0 eV for SCAN for the AF1 structure. As expected, the 1.0 eV gap from SCAN is in better agreement with 1.1 eV of experiment [231]. I now discuss the contribution of the atomic orbitals in the vicinity of the Fermi level. From Fig. 7.2, the dominant contribution are from orbitals with S-p and Cr-d character. But then, for DFT calculation, the Cr-d have the larger contribution but this is not the case with DFT+U and SCAN where the S-p contribution dominates. This variation is due to the better accurate treatment of electronic correlations with the beyond DFT approaches and most likely accounts for the failure encountered for the muon calculations with DFT, presented in the previous chapter (Chap. 6). I now take into considerations these electronic correlations and perform the muon calculations with DFT+U using the AF1 structure[1].

[1] This is also the experimentally identified magnetic structure

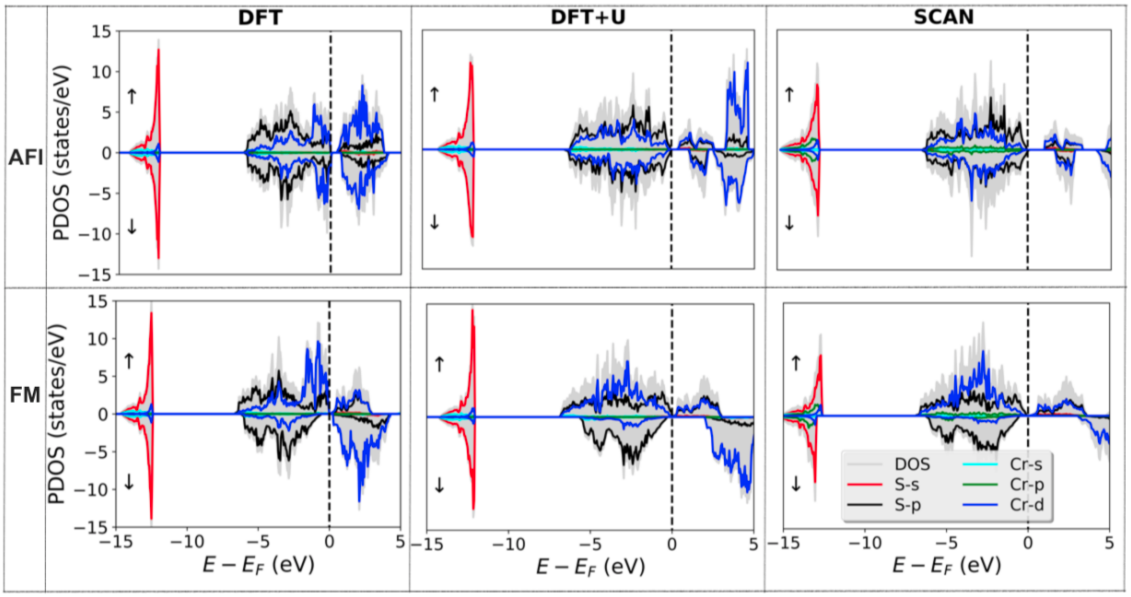

Figure 7.2: The density of states (gray background) and projected density of states (Cr and S) for both the majority spin (↑) and minority spin (↓) channel of both AF1 and FM (for DFT, DFT+U and DFT+SCAN calculations). The zero energy is set to the VBM.

7.3.2 Muon-stopping sites and hyperfine interactions

The structural relaxations with supercells for the muon search reveal two distinct inequivalent candidate stopping sites for each of the charge-neutral (0) and charge-positive (+) state. The summary of the sites together with the DFT+U estimated contact contribution to the hyperfine field is reported in Table 7.2, while the sites are shown in the unitcell together with the minimum of the electrostatic potential in Fig. 7.3. In both charge states, sites B_+ and B_0 can safely be ruled out as they are of high energy $\approx$ 1 eV, even larger than a typical muon zero point vibration energy.

Table 7.2: The calculated muon-stopping sites for both muon-charge states and their respective energy difference ΔE in eV. DFT+U calculated hyperfine contact field $B_{\text{Cont}}^{\text{DFT}}$ in Tesla.

Charge	Label	Muon site, $\boldsymbol{r}_\mu$	ΔE (eV)	$B_{\text{Cont}}^{\text{DFT}}$ (T)
+	A_+	(0.4895, 0.4853, 0.4931)	0.0000	+0.0327
	B_+	(0.3333, 0.6667, 0.5630)	0.9495	-0.6126
0	A_0	(0.4911, 0.4866, 0.4934)	0.0000	+0.0520
	B_0	(0.1781, 0.1810, 0.4145)	0.9965	-0.1966

Sites A_+ and A_0 are of low energy and thus are probable sites for the muon implantation. Both sites even though of different charge states are symmetrically equivalent. These sites are attracted to the electronegative sulphur atoms and form unequal bonds with them with μ-S distance of 1.47 Å and 1.80 Å and S-μ-S angle of $\approx$178°. The nearest Cr atom to both sites is at distance of $\approx$ 3 Å. Considering that in μSR measurement for Cr_2S_3 [212] two distinct muon sites with local field of

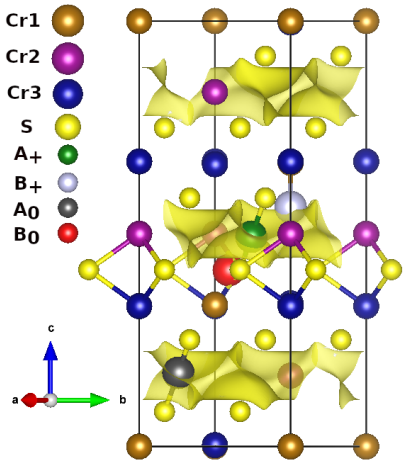

Figure 7.3: The figure show the calculated candidate sites listed in Table 7.2 and the minmium of the electrostatic potential (yellow isosurface). The figure is visualised using VESTA [88].

0.2878 T and 0.2376 T were observed, the muon stopping sites in Cr_2S_3 are those of the symmetry equivalent site(s) (A_+ and A_0) with different charge states. Hence, I proceed to account and discuss these observed muon local fields at these sites.

In order to calculate the muon local ($B_{\text{calc}} = B_{\text{Dip}} + B_{\text{Cont}}$, see Chap. 2 for details) an estimate of the dipolar and contact contribution is required, these quantities are dependent on the muon sites and the magnetic moment. Dipolar calculations were performed using the the relaxed positions for Cr and S in the supercell with the muon impurity and the AF1 structure was adopted. Already, the DFT+U calculated values of the contact contribution $B^{\text{DFT}}_{\text{Cont}}$ are reported in Table 7.2. However, we have pointed out above that calculations from DFT+U over-estimate the magnetic moments, thus one way to proceed is to estimate the magnetic moment by calculating the local field at the muon over a range of moments and then compare with experiment. But before this, the calculated contact field contribution from DFT has to be rescaled with each of the new Cr moment m_{Cr} as;

$$B_{\text{Cont}} = B^{DFT}_{\text{Cont}} \cdot \frac{m_{\text{Cr}}}{m^{\text{DFT}}_{\text{Cr}}} \tag{7.1}$$

where $\text{m}^{DFT}_{\text{Cr}} = 2.93\mu_B$. The calculated muon local field B_{calc} for magnetic moment ranging from 1 to 3.5 μ_B are plotted in Fig. 7.4a for sites A_+ and A_0, where the horizontal lines indicate the experimentally observed local field at the muon B_{exp}. Edges of the grey shaded vertical lines are used to indicate where the B_{calc} and B_{exp} meet, which are at Cr moments of 1.82 μ_B and 2.15 μ_B. Another, approach to calculate the best fit magnetic moment with both sites (1 and 2), is to find the magnetic moment that minimizes the relation;

$$\chi = \sqrt{\left[(B^1_{\text{calc}} - B^1_{\text{expt}})/B^1_{\text{expt}}\right]^2 + \left[(B^2_{\text{calc}} - B^2_{\text{exp}})/B^2_{\text{exp}}\right]^2}. \tag{7.2}$$

This relation is plotted in Fig. 7.4b and the Cr moment that minimizes the relation is $\sim$2 μ_B. Hence the plots in Fig. 7.4 show that site A_+ accounts for the higher

muon local field of 0.2877 T, while A_0 accounts for the 0.2376 T field. Our muon calculations predicts that the Cr moment is within the range of 1.82 to 2.15 μ_B in very good agreement with experiments (2.05μ_B [239] and 2.07μ_B [229]).

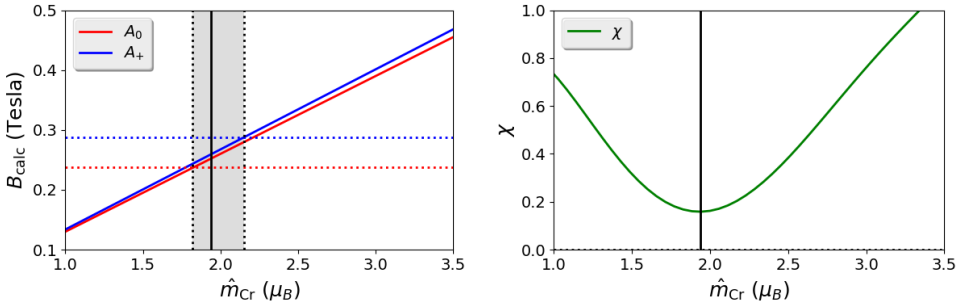

(a) **(b)**

Figure 7.4: (a) Calculated local field at muon sites, A_+ and A_0 as a function of Cr moment. Horizontal red (0.2376 T) and blue (0.2877 T) line] are observed μSR fields [212]. (b) Plot of the relation in Equation (7.2) as a function of Cr moment. The solid vertical line in both plots is at Cr = 1.94 μ_B, the moment that minimizes the relation, Equation (7.2).

This shows that indeed DFT overestimates the calculation of the magnetic moment. I further plot in Fig. 7.6 the contributions to the local field using the DFT+U moment (Fig. 7.5a), to show this overestimation and then also another plot (Fig. 7.5b) to show agreement with experiment using the muon calculations determined Cr moment of 1.82 μ_B. In all, the accurate muon calculation results show that the failure of our workflow discussed in the previous chapter (Chap.6), is due to inaccurate treatment of the electron correlation effects in Cr_2S_3.

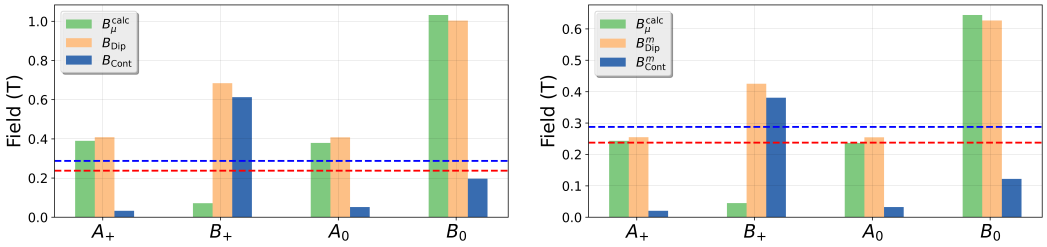

(a) **(b)**

Figure 7.5: Bar plot of the contributions (dipolar (brown)), contact (blue)) to the local field (red and blue dashed lines are experiment values): with (a) DFT+U moments size, (b) m_{Cr} = 1.82μ_B, the lower bound of the shaded area in Fig. 7.4a.

7.3.3 Muon-charge localization

Now, I discuss the localization of the muon charge in both the charged and neutral supercells. The localization of the muon charge is shown with the isosurface charge

density plots in Fig. 7.6. The plot shows that for Cr_2S_3 the muon charge is predominantly localized at its implantation site while also a significant localization of the muon charge is found on the nearest S atom bonding to the muon at a distance of 1.47 Å. Also reducing the isosurface level in Fig. 7.6, one also finds that a little fraction of the charge is located at the next nearest bonding S atom at 1.80 Å. Unlike in Fe_2O_3 [209] and Cr_2O_3 [241] were the localization of large fraction of the muon charge (in the neutral charged regime) on the neighbour transition metal atom leads to the formation muon-polaron complex, here only negligible fraction of the muon charge are found on Cr for the charge neutral supercell. This negligible charge also do not show any splitting of the Cr-*d* level states.

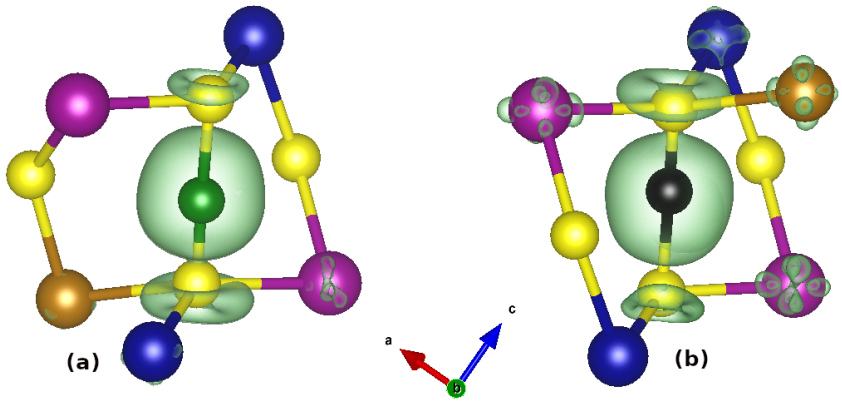

Figure 7.6: Isosurface plots of the muon charge for the (a) charge-positive A_+ (green spheres) and (b) charge-neutral A_0 (black sphere) for ∼0.003 eV/A^3 iso-level.

7.4 Conclusion

I have studied from first principles the electronic and magnetic properties of Cr_2S_3 as well as the muon sites and interaction in this compound. Results of the calculations indicate that accurate treatment of electron correlation beyond DFT is required to describe properly the properties of the system. The electronic properties of Cr_2S_3 were shown to be strongly dependent on the magnetic ordering. I have gone further to identify the muon sites, of which together with analysis of the muon local field allowed to predict with μSR the Cr magnetic moment in agreement with other experiments.

Finally, results of this chapter have provided insights on possible approaches to implement in the improvement of the workflow for high-throughput muon calculations, particularly that of better treatment of the electron correlations not fully captured within the standard DFT.

CHAPTER 8

Summary and Conclusion

The results presented in this thesis have demonstrated the effectiveness of the first principle approaches in identifying candidate muon stopping sites and understanding their local interactions in order to support the analysis of μSR experimental data. These first principle approaches based on DFT involve a number of calculation protocols that require intensive human intervention, thus I have also presented a high throughput approach developed to automate these protocols.

In the first three chapters, I have presented the μSR experimental and DFT theoretical backgrounds underlying the findings presented in this thesis together with the practical calculation procedures and protocols for finding the muon site and hyperfine interactions. In chapter four, I have described the efficient approach by Celio for the simulation of the muon time dependent spin polarization on the quantum level and I have demonstrated its usage in fluorides, copper and MnSi.

In chapter five, to characterize the ferromagnetic ground state of Fe_2P, we have used first principle calculations to provide improved understanding of data from μSR and NMR spectroscopic measurements. Here, using the supercell calculation strategy and protocols, we have accurately identified where the muons stop in this compound and as well the muon hyperfine coupling constants which allowed to interpret the μSR data. Also, the hyperfine coupling constants at the P nuclei calculated from first principle allowed to characterize NMR peaks, all providing a complete analysis of the FM phase of this compound.

Further in chapter six, I present an automatic workflow embedding all the time consuming procedures of muon sites calculations and based on the existing AiiDA integrated platform, that allows for automation, managing, storing data and tracking the calculation history. Automation within the DFT based HT approaches is well known to encounter a number of challenges, as beyond conventional DFT approaches for improved treatment of electronic correlation are known to be case by case dependent, hence providing setbacks for automation. But then as a starting point, we have presented in this thesis, the workflow for the muon calculation protocols limited to implementation with only conventional DFT. The workflow was benchmarked on 16 selected magnetic compounds from the MAGNDATA database.

Results of the benchmark show that while automation and efficient data management and storage were achieved, the workflow is more accurate in the determination of the muon implantation site(s) than in calculating the hyperfine fields. Also, as expected, the benchmark shows that the workflow accurately reproduces the experimental results in compounds where conventional DFT describes correctly the electronic and magnetic properties while it fails in compounds where beyond DFT approaches are required to treat electronic correlations. Further work to improve the accuracy of this approach is to introduce in the workflow a more general parametrized beyond DFT approaches at least to ensure that core material propertied are captured.

To this end, we have considered in chapter seven the role of improved first principle treatments of electronic correlations in Cr_2S_3, one of the magnetic compounds considered in the benchmark above. Expectedly, correlations play important role in the magnetic ground state of this compound and their improved treatment allowed to properly identify the muon implantation sites, hyperfine interactions and roles of muon charge localization in this compound.

References

[1] A. Schenck. *Muon spin rotation spectroscopy: Principles and applications in solid state physics*. United States: Taylor and Francis Inc, 1985. URL: http://inis.iaea.org/search/search.aspx?orig_q=RN:19081274 (cit. on pp. 1, 4, 7, 11).

[2] S. J. Blundell. "Spin-polarized muons in condensed matter physics". In: *Contemporary Physics* 40.3 (1999), 175–192. DOI: 10.1080/001075199181521. URL: http://dx.doi.org/10.1080/001075199181521 (cit. on pp. 1, 4, 5, 7, 8).

[3] Alain Yaouanc and Pierre Dalmas de Réotier. *Muon spin rotation, relaxation, and resonance: applications to condensed matter*. International series of monographs on physics. Oxford: Oxford Univ. Press, 2011. URL: https://cds.cern.ch/record/1385534 (cit. on pp. 1, 4, 7, 10, 11, 14, 15).

[4] Stephen J. Blundell, Roberto De Renzi, Tom Lancaster, and Francis L. Pratt. *Muon Spectroscopy: An Introduction*. Oxford University Press, 2021 (cit. on pp. 1, 4, 7).

[5] Y.J. Uemura and G.M. Luke. "Muon spin relaxation studies in strongly correlated electron systems". In: *Physica B: Condensed Matter* 186-188 (1993), 223–228. DOI: https://doi.org/10.1016/0921-4526(93)90537-G. URL: https://www.sciencedirect.com/science/article/pii/092145269390537G (cit. on p. 1).

[6] Y.J. Uemura. "Muon spin relaxation studies on high-Tc, organic, heavy-fermion, and Chevrel phase superconductors". In: *Physica B: Condensed Matter* 169.1 (1991), 99–106. DOI: https://doi.org/10.1016/0921-4526(91)90214-Y. URL: https://www.sciencedirect.com/science/article/pii/092145269190214Y (cit. on p. 1).

[7] Y. J. Uemura, L. P. Le, G. M. Luke, B. J. Sternlieb, W. D. Wu, J. H. Brewer, T. M. Riseman, C. L. Seaman, M. B. Maple, et al. "Basic similarities among cuprate, bismuthate, organic, Chevrel-phase, and heavy-fermion superconductors shown by penetration-depth measurements". In: *Phys. Rev. Lett.* 66 (20 1991), 2665–2668. DOI: 10.1103/PhysRevLett.66.2665. URL:

https://link.aps.org/doi/10.1103/PhysRevLett.66.2665 (cit. on p. 1).

[8] H. Keller. "Muon-spin rotation experiments in high-Tc superconductors and related materials". In: *IBM Journal of Research and Development* 33.3 (1989), 314–323. DOI: 10.1147/rd.333.0314 (cit. on p. 1).

[9] H. Luetkens, H.-H. Klauss, M. Kraken, F. J. Litterst, T. Dellmann, R. Klingeler, C. Hess, R. Khasanov, A. Amato, et al. "The electronic phase diagram of the $LaO_{1-x}F_xFeAs$ superconductor". In: *Nature Materials* 8.4 (2009), 305–309. DOI: 10.1038/nmat2397. URL: https://doi.org/10.1038/nmat2397 (cit. on p. 1).

[10] W.A. MacFarlane, O. Ofer, K.H. Chow, M.D. Hossain, T.J. Parolin, H. Saadaoui, Q. Song, D. Wang, D.J. Arseneau, et al. "Longitudinal Field Muon Spin Rotation Study of Magnetic Freezing in Fe Rich FeSe0.25Te0.75". In: *Physics Procedia* 30 (2012). 12th International Conference on Muon Spin Rotation, Relaxation and Resonance (μSR2011), 254–257. DOI: https://doi.org/10.1016/j.phpro.2012.04.085. URL: https://www.sciencedirect.com/science/article/pii/S1875389212012710 (cit. on pp. 1, 62).

[11] J. E. Sonier, W. Huang, C. V. Kaiser, C. Cochrane, V. Pacradouni, S. A. Sabok-Sayr, M. D. Lumsden, B. C. Sales, M. A. McGuire, A. S. Sefat, and D. Mandrus. "Magnetism and Disorder Effects on Muon Spin Rotation Measurements of the Magnetic Penetration Depth in Iron-Arsenic Superconductors". In: *Phys. Rev. Lett.* 106 (12 2011), 127002. DOI: 10.1103/PhysRevLett.106.127002. URL: https://link.aps.org/doi/10.1103/PhysRevLett.106.127002 (cit. on p. 1).

[12] Y.J. Uemura, L.P. Le, G.M. Luke, B.J. Sternlieb, J.H. Brewer, R. Kadono, R.F. Kiefl, S.R. Kreitzman, and T.M. Riseman. "Probing magnetism and superconductivity of high-Tc systems with positive muons". In: *Physica C: Superconductivity and its Applications* 162-164 (1989), 857–860. DOI: https://doi.org/10.1016/0921-4534(89)90493-0. URL: https://www.sciencedirect.com/science/article/pii/0921453489904930 (cit. on p. 1).

[13] Jeff E. Sonier, Jess H. Brewer, and Robert F. Kiefl. "μSR studies of the vortex state in type-II superconductors". In: *Rev. Mod. Phys.* 72 (3 2000), 769–811. DOI: 10.1103/RevModPhys.72.769. URL: https://link.aps.org/doi/10.1103/RevModPhys.72.769 (cit. on pp. 1, 12).

[14] S. J. Ray, A. S. Gibbs, S. J. Bending, P. J. Curran, E. Babaev, C. Baines, A. P. Mackenzie, and S. L. Lee. "Muon-spin rotation measurements of the vortex state inSr2RuO4: Type-1.5 superconductivity, vortex clustering, and a crossover from a triangular to a square vortex lattice". In: *Physical Review B* 89.9 (2014). DOI: 10.1103/physrevb.89.094504. URL: http://dx.doi.org/10.1103/PhysRevB.89.094504 (cit. on p. 1).

[15] Bruce D. Patterson. "Muonium states in semiconductors". In: *Rev. Mod. Phys.* 60 (1 1988), 69–159. DOI: 10.1103/RevModPhys.60.69. URL: https://link.aps.org/doi/10.1103/RevModPhys.60.69 (cit. on p. 1).

[16] T. L. Estle and R. L. Lichti. "Muonium in semiconductors and some implications for hydrogen impurities". In: *Hyperfine Interactions* 97.1 (1996), 171–192. DOI: 10.1007/BF02150174. URL: https://doi.org/10.1007/BF02150174 (cit. on p. 1).

[17] S. R. Kreitzman, B. Hitti, R. L. Lichti, T. L. Estle, and K. H. Chow. "Muon-spin-resonance study of muonium dynamics in Si and its relevance to hydrogen". In: *Phys. Rev. B* 51 (19 1995), 13117–13137. DOI: 10.1103/PhysRevB.51.13117. URL: https://link.aps.org/doi/10.1103/PhysRevB.51.13117 (cit. on p. 1).

[18] A. Amato, R. Feyerherm, F. N. Gygax, and A. Schenck. "μ+-site in heavy-fermion compounds". In: *Hyperfine Interactions* 104.1 (1997), 115–125. DOI: 10.1023/A:1012611422979. URL: https://doi.org/10.1023/A:1012611422979 (cit. on pp. 1, 12).

[19] R. Feyerherm, A. Amato, A. Grayevsky, F. N. Gygax, N. Kaplan, and A. Schenck. "Crystal electric field next to a hydrogen-like interstitial— μ+ in PrNi5". In: *Zeitschrift für Physik B Condensed Matter* 99.1 (1995), 3–13. DOI: 10.1007/s002570050002. URL: https://doi.org/10.1007/s002570050002 (cit. on pp. 1, 12).

[20] R. F. Kiefl, M. Celio, T. L. Estle, G. M. Luke, S. R. Kreitzman, J. H. Brewer, D. R. Noakes, E. J. Ansaldo, and K. Nishiyama. "Determination of the electronic structure of anomalous muonium in GaAs from nuclear hyperfine interactions". In: *Phys. Rev. Lett.* 58 (17 1987), 1780–1783. DOI: 10.1103/PhysRevLett.58.1780. URL: https://link.aps.org/doi/10.1103/PhysRevLett.58.1780 (cit. on p. 1).

[21] G. M. Luke, J. H. Brewer, S. R. Kreitzman, D. R. Noakes, M. Celio, R. Kadono, and E. J. Ansaldo. "Muon diffusion and spin dynamics in copper". In: *Phys. Rev. B* 43 (4 1991), 3284–3297. DOI: 10.1103/PhysRevB.43.3284. URL: https://link.aps.org/doi/10.1103/PhysRevB.43.3284 (cit. on p. 1).

[22] M. Celio. "New Method to Calculate the Muon Polarization Function". In: *Phys. Rev. Lett.* 56 (25 1986), 2720–2723. DOI: 10.1103/PhysRevLett.56.2720. URL: https://link.aps.org/doi/10.1103/PhysRevLett.56.2720 (cit. on pp. 1, 29, 31, 37, 40).

[23] J. S. Möller, D. Ceresoli, T. Lancaster, N. Marzari, and S. J. Blundell. "Quantum states of muons in fluorides". In: *Phys. Rev. B* 87 (12 2013), 121108. DOI: 10.1103/PhysRevB.87.121108. URL: https://link.aps.org/doi/10.1103/PhysRevB.87.121108 (cit. on pp. 1, 26, 36, 37, 54, 69).

[24] F. Bernardini, P. Bonfà, S. Massidda, and R. De Renzi. "Ab initio strategy for muon site assignment in wide band gap fluorides". In: *Physical Review B* 87.11 (2013). DOI: 10.1103/physrevb.87.115148. URL: http://dx.doi.org/10.1103/PhysRevB.87.115148 (cit. on pp. 1, 26, 36, 37).

[25] J S Möller, P Bonfà, D Ceresoli, F Bernardini, S J Blundell, T Lancaster, R De Renzi, N Marzari, I Watanabe, S Sulaiman, and M I Mohamed-Ibrahim. "Playing quantum hide-and-seek with the muon: localizing muon stopping sites". In: *Physica Scripta* 88.6 (2013), 068510. DOI: 10.1088/0031-8949/88/06/068510. URL: https://doi.org/10.1088%2F0031-8949%2F88%2F06%2F068510 (cit. on pp. 1, 52, 69).

[26] Ifeanyi John Onuorah, Pietro Bonfà, and Roberto De Renzi. "Muon contact hyperfine field in metals: A DFT calculation". In: *Physical Review B* 97.17 (2018). DOI: 10.1103/physrevb.97.174414. URL: http://dx.doi.org/10.1103/PhysRevB.97.174414 (cit. on pp. 1, 15, 54, 58, 68).

[27] Siti Nur Afifi Ahmad, Shukri Sulaiman, Dang Fatihah Hasan Baseri, Lee Sin Ang, Nor Zakiah Yahaya, Hasni Arsad, and Isao Watanabe. "Density Functional Theory Studies of Muon Stopping Sites and Hyperfine Interaction in [Au25(SR)18]0 Nanocluster". In: *Journal of the Physical Society of Japan* 89.1 (2020), 014301. DOI: 10.7566/JPSJ.89.014301. eprint: https://doi.org/10.7566/JPSJ.89.014301. URL: https://doi.org/10.7566/JPSJ.89.014301 (cit. on pp. 1, 54).

[28] Leandro Liborio, Simone Sturniolo, and Dominik Jochym. "Computational prediction of muon stopping sites using ab initio random structure searching (AIRSS)". In: *The Journal of Chemical Physics* 148.13 (2018), 134114. DOI: 10.1063/1.5024450. eprint: https://doi.org/10.1063/1.5024450. URL: https://doi.org/10.1063/1.5024450 (cit. on pp. 1, 54).

[29] B M Huddart, M T Birch, F L Pratt, S J Blundell, D G Porter, S J Clark, W Wu, S R Julian, P D Hatton, and T Lancaster. "Local magnetism, magnetic order and spin freezing in the 'nonmetallic metal' FeCrAs". In: *Journal of Physics: Condensed Matter* 31.28 (2019), 285803. DOI: 10.1088/1361-648x/ab151f. URL: https://doi.org/10.1088/1361-648x/ab151f (cit. on pp. 1, 48, 54).

[30] Kévin J. A. Franke, Benjamin M. Huddart, Thomas J. Hicken, Fan Xiao, Stephen J. Blundell, Francis L. Pratt, Marta Crisanti, Joel A. T. Barker, Stewart J. Clark, et al. "Magnetic phases of skyrmion-hosting $GaV_4S_{8-y}Se_y$ $(y = 0, 2, 4, 8)$ probed with muon spectroscopy". In: *Phys. Rev. B* 98 (5 2018), 054428. DOI: 10.1103/PhysRevB.98.054428. URL: https://link.aps.org/doi/10.1103/PhysRevB.98.054428 (cit. on pp. 1, 54).

[31] T Lancaster, F Xiao, B M Huddart, R C Williams, F L Pratt, S J Blundell, S J Clark, R Scheuermann, T Goko, et al. "Quantum magnetism in molecular spin ladders probed with muon-spin spectroscopy". In: *New Journal of Physics* 20.10 (2018), 103002. DOI: 10.1088/1367-2630/aae21a. URL: https://doi.org/10.1088/1367-2630/aae21a (cit. on pp. 1, 54).

[32] F. Xiao, J. S. Möller, T. Lancaster, R. C. Williams, F. L. Pratt, S. J. Blundell, D. Ceresoli, A. M. Barton, and J. L. Manson. "Spin diffusion in the low-dimensional molecular quantum Heisenberg antiferromagnet $Cu(pyz)(NO_3)_2$ detected with implanted muons". In: *Phys. Rev. B* 91 (14 2015), 144417. DOI: 10.1103/PhysRevB.91.144417. URL: https://link.aps.org/doi/10.1103/PhysRevB.91.144417 (cit. on pp. 1, 54).

[33] B. M. Huddart, I. J. Onuorah, M. M. Isah, P. Bonfà, S. J. Blundell, S. J. Clark, R. De Renzi, and T. Lancaster. "Intrinsic Nature of Spontaneous Magnetic Fields in Superconductors with Time-Reversal Symmetry Breaking". In: *Phys. Rev. Lett.* 127 (23 2021), 237002. DOI: 10.1103/PhysRevLett.127.237002. URL: https://link.aps.org/doi/10.1103/PhysRevLett.127.237002 (cit. on pp. 1, 54).

[34] Carl D. Anderson and Seth H. Neddermeyer. "Cloud Chamber Observations of Cosmic Rays at 4300 Meters Elevation and Near Sea-Level". In: *Phys. Rev.* 50 (4 1936), 263–271. DOI: 10.1103/PhysRev.50.263. URL: https://link.aps.org/doi/10.1103/PhysRev.50.263 (cit. on p. 4).

[35] Seth H. Neddermeyer and Carl D. Anderson. "Cosmic-Ray Particles of Intermediate Mass". In: *Phys. Rev.* 54 (1 1938), 88–89. DOI: 10.1103/PhysRev.54.88.2. URL: https://link.aps.org/doi/10.1103/PhysRev.54.88.2 (cit. on p. 4).

[36] J. C. Street and E. C. Stevenson. "New Evidence for the Existence of a Particle of Mass Intermediate Between the Proton and Electron". In: *Phys. Rev.* 52 (9 1937), 1003–1004. DOI: 10.1103/PhysRev.52.1003. URL: https://link.aps.org/doi/10.1103/PhysRev.52.1003 (cit. on p. 4).

[37] Richard L. Garwin, Leon M. Lederman, and Marcel Weinrich. "Observations of the Failure of Conservation of Parity and Charge Conjugation in Meson Decays: the Magnetic Moment of the Free Muon". In: *Phys. Rev.* 105 (4 1957), 1415–1417. DOI: 10.1103/PhysRev.105.1415. URL: https://link.aps.org/doi/10.1103/PhysRev.105.1415 (cit. on pp. 4, 6).

[38] T. D. Lee and C. N. Yang. "Parity Nonconservation and a Two-Component Theory of the Neutrino". In: *Phys. Rev.* 105 (5 1957), 1671–1675. DOI: 10.1103/PhysRev.105.1671. URL: https://link.aps.org/doi/10.1103/PhysRev.105.1671 (cit. on pp. 5, 6).

[39] L Nuccio, L Schulz, and A J Drew. "Muon spin spectroscopy: magnetism, soft matter and the bridge between the two". In: *Journal of Physics D: Applied Physics* 47.47 (2014), 473001. DOI: 10.1088/0022-3727/47/47/473001. URL: https://doi.org/10.1088/0022-3727/47/47/473001 (cit. on p. 6).

[40] S. L. Lee, S. H. Kilcoyne, and R. Cywinski, eds. *Muon science: Muons in physics, chemistry and materials: Proceedings, 51st Scottish Universities Summer School in Physics, NATO Advanced Study Institute, St. Andrews, UK, August 17-28, 1998*. Edinburgh, UK: SUSSP, 1999 (cit. on pp. 7, 9, 10).

[41] R. S. Hayano, Y. J. Uemura, J. Imazato, N. Nishida, T. Yamazaki, and R. Kubo. "Zero-and low-field spin relaxation studied by positive muons". In: *Phys. Rev. B* 20 (3 1979), 850–859. DOI: 10.1103/PhysRevB.20.850. URL: https://link.aps.org/doi/10.1103/PhysRevB.20.850 (cit. on pp. 10, 12, 13, 40).

[42] Y. J. Uemura, T. Yamazaki, D. R. Harshman, M. Senba, and E. J. Ansaldo. "Muon-spin relaxation in AuFe and CuMn spin glasses". In: *Phys. Rev. B* 31 (1 1985), 546–563. DOI: 10.1103/PhysRevB.31.546. URL: https://link.aps.org/doi/10.1103/PhysRevB.31.546 (cit. on pp. 10, 11).

[43] R. Kubo and T. Toyabe. Ed. by R. Blinc. Amsterdam: North-Holland, 1967 (cit. on p. 10).

[44] Ryogo Kubo. "A stochastic theory of spin relaxation". In: *Hyperfine Interactions* 8.4 (1981), 731–738. DOI: 10.1007/BF01037553. URL: https://doi.org/10.1007/BF01037553 (cit. on pp. 10, 11).

[45] R. E. Walstedt and L. R. Walker. "Nuclear-resonance line shapes due to magnetic impurities in metals". In: *Phys. Rev. B* 9 (11 1974), 4857–4867. DOI: 10.1103/PhysRevB.9.4857. URL: https://link.aps.org/doi/10.1103/PhysRevB.9.4857 (cit. on p. 11).

[46] Y. J. Uemura. "Muon spin relaxation studies on high-TC superconductors and related antiferromagnets (invited)". In: *Journal of Applied Physics* 64.10 (1988), 6087–6091. DOI: 10.1063/1.342127. eprint: https://doi.org/10.1063/1.342127. URL: https://doi.org/10.1063/1.342127 (cit. on p. 13).

[47] J.I. Budnick, A. Golnik, Ch. Niedermayer, E. Recknagel, M. Rossmanith, A. Weidinger, B. Chamberland, M. Filipkowski, and D.P. Yang. "Observation of magnetic ordering in La2CuO4 by muon spin rotation spectroscopy". In: *Physics Letters A* 124.1 (1987), 103–106. DOI: https://doi.org/10.1016/0375-9601(87)90382-3. URL: https://www.sciencedirect.com/science/article/pii/0375960187903823 (cit. on p. 13).

[48] I. Watanabe, T. Adachi, K. Takahashi, S. Yairi, Y. Koike, and K. Nagamine. "Muon-spin-relaxation study of the effect of nonmagnetic impurities on the Cu-spin fluctuations in $La_{2-x}Sr_xCu_{1-y}Zn_yO_4$ around $x = 0.115$". In: *Phys. Rev. B* 65 (18 2002), 180516. DOI: 10.1103/PhysRevB.65.180516. URL: https://link.aps.org/doi/10.1103/PhysRevB.65.180516 (cit. on p. 13).

[49] P.A. Pattenden, R.M. Valladares, F.L. Pratt, S.J. Blundell, A.J. Fisher, W. Hayes, and T. Sugano. "μSR studies of magnetism in the organic systems p-NPNN and 3-QNNN". In: *Synthetic Metals* 71.1 (1995). Proceedings of the International Conference on Science and Technology of Synthetic Metals (ICSM '94), 1823–1824. DOI: https://doi.org/10.1016/0379-6779(94)03068-H. URL: https://www.sciencedirect.com/science/article/pii/037967799403068H (cit. on p. 13).

[50] F. L. Pratt, S. J. Blundell, T. Lancaster, C. Baines, and S. Takagi. "Low-Temperature Spin Diffusion in a Highly Ideal $S = \frac{1}{2}$ Heisenberg Antiferromagnetic Chain Studied by Muon Spin Relaxation". In: *Phys. Rev. Lett.* 96 (24 2006), 247203. DOI: 10.1103/PhysRevLett.96.247203. URL: https://link.aps.org/doi/10.1103/PhysRevLett.96.247203 (cit. on p. 13).

[51] Jun Sugiyama, Kazuhiko Mukai, Yutaka Ikedo, Hiroshi Nozaki, Martin Månsson, and Isao Watanabe. "Li Diffusion in Li_xCoO_2 Probed by Muon-Spin Spectroscopy". In: *Phys. Rev. Lett.* 103 (14 2009), 147601. DOI: 10.1103/PhysRevLett.103.147601. URL: https://link.aps.org/doi/10.1103/PhysRevLett.103.147601 (cit. on p. 13).

[52] Isao Watanabe, Nobuo Wada, Hideo Yano, Tsuneyuki Okuno, Kunio Awaga, Seiko Ohira, Kusuo Nishiyama, and Kanetada Nagamine. "Muon-spin-relaxation study of the ground state of the two-dimensional $S = 1$ kagoméantiferromagnet [2-(3-N-methyl-pyridium)-4,4,5,5-tetramethyl-4,5-dihydro-1H-imidazol-1-oxyl 3-N-oxide]BF_4". In: *Phys. Rev. B* 58 (5 1998), 2438–2441. DOI: 10.1103/PhysRevB.58.2438. URL: https://link.aps.org/doi/10.1103/PhysRevB.58.2438 (cit. on p. 13).

[53] K. Ishida, K. Nagamine, T. Matsuzaki, Y. Kuno, T. Yamazaki, E. Torikai, H. Shirakawa, and J. H. Brewer. "Diffusion Properties of the Muon-Produced Soliton in trans-Polyacetylene". In: *Phys. Rev. Lett.* 55 (19 1985), 2009–2012. DOI: 10.1103/PhysRevLett.55.2009. URL: https://link.aps.org/doi/10.1103/PhysRevLett.55.2009 (cit. on p. 13).

[54] K. Nagamine, K. Ishida, T. Matsuzaki, K. Nishiyama, Y. Kuno, T. Yamazaki, and H. Shirakawa. "Solitons in Polyacetylene Produced and Probed by Positive Muons". In: *Phys. Rev. Lett.* 53 (18 1984), 1763–1766. DOI: 10.1103/PhysRevLett.53.1763. URL: https://link.aps.org/doi/10.1103/PhysRevLett.53.1763 (cit. on p. 13).

[55] R. Kadono, J. Imazato, T. Matsuzaki, K. Nishiyama, K. Nagamine, T. Yamazaki, D. Richter, and J.-M. Welter. "Quantum diffusion of positive muons in copper". In: *Phys. Rev. B* 39 (1 1989), 23–41. DOI: 10.1103/PhysRevB.39.23. URL: https://link.aps.org/doi/10.1103/PhysRevB.39.23 (cit. on pp. 13, 38).

[56] A. Abragam. Oxford: Oxford University Press, 1961 (cit. on p. 13).

[57] G Allodi and R De Renzi. "A numerical method to calculate the muon relaxation function in the presence of diffusion". In: *Physica Scripta* 89.11 (2014), 115201. DOI: 10.1088/0031-8949/89/11/115201. URL: https://doi.org/10.1088/0031-8949/89/11/115201 (cit. on p. 13).

[58] M. Born and R. Oppenheimer. "Zur Quantentheorie der Molekeln". In: *Annalen der Physik* 389.20 (1927), 457–484. DOI: https://doi.org/10.1002/andp.19273892002. eprint: https://onlinelibrary.wiley.com/doi/pdf/10.1002/andp.19273892002. URL: https://onlinelibrary.wiley.com/doi/abs/10.1002/andp.19273892002 (cit. on p. 17).

[59] Egil A. Hylleraas. "The Schrödinger Two-Electron Atomic Problem". In: ed. by Per-Olov Löwdin. Vol. 1. Advances in Quantum Chemistry. Academic Press, 1964, pp. 1–33. DOI: https://doi.org/10.1016/S0065-3276(08)60373-1. URL: https://www.sciencedirect.com/science/article/pii/S0065327608603731 (cit. on p. 17).

[60] Hubert M. James and Albert Sprague Coolidge. "The Ground State of the Hydrogen Molecule". In: *The Journal of Chemical Physics* 1.12 (1933), 825–835. DOI: 10.1063/1.1749252. eprint: https://doi.org/10.1063/1.1749252. URL: https://doi.org/10.1063/1.1749252 (cit. on p. 17).

[61] L. H. Thomas. "The calculation of atomic fields". In: *Mathematical Proceedings of the Cambridge Philosophical Society* 23.5 (1927), 542–548. DOI: 10.1017/S0305004100011683 (cit. on p. 18).

[62] P. Hohenberg and W. Kohn. "Inhomogeneous Electron Gas". In: *Phys. Rev.* 136 (3B 1964), B864–B871. DOI: 10.1103/PhysRev.136.B864. URL: https://link.aps.org/doi/10.1103/PhysRev.136.B864 (cit. on pp. 18, 20, 54).

[63] W. Kohn and L. J. Sham. "Self-Consistent Equations Including Exchange and Correlation Effects". In: *Phys. Rev.* 140 (4A 1965), A1133–A1138. DOI: 10.1103/PhysRev.140.A1133. URL: https://link.aps.org/doi/10.1103/PhysRev.140.A1133 (cit. on pp. 18, 20, 54).

[64] D. M. Ceperley and B. J. Alder. "Ground State of the Electron Gas by a Stochastic Method". In: *Phys. Rev. Lett.* 45 (7 1980), 566–569. DOI: 10.1103/PhysRevLett.45.566. URL: https://link.aps.org/doi/10.1103/PhysRevLett.45.566 (cit. on p. 22).

[65] John P. Perdew, Kieron Burke, and Matthias Ernzerhof. "Generalized Gradient Approximation Made Simple". In: *Phys. Rev. Lett.* 77 (18 1996), 3865–3868. DOI: 10.1103/PhysRevLett.77.3865. URL: https://link.aps.org/doi/10.1103/PhysRevLett.77.3865 (cit. on pp. 23, 56).

[66] John P. Perdew and Yue Wang. "Accurate and simple analytic representation of the electron-gas correlation energy". In: *Phys. Rev. B* 45 (23 1992), 13244–13249. DOI: 10.1103/PhysRevB.45.13244. URL: https://link.aps.org/doi/10.1103/PhysRevB.45.13244 (cit. on p. 23).

[67] Hendrik J. Monkhorst and James D. Pack. “Special points for Brillouin-zone integrations”. In: *Phys. Rev. B* 13 (12 1976), 5188–5192. DOI: 10.1103/PhysRevB.13.5188. URL: https://link.aps.org/doi/10.1103/PhysRevB.13.5188 (cit. on pp. 24, 47, 73).

[68] A. Baldereschi. “Mean-Value Point in the Brillouin Zone”. In: *Phys. Rev. B* 7 (12 1973), 5212–5215. DOI: 10.1103/PhysRevB.7.5212. URL: https://link.aps.org/doi/10.1103/PhysRevB.7.5212 (cit. on p. 24).

[69] Conyers Herring. “A New Method for Calculating Wave Functions in Crystals”. In: *Phys. Rev.* 57 (12 1940), 1169–1177. DOI: 10.1103/PhysRev.57.1169. URL: https://link.aps.org/doi/10.1103/PhysRev.57.1169 (cit. on p. 24).

[70] James C. Phillips and Leonard Kleinman. “New Method for Calculating Wave Functions in Crystals and Molecules”. In: *Phys. Rev.* 116 (2 1959), 287–294. DOI: 10.1103/PhysRev.116.287. URL: https://link.aps.org/doi/10.1103/PhysRev.116.287 (cit. on p. 24).

[71] D. R. Hamann, M. Schlüter, and C. Chiang. “Norm-Conserving Pseudopotentials”. In: *Phys. Rev. Lett.* 43 (20 1979), 1494–1497. DOI: 10.1103/PhysRevLett.43.1494. URL: https://link.aps.org/doi/10.1103/PhysRevLett.43.1494 (cit. on p. 25).

[72] G. B. Bachelet, D. R. Hamann, and M. Schlüter. “Pseudopotentials that work: From H to Pu”. In: *Phys. Rev. B* 26 (8 1982), 4199–4228. DOI: 10.1103/PhysRevB.26.4199. URL: https://link.aps.org/doi/10.1103/PhysRevB.26.4199 (cit. on p. 25).

[73] David Vanderbilt. “Soft self-consistent pseudopotentials in a generalized eigenvalue formalism”. In: *Phys. Rev. B* 41 (11 1990), 7892–7895. DOI: 10.1103/PhysRevB.41.7892. URL: https://link.aps.org/doi/10.1103/PhysRevB.41.7892 (cit. on p. 25).

[74] Peter E. Blöchl. “Generalized separable potentials for electronic-structure calculations”. In: *Phys. Rev. B* 41 (8 1990), 5414–5416. DOI: 10.1103/PhysRevB.41.5414. URL: https://link.aps.org/doi/10.1103/PhysRevB.41.5414 (cit. on p. 25).

[75] P. E. Blöchl. “Projector augmented-wave method”. In: *Phys. Rev. B* 50 (24 1994), 17953–17979. DOI: 10.1103/PhysRevB.50.17953. URL: https://link.aps.org/doi/10.1103/PhysRevB.50.17953 (cit. on pp. 25, 47, 73).

[76] G. Kresse and D. Joubert. “From ultrasoft pseudopotentials to the projector augmented-wave method”. In: *Phys. Rev. B* 59 (3 1999), 1758–1775. DOI: 10.1103/PhysRevB.59.1758. URL: https://link.aps.org/doi/10.1103/PhysRevB.59.1758 (cit. on p. 25).

[77] A. Filippetti, David Vanderbilt, W. Zhong, Yong Cai, and G. B. Bachelet. "Chemical hardness, linear response, and pseudopotential transferability". In: *Phys. Rev. B* 52 (16 1995), 11793–11804. DOI: 10.1103/PhysRevB.52.11793. URL: https://link.aps.org/doi/10.1103/PhysRevB.52.11793 (cit. on p. 25).

[78] S. Goedecker and K. Maschke. "Transferability of pseudopotentials". In: *Phys. Rev. A* 45 (1 1992), 88–93. DOI: 10.1103/PhysRevA.45.88. URL: https://link.aps.org/doi/10.1103/PhysRevA.45.88 (cit. on p. 25).

[79] R. P. Feynman. "Forces in Molecules". In: *Phys. Rev.* 56 (4 1939), 340–343. DOI: 10.1103/PhysRev.56.340. URL: https://link.aps.org/doi/10.1103/PhysRev.56.340 (cit. on p. 25).

[80] Bernd G. Pfrommer, Michel Côté, Steven G. Louie, and Marvin L. Cohen. "Relaxation of Crystals with the Quasi-Newton Method". In: *Journal of Computational Physics* 131.1 (1997), 233–240. DOI: https://doi.org/10.1006/jcph.1996.5612. URL: https://www.sciencedirect.com/science/article/pii/S0021999196956120 (cit. on p. 26).

[81] C.K. Gan, P.D. Haynes, and M.C. Payne. "Preconditioned conjugate gradient method for the sparse generalized eigenvalue problem in electronic structure calculations". In: *Computer Physics Communications* 134.1 (2001), 33–40. DOI: https://doi.org/10.1016/S0010-4655(00)00188-0. URL: https://www.sciencedirect.com/science/article/pii/S0010465500001880 (cit. on p. 26).

[82] Paolo Giannozzi, Stefano Baroni, Nicola Bonini, Matteo Calandra, Roberto Car, Carlo Cavazzoni, Davide Ceresoli, Guido L Chiarotti, Matteo Cococcioni, et al. "QUANTUM ESPRESSO: a modular and open-source software project for quantum simulations of materials". In: *Journal of Physics: Condensed Matter* 21.39 (2009), 395502. DOI: 10.1088/0953-8984/21/39/395502. URL: https://doi.org/10.1088%2F0953-8984%2F21%2F39%2F395502 (cit. on pp. 26, 73).

[83] P Giannozzi, O Andreussi, T Brumme, O Bunau, M Buongiorno Nardelli, M Calandra, R Car, C Cavazzoni, D Ceresoli, M Cococcioni, and et al. "Advanced capabilities for materials modelling with Quantum ESPRESSO". In: *Journal of Physics: Condensed Matter* 29.46 (2017), 465901. DOI: 10.1088/1361-648x/aa8f79. URL: http://dx.doi.org/10.1088/1361-648X/aa8f79 (cit. on pp. 26, 73).

[84] Paolo Giannozzi, Oscar Baseggio, Pietro Bonfà, Davide Brunato, Roberto Car, Ivan Carnimeo, Carlo Cavazzoni, Stefano de Gironcoli, Pietro Delugas, et al. "Quantum ESPRESSO toward the exascale". In: *The Journal of Chemical Physics* 152.15 (2020), 154105. DOI: 10.1063/5.0005082. URL: https://doi.org/10.1063/5.0005082 (cit. on p. 26).

[85] H. Maeter, H. Luetkens, Yu. G. Pashkevich, A. Kwadrin, R. Khasanov, A. Amato, A. A. Gusev, K. V. Lamonova, D. A. Chervinskii, et al. “Interplay of rare earth and iron magnetism in RFeAsO (R = La, Ce, Pr, and Sm): Muon-spin relaxation study and symmetry analysis”. In: *Phys. Rev. B* 80 (9 2009), 094524. DOI: 10.1103/PhysRevB.80.094524. URL: https://link.aps.org/doi/10.1103/PhysRevB.80.094524 (cit. on p. 26).

[86] Roberto De Renzi, Pietro Bonfà, Marcello Mazzani, Samuele Sanna, Giacomo Prando, Pietro Carretta, Rustem Khasanov, Alex Amato, Hubertus Luetkens, et al. “Effect of external pressure on the magnetic properties of LnFeAsO (Ln = La, Ce, Pr, Sm)”. In: *Superconductor Science and Technology* 25.8 (2012), 084009. DOI: 10.1088/0953-2048/25/8/084009. URL: https://doi.org/10.1088/0953-2048/25/8/084009 (cit. on pp. 26, 60).

[87] G Lamura, T Shiroka, P Bonfà, S Sanna, F Bernardini, R De Renzi, R Viennois, E Giannini, A Piriou, N Emery, M R Cimberle, and M Putti. “A magnetic glassy phase in $Fe_{1+y}Se_xTe_{1-x}$ single crystals”. In: *Journal of Physics: Condensed Matter* 25.15 (2013), 156004. DOI: 10.1088/0953-8984/25/15/156004. URL: https://doi.org/10.1088/0953-8984/25/15/156004 (cit. on p. 26).

[88] Koichi Momma and Fujio Izumi. “*VESTA*: a three-dimensional visualization system for electronic and structural analysis”. In: *Journal of Applied Crystallography* 41.3 (2008), 653–658. DOI: 10.1107/S0021889808012016. URL: https://doi.org/10.1107/S0021889808012016 (cit. on pp. 26, 27, 77).

[89] Pietro Bonfà, Jonathan Frassineti, Muhammad Maikudi Isah, Ifeanyi John Onuorah, and Samuele Sanna. “UNDI: An open-source library to simulate muon-nuclear interactions in solids”. In: *Computer Physics Communications* 260 (2021), 107719. DOI: https://doi.org/10.1016/j.cpc.2020.107719. URL: https://www.sciencedirect.com/science/article/pii/S0010465520303556 (cit. on pp. 29, 31, 34, 40).

[90] W. Huang, V. Pacradouni, and J.E. Sonier. “Calculation of Nuclear Contribution to the Zero-field Muon Spin Polarization Function of Single Crystal La2-XSrXCuO4”. In: *Physics Procedia* 30 (2012). 12th International Conference on Muon Spin Rotation, Relaxation and Resonance (μSR2011), 129–132. DOI: https://doi.org/10.1016/j.phpro.2012.04.056. URL: https://www.sciencedirect.com/science/article/pii/S1875389212012424 (cit. on pp. 31, 38, 39).

[91] Masuo Suzuki. “Generalized Trotter’s formula and systematic approximants of exponential operators and inner derivations with applications to many-body problems”. In: *Communications in Mathematical Physics* 51.2 (1976), 183–190. DOI: 10.1007/BF01609348. URL: https://doi.org/10.1007/BF01609348 (cit. on p. 31).

[92] J. H. Brewer, S. R. Kreitzman, D. R. Noakes, E. J. Ansaldo, D. R. Harshman, and R. Keitel. "Observation of muon-fluorine "hydrogen bonding" in ionic crystals". In: *Phys. Rev. B* 33 (11 1986), 7813–7816. DOI: 10.1103/PhysRevB.33.7813. URL: https://link.aps.org/doi/10.1103/PhysRevB.33.7813 (cit. on pp. 36, 37).

[93] T. Lancaster, S. J. Blundell, P. J. Baker, M. L. Brooks, W. Hayes, F. L. Pratt, J. L. Manson, M. M. Conner, and J. A. Schlueter. "Muon-Fluorine Entangled States in Molecular Magnets". In: *Phys. Rev. Lett.* 99 (26 2007), 267601. DOI: 10.1103/PhysRevLett.99.267601. URL: https://link.aps.org/doi/10.1103/PhysRevLett.99.267601 (cit. on p. 36).

[94] J. M. Wilkinson and S. J. Blundell. "Information and Decoherence in a Muon-Fluorine Coupled System". In: *Phys. Rev. Lett.* 125 (8 2020), 087201. DOI: 10.1103/PhysRevLett.125.087201. URL: https://link.aps.org/doi/10.1103/PhysRevLett.125.087201 (cit. on pp. 36, 38).

[95] O. Hartmann. "Quadrupole Influence on the Dipolar-Field Width for a Single Interstitial in a Metal Crystal". In: *Phys. Rev. Lett.* 39 (13 1977), 832–835. DOI: 10.1103/PhysRevLett.39.832. URL: https://link.aps.org/doi/10.1103/PhysRevLett.39.832 (cit. on p. 38).

[96] M. Camani, F. N. Gygax, W. Rüegg, A. Schenck, and H. Schilling. "Positive Muons in Copper: Detection of an Electric-Field Gradient at the Neighbor Cu Nuclei and Determination of the Site of Localization". In: *Phys. Rev. Lett.* 39 (13 1977), 836–839. DOI: 10.1103/PhysRevLett.39.836. URL: https://link.aps.org/doi/10.1103/PhysRevLett.39.836 (cit. on pp. 38, 39).

[97] H Schilling, M Camani, F N Gygax, W Ruegg, and A Schenck. "Depolarisation studies of positive muons in copper, vanadium, niobium and tantalum single crystals". In: *Journal of Physics F: Metal Physics* 12.5 (1982), 875–893. DOI: 10.1088/0305-4608/12/5/007. URL: https://doi.org/10.1088/0305-4608/12/5/007 (cit. on p. 38).

[98] PEKKA PYYKKÖ. "Spectroscopic nuclear quadrupole moments". In: *Molecular Physics* 99.19 (2001), 1617–1629. DOI: 10.1080/00268970110069010. eprint: https://doi.org/10.1080/00268970110069010. URL: https://doi.org/10.1080/00268970110069010 (cit. on p. 39).

[99] P. Jena, Shashikala G. Das, and K. S. Singwi. "Electric-Field Gradient at Cu Nuclei Due to an Interstitial Positive Muon". In: *Phys. Rev. Lett.* 40 (4 1978), 264–266. DOI: 10.1103/PhysRevLett.40.264. URL: https://link.aps.org/doi/10.1103/PhysRevLett.40.264 (cit. on p. 40).

[100] A. Amato, P. Dalmas de Réotier, D. Andreica, A. Yaouanc, A. Suter, G. Lapertot, I. M. Pop, E. Morenzoni, P. Bonfà, F. Bernardini, and R. De Renzi. "Understanding the μSR spectra of MnSi without magnetic polarons". In: *Phys. Rev. B* 89 (18 2014), 184425. DOI: 10.1103/PhysRevB.89.184425. URL: https://link.aps.org/doi/10.1103/PhysRevB.89.184425 (cit. on p. 40).

[101] Hiroshi Yasuoka, V. Jaccarino, R. C. Sherwood, and J. H. Wernick. "NMR and Susceptibility Studies of MnSi above Tc". In: *Journal of the Physical Society of Japan* 44.3 (1978), 842–849. DOI: 10.1143/JPSJ.44.842. eprint: https://doi.org/10.1143/JPSJ.44.842. URL: https://doi.org/10.1143/JPSJ.44.842 (cit. on pp. 40, 41).

[102] Pierre Dalmas de Réotier, Alain Yaouanc, Alex Amato, Alexander Maisuradze, Daniel Andreica, Bertrand Roessli, Tatsuo Goko, Robert Scheuermann, and Gérard Lapertot. "On the Robustness of the MnSi Magnetic Structure Determined by Muon Spin Rotation". In: *Quantum Beam Science* 2.3 (2018). DOI: 10.3390/qubs2030019. URL: https://www.mdpi.com/2412-382X/2/3/19 (cit. on p. 40).

[103] R. Kadono, J. H. Brewer, K. Chow, S. R. Kreitzman, Ch. Niedermayer, T. M. Riseman, J. W. Schneider, and T. Yamazaki. "Critical behavior of electric field gradient in MnSi studied by muon level-crossing resonance". In: *Hyperfine Interactions* 85.1 (1994), 259–264. DOI: 10.1007/BF02069431. URL: https://doi.org/10.1007/BF02069431 (cit. on p. 40).

[104] W. Huang, V. Pacradouni, M. P. Kennett, S. Komiya, and J. E. Sonier. "Precision search for magnetic order in the pseudogap regime of $La_{2-x}Sr_xCuO_4$ by muon spin relaxation". In: *Phys. Rev. B* 85 (10 2012), 104527. DOI: 10.1103/PhysRevB.85.104527. URL: https://link.aps.org/doi/10.1103/PhysRevB.85.104527 (cit. on p. 40).

[105] D. W. Alderman, Mark S. Solum, and David M. Grant. "Methods for analyzing spectroscopic line shapes. NMR solid powder patterns". In: *The Journal of Chemical Physics* 84.7 (1986), 3717–3725. DOI: 10.1063/1.450211. eprint: https://doi.org/10.1063/1.450211. URL: https://doi.org/10.1063/1.450211 (cit. on p. 40).

[106] R. Feyerherm, A. Amato, F.N. Gygax, A. Schenck, Y. Ōnuki, and N. Sato. "Problems of the magnetic structure of CeB6". In: *Journal of Magnetism and Magnetic Materials* 140-144 (1995). International Conference on Magnetism, 1175–1176. DOI: https://doi.org/10.1016/0304-8853(94)01281-4. URL: https://www.sciencedirect.com/science/article/pii/0304885394012814 (cit. on p. 41).

[107] R. Hussain, F. Cugini, S. Baldini, G. Porcari, N. Sarzi Amadè, X. F. Miao, N. H. van Dijk, E. Brück, M. Solzi, R. De Renzi, and G. Allodi. "Ubiquitous first-order transitions and site-selective vanishing of the magnetic moment in giant magnetocaloric MnFeSiP alloys detected by ^{55}Mn NMR". In: *Phys. Rev. B* 100 (10 2019), 104439. DOI: 10.1103/PhysRevB.100.104439. URL: https://link.aps.org/doi/10.1103/PhysRevB.100.104439 (cit. on p. 43).

[108] F. Guillou, Sun-Liting, O. Haschuluu, Z.Q. Ou, E. Brück, O. Tegus, and H. Yibole. "Room temperature magnetic anisotropy in Fe2P-type transition metal based alloys". In: *Journal of Alloys and Compounds* 800 (2019), 403–411. DOI: https://doi.org/10.1016/j.jallcom.2019.05.327. URL: http://www.sciencedirect.com/science/article/pii/S0925838819320183 (cit. on p. 43).

[109] François Guillou, Giacomo Porcari, Hargen Yibole, Niels van Dijk, and Ekkes Brück. "Taming the First-Order Transition in Giant Magnetocaloric Materials". In: *Advanced Materials* 26.17 (2014), 2671–2675. DOI: 10.1002/adma.201304788. URL: https://onlinelibrary.wiley.com/doi/abs/10.1002/adma.201304788 (cit. on p. 43).

[110] Andrej Kitanovski. "Energy Applications of Magnetocaloric Materials". In: *Advanced Energy Materials* 10.10 (2020), 1903741. DOI: https://doi.org/10.1002/aenm.201903741. eprint: https://onlinelibrary.wiley.com/doi/pdf/10.1002/aenm.201903741. URL: https://onlinelibrary.wiley.com/doi/abs/10.1002/aenm.201903741 (cit. on p. 43).

[111] Daniel Dzekan, Anja Waske, Kornelius Nielsch, and Sebastian Fähler. "Efficient and affordable thermomagnetic materials for harvesting low grade waste heat". In: *APL Materials* 9.1 (2021), 011105. DOI: 10.1063/5.0033970. eprint: https://doi.org/10.1063/5.0033970. URL: https://doi.org/10.1063/5.0033970 (cit. on p. 43).

[112] Ekkes Brück. "Developments in magnetocaloric refrigeration". In: *Journal of Physics D: Applied Physics* 38.23 (2005), R381–R391. DOI: 10.1088/0022-3727/38/23/r01. URL: https://doi.org/10.1088/0022-3727/38/23/r01 (cit. on p. 43).

[113] N. T. Trung, L. Zhang, L. Caron, K. H. J. Buschow, and E. Brück. "Giant magnetocaloric effects by tailoring the phase transitions". In: *Applied Physics Letters* 96.17 (2010), 172504. DOI: 10.1063/1.3399773. eprint: https://doi.org/10.1063/1.3399773. URL: https://doi.org/10.1063/1.3399773 (cit. on p. 43).

[114] Nguyen H. Dung, Zhi Qiang Ou, Luana Caron, Lian Zhang, Dinh T. Cam Thanh, Gilles A. de Wijs, Rob A. de Groot, K. H. Jürgen Buschow, and Ekkes Brück. "Mixed Magnetism for Refrigeration and Energy Conversion". In: *Advanced Energy Materials* 1.6 (2011), 1215–1219. DOI: https://doi.org/10.1002/aenm.201100252. eprint: https://onlinelibrary.wiley.com/doi/pdf/10.1002/aenm.201100252. URL: https://onlinelibrary.wiley.com/doi/abs/10.1002/aenm.201100252 (cit. on p. 43).

[115] O. Tegus, E. Brück, K. Buschow, and F. R. de Boer. "Transition-metal-based magnetic refrigerants for room-temperature applications." In: *Nature Material* 415 (2002), 150–152. DOI: 10.1038/415150a. URL: https://doi.org/10.1038/415150a (cit. on p. 43).

[116] R. Wäppling, L. Häggström, T. Ericsson, S. Devanarayanan, E. Karlsson, B. Carlsson, and S. Rundqvist. "First order magnetic transition, magnetic structure, and vacancy distribution in Fe2P". In: *Journal of Solid State Chemistry* 13.3 (1975), 258 –271. DOI: https://doi.org/10.1016/0022-4596(75)90128-0. URL: http://www.sciencedirect.com/science/article/pii/0022459675901280 (cit. on pp. 43–45).

[117] L. Caron, M. Hudl, V. Höglin, N. H. Dung, C. P. Gomez, M. Sahlberg, E. Brück, Y. Andersson, and P. Nordblad. "Magnetocrystalline anisotropy and the magnetocaloric effect in Fe_2P". In: *Phys. Rev. B* 88 (9 2013), 094440. DOI: 10.1103/PhysRevB.88.094440. URL: https://link.aps.org/doi/10.1103/PhysRevB.88.094440 (cit. on p. 43).

[118] I. A. Zhuravlev, V. P. Antropov, A. Vishina, M. van Schilfgaarde, and K. D. Belashchenko. "Tunable dimensional crossover and magnetocrystalline anisotropy in Fe2P-based alloys". In: *Phys. Rev. Materials* 1 (5 2017), 051401. DOI: 10.1103/PhysRevMaterials.1.051401. URL: https://link.aps.org/doi/10.1103/PhysRevMaterials.1.051401 (cit. on pp. 43, 44).

[119] Bertil Carlsson, Margareta Gölin, and Stig Rundqvist. "Determination of the homogeneity range and refinement of the crystal structure of Fe2P". In: *Journal of Solid State Chemistry* 8.1 (1973), 57 –67. DOI: https://doi.org/10.1016/0022-4596(73)90021-2. URL: http://www.sciencedirect.com/science/article/pii/0022459673900212 (cit. on pp. 44, 47).

[120] D. Scheerlinck and E. Legrand. "Neutron diffraction study of the magnetic structure of Fe2P". In: *Solid State Communications* 25.3 (Jan. 1978), 181–184. DOI: 10.1016/0038-1098(78)91474-6. URL: https://doi.org/10.1016/0038-1098(78)91474-6 (cit. on pp. 44, 47).

[121] Hironobu Fujii, Shigehiro Komura, Takayoshi Takeda, Tetsuhiko Okamoto, Yuji Ito, and Jun Akimitsu. "Polarized Neutron Diffraction Study of Fe2P Single Crystal". In: *Journal of the Physical Society of Japan* 46.5 (May 1979), 1616–1621. DOI: 10.1143/jpsj.46.1616. URL: https://doi.org/10.1143/jpsj.46.1616 (cit. on p. 44).

[122] J. Tobola, M. Bacmann, D. Fruchart, S. Kaprzyk, A. Koumina, S. Niziol, J.-L. Soubeyroux, P. Wolfers, and R. Zach. "Magnetism of Fe2P investigated by neutron experiments and band structure calculations". In: *Journal of Magnetism and Magnetic Materials* 157-158 (May 1996), 708–710. DOI: 10.1016/0304-8853(95)01258-3. URL: https://doi.org/10.1016/0304-8853(95)01258-3 (cit. on pp. 44, 47).

[123] A Koumina, M Bacmann, D Fruchart, J Soubeyroux, P Wolfers, J Tobola, S Kaprzyk, S Niziol, M Mesnaoui, and R Zach. "Crystallographic and magnetic properties of fep". In: *Annales de Chimie Science des Materiaux* 23.1-2 (Jan. 1998), 177–180. DOI: 10.1016/s0151-9107(98)80050-0. URL: https://doi.org/10.1016/s0151-9107(98)80050-0 (cit. on pp. 44, 47).

[124] Hironobu Fujii, Yoshiya Uwatoko, Kiyoichiro Motoya, Yuji Ito, and Tetsuhiko Okamoto. "Neutron Scattering Investigation of Itinerant Electron System Fe2P". In: *Journal of the Physical Society of Japan* 57.6 (1988), 2143–2153. DOI: 10.1143/JPSJ.57.2143. eprint: https://doi.org/10.1143/JPSJ.57.2143. URL: https://doi.org/10.1143/JPSJ.57.2143 (cit. on p. 44).

[125] X. F. Miao, L. Caron, J. Cedervall, P. C. M. Gubbens, P. Dalmas de Réotier, A. Yaouanc, F. Qian, A. R. Wildes, H. Luetkens, A. Amato, N. H. van Dijk, and E. Brück. "Short-range magnetic correlations and spin dynamics in the paramagnetic regime of $(Mn,Fe)_2(P,Si)$". In: *Phys. Rev. B* 94 (1 2016), 014426. DOI: 10.1103/PhysRevB.94.014426. URL: https://link.aps.org/doi/10.1103/PhysRevB.94.014426 (cit. on p. 44).

[126] N. H. Dung, L. Zhang, Z. Q. Ou, L. Zhao, L. van Eijck, A. M. Mulders, M. Avdeev, E. Suard, N. H. van Dijk, and Ekkes Brück. "High/low-moment phase transition in hexagonal Mn-Fe-P-Si compounds". In: *Phys. Rev. B* 86 (4 2012), 045134. DOI: 10.1103/PhysRevB.86.045134. URL: https://link.aps.org/doi/10.1103/PhysRevB.86.045134 (cit. on p. 44).

[127] G. Allodi, A. Banderini, R. De Renzi, and C. Vignali. "HyReSpect: A broadband fast-averaging spectrometer for nuclear magnetic resonance of magnetic materials". In: *Review of Scientific Instruments* 76.8 (Aug. 2005), 083911. DOI: 10.1063/1.2009868. URL: https://doi.org/10.1063/1.2009868 (cit. on p. 44).

[128] G Allodi, R De Renzi, K Zheng, S Sanna, A Sidorenko, C Baumann, L Righi, F Orlandi, and G Calestani. "Band filling effect on polaron localization in La1-x(CaySr1-y)xMnO3manganites". In: *Journal of Physics: Condensed Matter* 26.26 (June 2014), 266004. DOI: 10.1088/0953-8984/26/26/266004. URL: https://doi.org/10.1088/0953-8984/26/26/266004 (cit. on p. 44).

[129] E. Koster and B. G. Turrell. "NMR Studies of Fe2P and Fe3P". In: *Journal of Applied Physics* 42.4 (1971), 1314–1315. DOI: 10.1063/1.1660234. URL: https://doi.org/10.1063/1.1660234 (cit. on p. 44).

[130] J. Cedervall, M. S. Andersson, E. K. Delczeg-Czirjakan, familyi=c., given=D., giveni=D., „ M. Pereiro, P. Roy, T. Ericsson, L. Häggström, W. Lohstroh, et al. "Magnetocaloric effect in Fe_2P: Magnetic and phonon degrees of freedom". In: *Phys. Rev. B* 99 (17 2019), 174437. DOI: 10.1103/PhysRevB.99.174437. URL: https://link.aps.org/doi/10.1103/PhysRevB.99.174437 (cit. on pp. 45, 46).

[131] Paolo Giannozzi, Stefano Baroni, Nicola Bonini, Matteo Calandra, Roberto Car, Carlo Cavazzoni, Davide Ceresoli, Guido L Chiarotti, Matteo Cococcioni, et al. "QUANTUM ESPRESSO: a modular and open-source software project for quantum simulations of materials". In: *Journal of Physics: Condensed Matter* 21.39 (2009), 395502. DOI: 10.1088/0953-8984/21/39/395502. URL: https://doi.org/10.1088/0953-8984/21/39/395502 (cit. on pp. 47, 55).

[132] P Giannozzi, O Andreussi, T Brumme, O Bunau, M Buongiorno Nardelli, M Calandra, R Car, C Cavazzoni, D Ceresoli, M Cococcioni, and et al. "Advanced capabilities for materials modelling with Quantum ESPRESSO". In: *Journal of Physics: Condensed Matter* 29.46 (2017), 465901. DOI: 10.

1088/1361-648x/aa8f79. URL: http://dx.doi.org/10.1088/1361-648X/aa8f79 (cit. on pp. 47, 55).

[133] Paolo Giannozzi, Oscar Baseggio, Pietro Bonfà, Davide Brunato, Roberto Car, Ivan Carnimeo, Carlo Cavazzoni, Stefano de Gironcoli, Pietro Delugas, et al. "Quantum ESPRESSO toward the exascale". In: *The Journal of Chemical Physics* 152.15 (2020), 154105. DOI: 10.1063/5.0005082. eprint: https://doi.org/10.1063/5.0005082. URL: https://doi.org/10.1063/5.0005082 (cit. on pp. 47, 55).

[134] John P. Perdew, Kieron Burke, and Matthias Ernzerhof. "Generalized Gradient Approximation Made Simple". In: *Phys. Rev. Lett.* 77 (18 1996), 3865–3868. DOI: 10.1103/PhysRevLett.77.3865. URL: https://link.aps.org/doi/10.1103/PhysRevLett.77.3865 (cit. on pp. 47, 73).

[135] Nicola Marzari, David Vanderbilt, Alessandro De Vita, and M. C. Payne. "Thermal Contraction and Disordering of the Al(110) Surface". In: *Phys. Rev. Lett.* 82 (16 1999), 3296–3299. DOI: 10.1103/PhysRevLett.82.3296. URL: https://link.aps.org/doi/10.1103/PhysRevLett.82.3296 (cit. on pp. 47, 73).

[136] J.P. Senateur, A. Rouault, R. Fruchart, J.J. Capponi, and M. Perroux. "Etude par spectrometrie Mossbauer des transformations cristallographiques sous hautes pressions de MnFeAs et Fe2P". In: *Materials Research Bulletin* 11.6 (1976), 631 –635. DOI: https://doi.org/10.1016/0025-5408(76)90137-9. URL: http://www.sciencedirect.com/science/article/pii/0025540876901379 (cit. on p. 47).

[137] S Ishida, S Asano, and J Ishida. "Electronic structures and magnetic properties of T2P (T=Mn, Fe, Ni)". In: *Journal of Physics F: Metal Physics* 17.2 (1987), 475–482. DOI: 10.1088/0305-4608/17/2/016. URL: https://doi.org/10.1088%2F0305-4608%2F17%2F2%2F016 (cit. on p. 47).

[138] Soumya S Bhat, Kapil Gupta, Satadeep Bhattacharjee, and Seung-Cheol Lee. "Role of zero-point effects in stabilizing the ground state structure of bulk Fe2P". In: *Journal of Physics: Condensed Matter* 30.21 (2018), 215401. DOI: 10.1088/1361-648x/aabe52. URL: http://dx.doi.org/10.1088/1361-648X/aabe52 (cit. on p. 47).

[139] Ifeanyi John Onuorah, Pietro Bonfà, Roberto De Renzi, Lorenzo Monacelli, Francesco Mauri, Matteo Calandra, and Ion Errea. "Quantum effects in muon spin spectroscopy within the stochastic self-consistent harmonic approximation". In: *Phys. Rev. Materials* 3 (7 2019), 073804. DOI: 10.1103/PhysRevMaterials.3.073804. URL: https://link.aps.org/doi/10.1103/PhysRevMaterials.3.073804 (cit. on pp. 47, 49, 58, 68).

[140] Peter Blaha, Karlheinz Schwarz, Georg K H Madsen, Dieter Kvasnicka, Joachim Luitz, Robert Laskowsk, Fabien Tran, Laurence Marks, and Laurence Marks. *WIEN2k: An Augmented Plane Wave Plus Local Orbitals Program for Calculating Crystal Properties*. English (US). Techn. Universitat, 2019. URL: http://susi.theochem.tuwien.ac.at/reg_user/textbooks/usersguide.pdf (cit. on p. 50).

[141] K Dewhurst, S Sharma, L Nordstrom, F Cricchio, O Grånäs, H Gross, C Ambrosch-Draxl, C Persson, F Bultmark, and C Brouder. *The Elk Code, version 6.8.21*. 2019. URL: http://elk.sourceforge.net/ (visited on 01/30/2020) (cit. on p. 50).

[142] S. Blügel, H. Akai, R. Zeller, and P. H. Dederichs. "Hyperfine fields of 3d and 4d impurities in nickel". In: *Phys. Rev. B* 35 (7 1987), 3271–3283. DOI: 10.1103/PhysRevB.35.3271. URL: https://link.aps.org/doi/10.1103/PhysRevB.35.3271 (cit. on p. 50).

[143] P. Bonfà, F. Sartori, and R. De Renzi. "Efficient and Reliable Strategy for Identifying Muon Sites Based on the Double Adiabatic Approximation". In: *The Journal of Physical Chemistry C* 119.8 (2015), 4278–4285. DOI: 10.1021/jp5125876. eprint: https://doi.org/10.1021/jp5125876. URL: https://doi.org/10.1021/jp5125876 (cit. on p. 52).

[144] Pietro Bonfà, Muhammad Maikudi Isah, Benjamin A. Frandsen, Ethan J. Gibson, Ekkes Brück, Ifeanyi John Onuorah, Roberto De Renzi, and Giuseppe Allodi. "Ab initio modeling and experimental investigation of Fe_2P by DFT and spin spectroscopies". In: *Phys. Rev. Materials* 5 (4 2021), 044411. DOI: 10.1103/PhysRevMaterials.5.044411. URL: https://link.aps.org/doi/10.1103/PhysRevMaterials.5.044411 (cit. on p. 52).

[145] Parker Liu, Bingkun Guo, Tanglin An, Hui Fang, Genxiang Zhu, Chris Jiang, and Xiaoping Jiang. "High throughput materials research and development for lithium ion batteries". In: *Journal of Materiomics* 3.3 (2017). High-throughput Experimental and Modeling Research toward Advanced Batteries, 202–208. DOI: https://doi.org/10.1016/j.jmat.2017.07.004. URL: https://www.sciencedirect.com/science/article/pii/S2352847817300527 (cit. on p. 53).

[146] Shoichi Matsuda, Kiho Nishioka, and Shuji Nakanishi. "High-throughput combinatorial screening of multi-component electrolyte additives to improve the performance of Li metal secondary batteries". In: *Scientific Reports* 9.1 (2019), 6211. DOI: 10.1038/s41598-019-42766-x. URL: https://doi.org/10.1038/s41598-019-42766-x (cit. on p. 53).

[147] Leonid Kahle, Aris Marcolongo, and Nicola Marzari. "High-throughput computational screening for solid-state Li-ion conductors". In: *Energy Environ. Sci.* 13 (3 2020), 928–948. DOI: 10.1039/C9EE02457C. URL: http://dx.doi.org/10.1039/C9EE02457C (cit. on p. 53).

[148] Xinru Li, Zeying Zhang, Yugui Yao, and Hongbin Zhang. "High throughput screening for two-dimensional topological insulators". In: *2D Materials* 5.4 (2018), 045023. DOI: 10.1088/2053-1583/aadb1e. URL: https://doi.org/10.1088/2053-1583/aadb1e (cit. on p. 53).

[149] Yuanfeng Xu, Luis Elcoro, Zhi-Da Song, Benjamin J. Wieder, M. G. Vergniory, Nicolas Regnault, Yulin Chen, Claudia Felser, and B. Andrei Bernevig. "High-throughput calculations of magnetic topological materials". In: *Nature* 586.7831 (2020), 702–707. DOI: 10.1038/s41586-020-2837-0. URL: https://doi.org/10.1038/s41586-020-2837-0 (cit. on p. 53).

[150] Nathan C. Frey, Matthew K. Horton, Jason M. Munro, Sinéad M. Griffin, Kristin A. Persson, and Vivek B. Shenoy. "High-throughput search for magnetic and topological order in transition metal oxides". In: *Science Advances* 6.50 (2020). DOI: 10.1126/sciadv.abd1076. eprint: https://advances.sciencemag.org/content/6/50/eabd1076.full.pdf. URL: https://advances.sciencemag.org/content/6/50/eabd1076 (cit. on p. 53).

[151] Ruoxi Xia, Christoph J. Brabec, Hin-Lap Yip, and Yong Cao. "High-Throughput Optical Screening for Efficient Semitransparent Organic Solar Cells". In: *Joule* 3.9 (2019), 2241–2254. DOI: https://doi.org/10.1016/j.joule.2019.06.016. URL: https://www.sciencedirect.com/science/article/pii/S2542435119303071 (cit. on p. 53).

[152] Yamil J. Colón, David Fairen-Jimenez, Christopher E. Wilmer, and Randall Q. Snurr. "High-Throughput Screening of Porous Crystalline Materials for Hydrogen Storage Capacity near Room Temperature". In: *The Journal of Physical Chemistry C* 118.10 (2014), 5383–5389. DOI: 10.1021/jp4122326. eprint: https://doi.org/10.1021/jp4122326. URL: https://doi.org/10.1021/jp4122326 (cit. on p. 53).

[153] N. Scott Bobbitt, Jiayi Chen, and Randall Q. Snurr. "High-Throughput Screening of Metal–Organic Frameworks for Hydrogen Storage at Cryogenic Temperature". In: *The Journal of Physical Chemistry C* 120.48 (2016), 27328–27341. DOI: 10.1021/acs.jpcc.6b08729. eprint: https://doi.org/10.1021/acs.jpcc.6b08729. URL: https://doi.org/10.1021/acs.jpcc.6b08729 (cit. on p. 53).

[154] Kenji Sumida, Satoshi Horike, Steven S. Kaye, Zoey R. Herm, Wendy L. Queen, Craig M. Brown, Fernande Grandjean, Gary J. Long, Anne Dailly, and Jeffrey R. Long. "Hydrogen storage and carbon dioxide capture in an iron-based sodalite-type metal–organic framework (Fe-BTT) discovered via high-throughput methods". In: *Chem. Sci.* 1 (2 2010), 184–191. DOI: 10.1039/C0SC00179A. URL: http://dx.doi.org/10.1039/C0SC00179A (cit. on p. 53).

[155] Giovanni Pizzi, Andrea Cepellotti, Riccardo Sabatini, Nicola Marzari, and Boris Kozinsky. "AiiDA: automated interactive infrastructure and database for computational science". In: *Computational Materials Science* 111 (2016), 218 –230. DOI: https://doi.org/10.1016/j.commatsci.

2015.09.013. URL: http://www.sciencedirect.com/science/article/pii/S0927025615005820 (cit. on pp. 53, 56).

[156] *The AiiDA plugin registry*. https://aiidateam.github.io/aiida-registry/ (cit. on pp. 53, 56).

[157] J.M. Perez-Mato, S.V. Gallego, E.S. Tasci, L. Elcoro, G. de la Flor, and M.I. Aroyo. "Symmetry-Based Computational Tools for Magnetic Crystallography". In: *Annual Review of Materials Research* 45.1 (2015), 217–248. DOI: 10.1146/annurev-matsci-070214-021008. eprint: https://doi.org/10.1146/annurev-matsci-070214-021008. URL: https://doi.org/10.1146/annurev-matsci-070214-021008 (cit. on pp. 53, 54).

[158] Gemma de la Flor, Bernd Souvignier, Gotzon Madariaga, and Mois I. Aroyo. "Layer groups: Brillouin-zone and crystallographic databases on the Bilbao Crystallographic Server". In: *Acta Crystallographica Section A* 77.6 (2021), 559–571. DOI: 10.1107/S205327332100783X. URL: https://doi.org/10.1107/S205327332100783X (cit. on pp. 53, 54).

[159] Samuel V. Gallego, J. Manuel Perez-Mato, Luis Elcoro, Emre S. Tasci, Robert M. Hanson, Koichi Momma, Mois I. Aroyo, and Gotzon Madariaga. "*MAGNDATA*: towards a database of magnetic structures. I.The commensurate case". In: *Journal of Applied Crystallography* 49.5 (2016), 1750–1776. DOI: 10.1107/S1600576716012863. URL: https://doi.org/10.1107/S1600576716012863 (cit. on pp. 53, 54).

[160] Samuel V. Gallego, J. Manuel Perez-Mato, Luis Elcoro, Emre S. Tasci, Robert M. Hanson, Mois I. Aroyo, and Gotzon Madariaga. "*MAGNDATA*: towards a database of magnetic structures. II. The incommensurate case". In: *Journal of Applied Crystallography* 49.6 (2016), 1941–1956. DOI: 10.1107/S1600576716015491. URL: https://doi.org/10.1107/S1600576716015491 (cit. on pp. 53, 54).

[161] Anubhav Jain, Shyue Ping Ong, Geoffroy Hautier, Wei Chen, William Davidson Richards, Stephen Dacek, Shreyas Cholia, Dan Gunter, David Skinner, Gerbrand Ceder, and Kristin A. Persson. "Commentary: The Materials Project: A materials genome approach to accelerating materials innovation". In: *APL Materials* 1.1 (2013), 011002. DOI: 10.1063/1.4812323. eprint: https://doi.org/10.1063/1.4812323. URL: https://doi.org/10.1063/1.4812323 (cit. on p. 53).

[162] Nicolas Mounet, Marco Gibertini, Philippe Schwaller, Davide Campi, Andrius Merkys, Antimo Marrazzo, Thibault Sohier, Ivano Eligio Castelli, Andrea Cepellotti, Giovanni Pizzi, and Nicola Marzari. "Two-dimensional materials from high-throughput computational exfoliation of experimentally known compounds". In: *Nature Nanotechnology* 13.3 (2018), 246–252. DOI: 10.1038/s41565-017-0035-5. URL: https://doi.org/10.1038/s41565-017-0035-5 (cit. on p. 53).

[163] Matthew Kristofer Horton, Joseph Harold Montoya, Miao Liu, and Kristin Aslaug Persson. "High-throughput prediction of the ground-state collinear magnetic order of inorganic materials using Density Functional Theory". In: *npj Computational Materials* 5.1 (2019), 64. DOI: 10.1038/s41524-019-0199-7. URL: https://doi.org/10.1038/s41524-019-0199-7 (cit. on pp. 53, 54, 70).

[164] Hongbin Zhang. "High-throughput design of magnetic materials". In: *Electronic Structure* 3.3 (2021), 033001. DOI: 10.1088/2516-1075/abbb25. URL: https://doi.org/10.1088/2516-1075/abbb25 (cit. on pp. 53, 54, 70).

[165] Stefano Sanvito, Corey Oses, Junkai Xue, Anurag Tiwari, Mario Zic, Thomas Archer, Pelin Tozman, Munuswamy Venkatesan, Michael Coey, and Stefano Curtarolo. "Accelerated discovery of new magnets in the Heusler alloy family". In: *Science Advances* 3.4 (2017). DOI: 10.1126/sciadv.1602241. eprint: https://advances.sciencemag.org/content/3/4/e1602241.full.pdf. URL: https://advances.sciencemag.org/content/3/4/e1602241 (cit. on p. 54).

[166] Vladan Stevanović, Stephan Lany, Xiuwen Zhang, and Alex Zunger. "Correcting density functional theory for accurate predictions of compound enthalpies of formation: Fitted elemental-phase reference energies". In: *Phys. Rev. B* 85 (11 2012), 115104. DOI: 10.1103/PhysRevB.85.115104. URL: https://link.aps.org/doi/10.1103/PhysRevB.85.115104 (cit. on p. 54).

[167] Kevin F. Garrity, Joseph W. Bennett, Karin M. Rabe, and David Vanderbilt. "Pseudopotentials for high-throughput DFT calculations". In: *Computational Materials Science* 81 (2014), 446–452. DOI: 10.1016/j.commatsci.2013.08.053. URL: http://dx.doi.org/10.1016/j.commatsci.2013.08.053 (cit. on p. 56).

[168] C. L. Fu and K. M. Ho. "First-principles calculation of the equilibrium ground-state properties of transition metals: Applications to Nb and Mo". In: *Phys. Rev. B* 28 (10 1983), 5480–5486. DOI: 10.1103/PhysRevB.28.5480. URL: https://link.aps.org/doi/10.1103/PhysRevB.28.5480 (cit. on p. 56).

[169] Hendrik J. Monkhorst and James D. Pack. "Special points for Brillouin-zone integrations". In: *Phys. Rev. B* 13 (12 1976), 5188–5192. DOI: 10.1103/PhysRevB.13.5188. URL: https://link.aps.org/doi/10.1103/PhysRevB.13.5188 (cit. on p. 56).

[170] N. Qureshi, Y. Drees, J. Werner, S. Wurmehl, C. Hess, R. Klingeler, B. Büchner, M. T. Fernández-Díaz, and M. Braden. "Crystal and magnetic structure of the oxypnictide superconductor $LaFeAsO_{1-x}F_x$: A neutron-diffraction study". In: *Phys. Rev. B* 82 (18 2010), 184521. DOI: 10.1103/PhysRevB.82.184521. URL: https://link.aps.org/doi/10.1103/PhysRevB.82.184521 (cit. on pp. 59, 60).

[171] H.-H. Klauss, H. Luetkens, R. Klingeler, C. Hess, F. J. Litterst, M. Kraken, M. M. Korshunov, I. Eremin, S.-L. Drechsler, et al. "Commensurate Spin Density Wave in LaFeAsO: A Local Probe Study". In: *Phys. Rev. Lett.* 101 (7 2008), 077005. DOI: 10.1103/PhysRevLett.101.077005. URL: https://link.aps.org/doi/10.1103/PhysRevLett.101.077005 (cit. on p. 59).

[172] Q. Huang, Y. Qiu, Wei Bao, M. A. Green, J. W. Lynn, Y. C. Gasparovic, T. Wu, G. Wu, and X. H. Chen. "Neutron-Diffraction Measurements of Magnetic Order and a Structural Transition in the Parent $BaFe_2As_2$ Compound of FeAs-Based High-Temperature Superconductors". In: *Phys. Rev. Lett.* 101 (25 2008), 257003. DOI: 10.1103/PhysRevLett.101.257003. URL: https://link.aps.org/doi/10.1103/PhysRevLett.101.257003 (cit. on pp. 59, 61).

[173] M D Lumsden and A D Christianson. "Magnetism in Fe-based superconductors". In: *Journal of Physics: Condensed Matter* 22.20 (2010), 203203. DOI: 10.1088/0953-8984/22/20/203203. URL: https://doi.org/10.1088%2F0953-8984%2F22%2F20%2F203203 (cit. on p. 59).

[174] Y. Su, P. Link, A. Schneidewind, Th. Wolf, P. Adelmann, Y. Xiao, M. Meven, R. Mittal, M. Rotter, D. Johrendt, Th. Brueckel, and M. Loewenhaupt. "Antiferromagnetic ordering and structural phase transition in $Ba_2Fe_2As_2$ with Sn incorporated from the growth flux". In: *Phys. Rev. B* 79 (6 2009), 064504. DOI: 10.1103/PhysRevB.79.064504. URL: https://link.aps.org/doi/10.1103/PhysRevB.79.064504 (cit. on p. 59).

[175] Jun Zhao, W. Ratcliff, J. W. Lynn, G. F. Chen, J. L. Luo, N. L. Wang, Jiangping Hu, and Pengcheng Dai. "Spin and lattice structures of single-crystalline $SrFe_2As_2$". In: *Phys. Rev. B* 78 (14 2008), 140504. DOI: 10.1103/PhysRevB.78.140504. URL: https://link.aps.org/doi/10.1103/PhysRevB.78.140504 (cit. on p. 59).

[176] K. Matan, R. Morinaga, K. Iida, and T. J. Sato. "Anisotropic itinerant magnetism and spin fluctuations in $BaFe_2As_2$: A neutron scattering study". In: *Phys. Rev. B* 79 (5 2009), 054526. DOI: 10.1103/PhysRevB.79.054526. URL: https://link.aps.org/doi/10.1103/PhysRevB.79.054526 (cit. on p. 59).

[177] Erwin Wiesenmayer, Hubertus Luetkens, Gwendolyne Pascua, Rustem Khasanov, Alex Amato, Heidi Potts, Benjamin Banusch, Hans-Henning Klauss, and Dirk Johrendt. "Microscopic Coexistence of Superconductivity and Magnetism inBa1-xKxFe2As2". In: *Physical Review Letters* 107.23 (2011). DOI: 10.1103/physrevlett.107.237001. URL: http://dx.doi.org/10.1103/PhysRevLett.107.237001 (cit. on pp. 59, 61).

[178] C. Bernhard, C. N. Wang, L. Nuccio, L. Schulz, O. Zaharko, J. Larsen, C. Aristizabal, M. Willis, A. J. Drew, G. D. Varma, T. Wolf, and Ch. Niedermayer. "Muon spin rotation study of magnetism and superconductivity in $Ba(Fe_{1-x}Co_x)_2As_2$ single crystals". In: *Phys. Rev. B* 86 (18 2012), 184509. DOI: 10.1103/PhysRevB.86.184509. URL: https://link.aps.org/doi/10.1103/PhysRevB.86.184509 (cit. on pp. 59, 61).

[179] D. S. Inosov, G. Friemel, J. T. Park, A. C. Walters, Y. Texier, Y. Laplace, J. Bobroff, V. Hinkov, D. L. Sun, et al. "Possible realization of an antiferromagnetic Griffiths phase in $Ba(Fe_{1-x}Mn_x)_2As_2$". In: *Phys. Rev. B* 87 (22 2013), 224425. DOI: 10.1103/PhysRevB.87.224425. URL: https://link.aps.org/doi/10.1103/PhysRevB.87.224425 (cit. on pp. 59, 61).

[180] J Rodriguez-Carvajal, M T Fernandez-Diaz, and J L Martinez. "Neutron diffraction study on structural and magnetic properties of La2NiO4". In: *Journal of Physics: Condensed Matter* 3.19 (1991), 3215–3234. DOI: 10.1088/0953-8984/3/19/002. URL: https://doi.org/10.1088%2F0953-8984%2F3%2F19%2F002 (cit. on pp. 59, 61).

[181] B. Martínez, X. Obradors, E.J. Ansaldo, C. Niedermayer, D.R. Noakes, M.J. Sayagués, M. Vallet, and J. González-Calbet. "μ+SR study of magnetic order in La 2NiO4+δ". In: *Journal of Magnetism and Magnetic Materials* 104-107 (1992). Proceedings of the International Conference on Magnetism, Part II, 941 –943. DOI: https://doi.org/10.1016/0304-8853(92)90433-O. URL: http://www.sciencedirect.com/science/article/pii/030488539290433O (cit. on pp. 59, 62).

[182] K. H. Chow, P. A. Pattenden, S. J. Blundell, W. Hayes, F. L. Pratt, Th. Jestädt, M. A. Green, J. E. Millburn, M. J. Rosseinsky, et al. "Muon-spin-relaxation studies of magnetic order in heavily doped $La_{2-x}Sr_xNiO_{4+\delta}$". In: *Phys. Rev. B* 53 (22 1996), R14725–R14728. DOI: 10.1103/PhysRevB.53.R14725. URL: https://link.aps.org/doi/10.1103/PhysRevB.53.R14725 (cit. on p. 59).

[183] R.P. Santoro, D.J. Segal, and R.E. Newnham. "Magnetic properties of LiCoPO4 and LiNiPO4". In: *Journal of Physics and Chemistry of Solids* 27.6 (1966), 1192 –1193. DOI: https://doi.org/10.1016/0022-3697(66)90097-7. URL: http://www.sciencedirect.com/science/article/pii/0022369766900977 (cit. on pp. 59, 62).

[184] Thomas Bagger Stibius Jensen, Niels Bech Christensen, Michel Kenzelmann, Henrik Moodysson Rønnow, Christof Niedermayer, Niels Hessel Andersen, Kim Lefmann, Jürg Schefer, Martin v. Zimmermann, Jiying Li, Jerel L. Zarestky, and David Vaknin. "Field-induced magnetic phases and electric polarization in $LiNiPO_4$". In: *Phys. Rev. B* 79 (9 2009), 092412. DOI: 10.1103/PhysRevB.79.092412. URL: https://link.aps.org/doi/10.1103/PhysRevB.79.092412 (cit. on p. 59).

[185] P. J. Baker, I. Franke, F. L. Pratt, T. Lancaster, D. Prabhakaran, W. Hayes, and S. J. Blundell. "Probing magnetic order in $LiMPO_4$ (M = Ni, Co, Fe) and lithium diffusion in Li_xFePO_4". In: *Phys. Rev. B* 84 (17 2011), 174403. DOI: 10.1103/PhysRevB.84.174403. URL: https://link.aps.org/doi/10.1103/PhysRevB.84.174403 (cit. on pp. 59, 62).

[186] Oren Ofer, Jun Sugiyama, Jess H. Brewer, Martin Månsson, Krunoslav Prša, Eduardo J. Ansaldo, Genki Kobayashi, and Ryoji Kanno. "The Magnetic Phase of Lithium Transition Metal Phosphates LiMPO4 (M=Mn, Co, Ni)

Detected by μ+SR". In: *Physics Procedia* 30 (2012). 12th International Conference on Muon Spin Rotation, Relaxation and Resonance (μSR2011), 160–163. DOI: https://doi.org/10.1016/j.phpro.2012.04.063. URL: https://www.sciencedirect.com/science/article/pii/S1875389212012497 (cit. on pp. 59, 62).

[187] F. Moussa, M. Hennion, J. Rodriguez-Carvajal, H. Moudden, L. Pinsard, and A. Revcolevschi. "Spin waves in the antiferromagnet perovskite $LaMnO_3$: A neutron-scattering study". In: *Phys. Rev. B* 54 (21 1996), 15149–15155. DOI: 10.1103/PhysRevB.54.15149. URL: https://link.aps.org/doi/10.1103/PhysRevB.54.15149 (cit. on pp. 59, 63).

[188] R. H. Heffner, J. E. Sonier, D. E. MacLaughlin, G. J. Nieuwenhuys, G. M. Luke, Y. J. Uemura, William Ratcliff, S-W. Cheong, and G. Balakrishnan. "Muon spin relaxation study ofLa1-xCaxMnO3". In: *Physical Review B* 63.9 (2001). DOI: 10.1103/physrevb.63.094408. URL: http://dx.doi.org/10.1103/PhysRevB.63.094408 (cit. on p. 59).

[189] M. Cestelli Guidi, G. Allodi, R. De Renzi, G. Guidi, M. Hennion, L. Pinsard, and A. Amato. "Staggered magnetization, critical behavior, and weak ferromagnetic properties of $LaMnO_3$ by muon spin rotation". In: *Phys. Rev. B* 64 (6 2001), 064414. DOI: 10.1103/PhysRevB.64.064414. URL: https://link.aps.org/doi/10.1103/PhysRevB.64.064414 (cit. on pp. 59, 63).

[190] Sanghyun Lee, Seongil Choi, Jiyeon Kim, Hasung Sim, Choongjae Won, Seongsu Lee, Shin Ae Kim, Namjung Hur, and Je-Geun Park. "Antiferromagnetic ordering in Li2MnO3single crystals with a two-dimensional honeycomb lattice". In: *Journal of Physics: Condensed Matter* 24.45 (2012), 456004. DOI: 10.1088/0953-8984/24/45/456004. URL: https://doi.org/10.1088%2F0953-8984%2F24%2F45%2F456004 (cit. on pp. 59, 63).

[191] Jun Sugiyama, Kazuhiko Mukai, Hiroshi Nozaki, Masashi Harada, Martin Månsson, Kazuya Kamazawa, Daniel Andreica, Alex Amato, and Adrian D. Hillier. "Antiferromagnetic spin structure and lithium ion diffusion in Li_2MnO_3 probed by μ^+SR". In: *Phys. Rev. B* 87 (2 2013), 024409. DOI: 10.1103/PhysRevB.87.024409. URL: https://link.aps.org/doi/10.1103/PhysRevB.87.024409 (cit. on pp. 59, 64).

[192] W. Jauch, M. Reehuis, and A. J. Schultz. "γ-ray and neutron diffraction studies of CoF_2: magnetostriction, electron density and magnetic moments". In: *Acta Crystallographica Section A* 60.1 (2004), 51–57. DOI: 10.1107/S0108767303022803. URL: https://doi.org/10.1107/S0108767303022803 (cit. on pp. 59, 64).

[193] R De Renzi, G Guidi, P Podini, R A Tedeschi, and C Bucci. "Magnetic properties of MnF2 and CoF2 determined by implanted positive muons. II. Sublattice magnetization and phase transition". In: *Phys. Rev. B* 30 (1984), 197–204. DOI: 10.1103/PhysRevB.30.197. URL: http://cds.cern.ch/record/966709 (cit. on pp. 59, 64).

[194] R. De Renzi, R. Tedeschi, G. Guidi, C. Bucci, and S.F.J. Cox. "Investigation of the critical relaxation in MnF2 by Muon Spin Rotation". In: *Solid State Communications* 43.9 (1982), 683 –685. DOI: https://doi.org/10.1016/0038-1098(82)90771-2. URL: http://www.sciencedirect.com/science/article/pii/0038109882907712 (cit. on p. 59).

[195] I. V. Golosovsky, N. S. Sokolov, A. K. Kaveev, M. Boehm, J. Nogués, and S. Nannarone. "Magnetic order in an MnF2 epitaxial layer with the orthorhombic structure". In: *Journal of Experimental and Theoretical Physics Letters* 83.4 (2006), 152–155. DOI: 10.1134/S0021364006040059. URL: https://doi.org/10.1134/S0021364006040059 (cit. on p. 59).

[196] R. F. Kiefl, G. M. Luke, S. R. Kreitzman, M. Celio, R. Keitel, J. H. Brewer, D. R. Noakes, Y. J. Uemura, A. M. Portis, and V. Jaccarino. "Muon level-crossing resonance in antiferromagnetic MnF_2". In: *Phys. Rev. B* 35 (4 1987), 2079–2082. DOI: 10.1103/PhysRevB.35.2079. URL: https://link.aps.org/doi/10.1103/PhysRevB.35.2079 (cit. on pp. 59, 64).

[197] B. Roy, Abhishek Pandey, Q. Zhang, T. W. Heitmann, D. Vaknin, D. C. Johnston, and Y. Furukawa. "Experimental evidence of a collinear antiferromagnetic ordering in the frustrated $CoAl_2O_4$ spinel". In: *Phys. Rev. B* 88 (17 2013), 174415. DOI: 10.1103/PhysRevB.88.174415. URL: https://link.aps.org/doi/10.1103/PhysRevB.88.174415 (cit. on pp. 59, 65).

[198] M. Iakovleva, E. Vavilova, H.-J. Grafe, S. Zimmermann, A. Alfonsov, H. Luetkens, H.-H. Klauss, A. Maljuk, S. Wurmehl, B. Büchner, and V. Kataev. "Ground state and low-energy magnetic dynamics in the frustrated magnet $CoAl_2O_4$ as revealed by local spin probes". In: *Phys. Rev. B* 91 (14 2015), 144419. DOI: 10.1103/PhysRevB.91.144419. URL: https://link.aps.org/doi/10.1103/PhysRevB.91.144419 (cit. on pp. 59, 65).

[199] Andrew L. Goodwin, Matthew G. Tucker, Martin T. Dove, and David A. Keen. "Magnetic Structure of MnO at 10 K from Total Neutron Scattering Data". In: *Phys. Rev. Lett.* 96 (4 2006), 047209. DOI: 10.1103/PhysRevLett.96.047209. URL: https://link.aps.org/doi/10.1103/PhysRevLett.96.047209 (cit. on pp. 59, 65).

[200] Y. J. Uemura, T. Yamazaki, Y. Kitaoka, M. Takigawa, and H. Yasuoka. "Positive muon spin precession in magnetic oxides MnO and V2O3; local fields and phase transition". In: *Hyperfine Interactions* 17.1-4 (1984), 339–343. URL: http://inis.iaea.org/search/search.aspx?orig_q=RN:15047726 (cit. on pp. 59, 66).

[201] S. Nagamiya, K. Nagamine, O. Hashimoto, and T. Yamazaki. "Negative-Muon Spin Rotation at the Oxygen Site in Paramagnetic MnO". In: *Phys. Rev. Lett.* 35 (5 1975), 308–311. DOI: 10.1103/PhysRevLett.35.308. URL: https://link.aps.org/doi/10.1103/PhysRevLett.35.308 (cit. on pp. 59, 66).

[202] Eric Ressouche, Nolwenn Kernavanois, Louis-Pierre Regnault, and Jean-Yves Henry. "Magnetic structures of the metal monoxides NiO and CoO re-investigated by spherical neutron polarimetry". In: *Physica B: Condensed Matter* 385-386 (2006), 394 –397. DOI: https://doi.org/10.1016/j.physb.2006.05.082. URL: http://www.sciencedirect.com/science/article/pii/S0921452606009896 (cit. on pp. 59, 65).

[203] K. Nishiyama, S. Ohira, W. K. Dawson, and W. Higemoto. "Low temperature μSR studies in NiO and CoO". In: *Hyperfine Interactions* 104.1 (1997), 349–355. DOI: 10.1023/A:1012681305657. URL: https://doi.org/10.1023/A:1012681305657 (cit. on pp. 59, 66).

[204] W. Jauch, M. Reehuis, H. J. Bleif, F. Kubanek, and P. Pattison. "Crystallographic symmetry and magnetic structure of CoO". In: *Phys. Rev. B* 64 (5 2001), 052102. DOI: 10.1103/PhysRevB.64.052102. URL: https://link.aps.org/doi/10.1103/PhysRevB.64.052102 (cit. on pp. 59, 65).

[205] C. Tenailleau, E. Suard, J. Rodriguez-Carvajal, and P. Lacorre. "Influence of Mo-doping on the magnetic properties of V2O3". In: *Journal of Magnetism and Magnetic Materials* 278.1 (2004), 57 –67. DOI: https://doi.org/10.1016/j.jmmm.2003.11.373. URL: http://www.sciencedirect.com/science/article/pii/S0304885303019577 (cit. on pp. 59, 66).

[206] A. H. Hill, F. Jiao, P. G. Bruce, A. Harrison, W. Kockelmann, and C. Ritter. "Neutron Diffraction Study of Mesoporous and Bulk Hematite, α-Fe2O3". In: *Chemistry of Materials* 20.15 (2008), 4891–4899. DOI: 10.1021/cm800009s. eprint: https://doi.org/10.1021/cm800009s. URL: https://doi.org/10.1021/cm800009s (cit. on pp. 59, 67).

[207] K. Rüegg, C. Boekema, A. Denison, W. Hofmann, and W. Kündig. "Muon spin rotation experiments in α-Fe2O3 and Cr2O3". In: *Journal of Magnetism and Magnetic Materials* 15-18 (1980), 669 –670. DOI: https://doi.org/10.1016/0304-8853(80)90713-1. URL: http://www.sciencedirect.com/science/article/pii/0304885380907131 (cit. on pp. 59, 67).

[208] C. Boekema, A.B. Denison, and K.J. Rüegg. "Muon spin rotation in antiferromagnetic oxides". In: *Journal of Magnetism and Magnetic Materials* 36.1 (1983), 111 –114. DOI: https://doi.org/10.1016/0304-8853(83)91052-1. URL: http://www.sciencedirect.com/science/article/pii/0304885383910521 (cit. on pp. 59, 67).

[209] M. H. Dehn, J. K. Shenton, D. J. Arseneau, W. A. MacFarlane, G. D. Morris, A. Maigné, N. A. Spaldin, and R. F. Kiefl. "Local Electronic Structure and Dynamics of Muon-Polaron Complexes in Fe_2O_3". In: *Phys. Rev. Lett.* 126 (3 2021), 037202. DOI: 10.1103/PhysRevLett.126.037202. URL: https://link.aps.org/doi/10.1103/PhysRevLett.126.037202 (cit. on pp. 59, 67, 79).

[210] C.F. [van Bruggen], M.B. Vellinga, and C. Haas. “Semiconducting and magnetic properties of rhombohedral Cr2S3”. In: *Journal of Solid State Chemistry* 2.2 (1970), 303 –308. DOI: https://doi.org/10.1016/0022-4596(70)90086-1. URL: http://www.sciencedirect.com/science/article/pii/0022459670900861 (cit. on p. 59).

[211] T.J.A. Popma, C. Haas, and B. [Van Laar]. “Spin structure and magnetic anisotropy of Cr5S6 and rhombohedral Cr2S3”. In: *Journal of Physics and Chemistry of Solids* 32.3 (1971), 581 –590. DOI: https://doi.org/10.1016/0022-3697(71)90007-2. URL: http://www.sciencedirect.com/science/article/pii/0022369771900072 (cit. on pp. 59, 72).

[212] M. L. Brooks, S. J. Blundell, C. A. Steer, T. Lancaster, F. L. Pratt, P. Vaqueiro, and A. V. Powell. “Muon spin rotation study of magnetism in electron-doped chromium sulfide”. In: *Phys. Rev. B* 72 (1 2005), 012419. DOI: 10.1103/PhysRevB.72.012419. URL: https://link.aps.org/doi/10.1103/PhysRevB.72.012419 (cit. on pp. 59, 68, 72, 76, 78).

[213] A. A. Aczel, E. Baggio-Saitovitch, S. L. Budko, P. C. Canfield, J. P. Carlo, G. F. Chen, Pengcheng Dai, T. Goko, W. Z. Hu, et al. “Muon-spin-relaxation studies of magnetic order and superfluid density in antiferromagnetic NdFeAsO, $BaFe_2As_2$, and superconducting $Ba_{1-x}K_xFe_2As_2$”. In: *Phys. Rev. B* 78 (21 2008), 214503. DOI: 10.1103/PhysRevB.78.214503. URL: https://link.aps.org/doi/10.1103/PhysRevB.78.214503 (cit. on p. 61).

[214] Rasmus Toft-Petersen, Manfred Reehuis, Thomas B. S. Jensen, Niels H. Andersen, Jiying Li, Manh Duc Le, Mark Laver, Christof Niedermayer, Bastian Klemke, Kim Lefmann, and David Vaknin. “Anomalous magnetic structure and spin dynamics in magnetoelectric $LiFePO_4$”. In: *Phys. Rev. B* 92 (2 2015), 024404. DOI: 10.1103/PhysRevB.92.024404. URL: https://link.aps.org/doi/10.1103/PhysRevB.92.024404 (cit. on p. 62).

[215] J.-P. Rivera. “The linear magnetoelectric effect in LiCoPO4Revisited”. In: *Ferroelectrics* 161.1 (1994), 147–164. DOI: 10.1080/00150199408213364. eprint: https://doi.org/10.1080/00150199408213364. URL: https://doi.org/10.1080/00150199408213364 (cit. on p. 62).

[216] E.F. Bertaut and M. Mercier. “Magnetoelectricity in theory and experiment”. In: *Materials Research Bulletin* 6.10 (1971), 907–921. DOI: https://doi.org/10.1016/0025-5408(71)90069-9. URL: https://www.sciencedirect.com/science/article/pii/0025540871900699 (cit. on p. 62).

[217] A. B. Denison, C. Boekema, R. L. Lichti, K. C. Chan, D. W. Cooke, R. H. Heffner, R. L. Hutson, M. Leon, and M. E. Schillaci. “Muon spin rotation study of V2O3”. In: *Journal of Applied Physics* 57.8 (1985), 3743–3745. DOI: 10.1063/1.334955. eprint: https://doi.org/10.1063/1.334955. URL: https://doi.org/10.1063/1.334955 (cit. on pp. 63, 66).

[218] Z. Yamani, Z. Tun, and D. H. Ryan. "Neutron scattering study of the classical antiferromagnet MnF2: a perfect hands-on neutron scattering teaching courseSpecial issue on Neutron Scattering in Canada." In: *Canadian Journal of Physics* 88.10 (2010), 771–797. DOI: 10.1139/P10-081. eprint: https://doi.org/10.1139/P10-081. URL: https://doi.org/10.1139/P10-081 (cit. on p. 64).

[219] A.H. Morrish, G.B. Johnston, and N.A. Curry. "Magnetic transition in pure and Ga doped α-Fe2O3". In: *Physics Letters* 7.3 (1963), 177–178. DOI: https://doi.org/10.1016/0031-9163(63)90372-X. URL: https://www.sciencedirect.com/science/article/pii/003191636390372X (cit. on p. 67).

[220] R. Nathans, S. J. Pickart, H. A. Alperin, and P. J. Brown. "Polarized-Neutron Study of Hematite". In: *Phys. Rev.* 136 (6A 1964), A1641–A1647. DOI: 10.1103/PhysRev.136.A1641. URL: https://link.aps.org/doi/10.1103/PhysRev.136.A1641 (cit. on p. 67).

[221] Michał Stekiel, Radosław Przeniosło, Izabela Sosnowska, Andrew Fitch, Jacek B. Jasiński, Joey A. Lussier, and Mario Bieringer. "Lack of a threefold rotation axis in α-Fe_2O_3 and α-Cr_2O_3 crystals". In: *Acta Crystallographica Section B* 71.2 (2015), 203–208. DOI: 10.1107/S205252061500342X. URL: https://doi.org/10.1107/S205252061500342X (cit. on p. 67).

[222] E.F. Bertaut, J. Cohen, B. Lambert-Andron, and P. Mollard. "Étude de Cr2S3 rhomboédrique par diffraction neutronique et mesures magnétiques". In: *Journal de Physique* 29.8-9 (1968), 813–824. DOI: 10.1051/jphys:01968002908-9081300. URL: https://hal.archives-ouvertes.fr/jpa-00206719 (cit. on pp. 68, 72).

[223] Jun Sugiyama, Hiroshi Nozaki, Masashi Harada, Kazuya Kamazawa, Oren Ofer, Martin Månsson, Jess H. Brewer, Eduardo J. Ansaldo, Kim H. Chow, et al. "Magnetic and diffusive nature of $LiFePO_4$ investigated by muon spin rotation and relaxation". In: *Phys. Rev. B* 84 (5 2011), 054430. DOI: 10.1103/PhysRevB.84.054430. URL: https://link.aps.org/doi/10.1103/PhysRevB.84.054430 (cit. on p. 68).

[224] Matteo Cococcioni and Stefano de Gironcoli. "Linear response approach to the calculation of the effective interaction parameters in the LDA + U method". In: *Phys. Rev. B* 71 (3 2005), 035105. DOI: 10.1103/PhysRevB.71.035105. URL: https://link.aps.org/doi/10.1103/PhysRevB.71.035105 (cit. on pp. 69, 73).

[225] G. Rollmann, A. Rohrbach, P. Entel, and J. Hafner. "First-principles calculation of the structure and magnetic phases of hematite". In: *Phys. Rev. B* 69 (16 2004), 165107. DOI: 10.1103/PhysRevB.69.165107. URL: https://link.aps.org/doi/10.1103/PhysRevB.69.165107 (cit. on p. 69).

[226] A. Floris, S. de Gironcoli, E. K. U. Gross, and M. Cococcioni. "Vibrational properties of MnO and NiO from DFT + U-based density functional perturbation theory". In: *Phys. Rev. B* 84 (16 2011), 161102. DOI: 10.1103/PhysRevB.84.161102. URL: https://link.aps.org/doi/10.1103/PhysRevB.84.161102 (cit. on p. 69).

[227] Myron B. Salamon and Marcelo Jaime. "The physics of manganites: Structure and transport". In: *Rev. Mod. Phys.* 73 (3 2001), 583–628. DOI: 10.1103/RevModPhys.73.583. URL: https://link.aps.org/doi/10.1103/RevModPhys.73.583 (cit. on p. 72).

[228] Maria Baldini, Takaki Muramatsu, Mohammad Sherafati, Ho-kwang Mao, Lorenzo Malavasi, Paolo Postorino, Sashi Satpathy, and Viktor V. Struzhkin. "Origin of colossal magnetoresistance in LaMnO3 manganite". In: *Proceedings of the National Academy of Sciences* 112.35 (2015), 10869–10872. DOI: 10.1073/pnas.1424866112. eprint: https://www.pnas.org/content/112/35/10869.full.pdf. URL: https://www.pnas.org/content/112/35/10869 (cit. on p. 72).

[229] B. [Van Laar]. "The magnetic structure of trigonal Cr2S3". In: *Physics Letters A* 25.1 (1967), 27 –29. DOI: https://doi.org/10.1016/0375-9601(67)90320-9. URL: http://www.sciencedirect.com/science/article/pii/0375960167903209 (cit. on pp. 72, 75, 78).

[230] Koichiro Yaji, Akio Kimura, Chiyuki Hirai, Masaki Taniguchi, Michie Koyama, Hitoshi Sato, Kenya Shimada, Arata Tanaka, Takayuki Muro, Shin Imada, and et al. "Electronic structure ofCr1-δX(X=S,Te)studied by Cr2psoft x-ray magnetic circular dichroism". In: *Physical Review B* 70.6 (2004). DOI: 10.1103/physrevb.70.064402. URL: http://dx.doi.org/10.1103/PhysRevB.70.064402 (cit. on pp. 72, 75).

[231] Yamini Sharma and Pankaj Srivastava. "Electronic Structure And Magnetic Properties Of Rhombohedral Cr2S3". In: *AIP Conference Proceedings* 1347.1 (2011), 123–127. DOI: 10.1063/1.3601801. eprint: https://aip.scitation.org/doi/pdf/10.1063/1.3601801. URL: https://aip.scitation.org/doi/abs/10.1063/1.3601801 (cit. on pp. 73, 75).

[232] Liu Xie, Jun Wang, Jie Li, Chang Li, Yan Zhang, Benpeng Zhu, Yuzheng Guo, Zhongchang Wang, and Kai Zhang. "An Atomically Thin Air-Stable Narrow-Gap Semiconductor Cr2S3 for Broadband Photodetection with High Responsivity". In: *Advanced Electronic Materials* 7.7 (2021), 2000962. DOI: https://doi.org/10.1002/aelm.202000962. eprint: https://onlinelibrary.wiley.com/doi/pdf/10.1002/aelm.202000962. URL: https://onlinelibrary.wiley.com/doi/abs/10.1002/aelm.202000962 (cit. on p. 73).

[233] Chunyu Li, Feng Ke, Qingyang Hu, Zhenhai Yu, Jinggeng Zhao, Zhiqiang Chen, and Hao Yan. "Correlated structural and electronic phase transformations in transition metal chalcogenide under high pressure". In: *Journal of Applied Physics* 119.13 (2016), 135901. DOI: 10.1063/1.4945323.

eprint: https://doi.org/10.1063/1.4945323. URL: https://doi.org/10.1063/1.4945323 (cit. on p. 73).

[234] Vladimir I Anisimov, F Aryasetiawan, and A I Lichtenstein. "First-principles calculations of the electronic structure and spectra of strongly correlated systems: the LDA+U method". In: *Journal of Physics: Condensed Matter* 9.4 (1997), 767–808. DOI: 10.1088/0953-8984/9/4/002. URL: https://doi.org/10.1088/0953-8984/9/4/002 (cit. on p. 73).

[235] Heather J. Kulik, Matteo Cococcioni, Damian A. Scherlis, and Nicola Marzari. "Density Functional Theory in Transition-Metal Chemistry: A Self-Consistent Hubbard U Approach". In: *Phys. Rev. Lett.* 97 (10 2006), 103001. DOI: 10.1103/PhysRevLett.97.103001. URL: https://link.aps.org/doi/10.1103/PhysRevLett.97.103001 (cit. on p. 73).

[236] Jianwei Sun, Adrienn Ruzsinszky, and John P. Perdew. "Strongly Constrained and Appropriately Normed Semilocal Density Functional". In: *Phys. Rev. Lett.* 115 (3 2015), 036402. DOI: 10.1103/PhysRevLett.115.036402. URL: https://link.aps.org/doi/10.1103/PhysRevLett.115.036402 (cit. on p. 73).

[237] N. Troullier and José Luís Martins. "Efficient pseudopotentials for plane-wave calculations". In: *Phys. Rev. B* 43 (3 1991), 1993–2006. DOI: 10.1103/PhysRevB.43.1993. URL: https://link.aps.org/doi/10.1103/PhysRevB.43.1993 (cit. on p. 73).

[238] F. Jellinek. "The structures of the chromium sulphides". In: *Acta Crystallographica* 10.10 (1957), 620–628. DOI: 10.1107/S0365110X57002200. URL: https://doi.org/10.1107/S0365110X57002200 (cit. on p. 73).

[239] P. Vaqueiro, A. V. Powell, A. I. Coldea, C. A. Steer, I. M. Marshall, S. J. Blundell, J. Singleton, and T. Ohtani. "Colossal magnetoresistance in the layered chromium sulfide Cr_2S_{3-x} $(x = 0.08)$". In: *Phys. Rev. B* 64 (13 2001), 132402. DOI: 10.1103/PhysRevB.64.132402. URL: https://link.aps.org/doi/10.1103/PhysRevB.64.132402 (cit. on pp. 75, 78).

[240] Wills, A. "Magnetic structures and their determination using group theory". In: *J. Phys. IV France* 11 (2001), Pr9–133–Pr9–158. DOI: 10.1051/jp4:2001906. URL: https://doi.org/10.1051/jp4:2001906 (cit. on p. 75).

[241] M. H. Dehn, J. K. Shenton, S. Holenstein, Q. N. Meier, D. J. Arseneau, D. L. Cortie, B. Hitti, A. C. Y. Fang, W. A. MacFarlane, et al. "Observation of a Charge-Neutral Muon-Polaron Complex in Antiferromagnetic Cr_2O_3". In: *Phys. Rev. X* 10 (1 2020), 011036. DOI: 10.1103/PhysRevX.10.011036. URL: https://link.aps.org/doi/10.1103/PhysRevX.10.011036 (cit. on p. 79).